

**Effects of lattice defects on
thermoelectric properties of
calcium-manganite compounds for
energy harvesting applications**

Ayelet Graff

**Effects of lattice defects on thermoelectric
properties of calcium-manganite
compounds for energy harvesting
applications**

Research Thesis

**In Partial Fulfillment of the Requirements for the
Degree of Master of Science in Materials Science and
Engineering**

Ayelet Graff

**Submitted to the Senate of the
Technion - Israel Institute of Technology**

Shebat 5775, Haifa, February 2015

Acknowledgments

This research thesis was done under the supervision of Asst. Prof. Yaron Amouyal at the Department of Materials Science and Engineering, Technion – Israel Institute of Technology.

The generous financial help of Irwin and Joan Jacobs Graduate School at the Technion, as well as the NEVET program of the Grand Technion Energy Program (GTEP) are gratefully acknowledged.

Publications

Graff, A., Amouyal, Y.: “Reduced thermal conductivity in niobium-doped calcium-manganate compounds for thermoelectric applications”, *Appl. Phys. Lett.* Vol. 105 (18) p.181906, (2014).

Table of Content

Table of Content

List of figures

List of tables

List of symbols and acronyms

1. Abstract.....	15
2. Literature review	19
2.1 <i>Basics of thermoelectricity.....</i>	19
2.2 <i>State-of-the-art TE materials and the interest in thermoelectric oxides.....</i>	23
2.3 <i>Thermal conductivity in crystalline solids</i>	26
2.3.1 Fundamentals of thermal conductivity.....	26
2.3.2 The Callaway model for thermal conductivity	28
2.3.3 The microstructure-thermal conductivity relationship.....	29
2.4 <i>The interest in Ruddlesden Popper phases</i>	30
2.5 <i>Summary</i>	33
2.6 <i>Research goals.....</i>	33
3. Experimental and analytical methods.....	35
3.1 <i>Sample preparation.....</i>	35
3.2 <i>Microstructure analysis</i>	36
3.2.1 X-ray diffraction (XRD)	36
3.2.2 High-resolution scanning electron microscopy (HR-SEM).....	36
3.2.3 Grain size analysis	36
3.2.4 Density measurements	37
3.3 <i>Thermoelectric characterization.....</i>	37
3.3.1 Electrical conductivity and thermopower measurements	37
3.3.1.1 Electrical conductivity measurement for bar-shaped specimens	37
3.3.1.2 Thermopower measurements for bar-shaped specimens	38
3.3.1.3 Electrical conductivity measurement for planar specimens.....	39
3.3.1.4 Thermopower measurements for the planar geometry	41
3.3.2 Thermal conductivity measurements	42
3.4 <i>First-principles calculations.....</i>	44

4. Results	46
<i>4.1 Microstructure characterization.....</i>	<i>46</i>
4.1.1 X-ray diffraction (XRD) analysis	46
4.1.2 High-resolution scanning electron microscopy (HR-SEM) analysis.....	55
4.1.3 Grain size analysis	57
<i>4.2 Electrical measurements.....</i>	<i>59</i>
4.2.1 Electrical conductivity measurements	59
4.2.2 Seebeck coefficient measurements	63
<i>4.3 Thermal diffusivity measurments</i>	<i>68</i>
<i>4.4 Thermal conductivity measurements.....</i>	<i>72</i>
5. Discussion.....	78
<i>5.1 Thermal conductivity analysis</i>	<i>78</i>
5.1.1 The effects of CaO planes.....	78
5.1.2. The effects of porosity	84
5.1.3. The effects of doping	86
<i>5.2 Analysis of electrical conductivity data</i>	<i>86</i>
<i>5.3 Power Factor calculation</i>	<i>88</i>
<i>5.4 The figure of merit, ZT.....</i>	<i>92</i>
6. Summary, conclusions, and recommendations for further research	96
7. References.....	99

List of figures

Figure 1: A schematic illustration of a thermoelectric module for power generation (Seebeck effect). ⁶	20
Figure 2: A schematic illustration of a thermoelectric module showing the thermoelements connected electrically in series and thermally in parallel. ¹	20
Figure 3: Thermoelectric power generation efficiency versus T_{hot} (for $T_{\text{cold}} = 300$ K). Efficiency for conventional mechanical engines as the Carnot limit are also shown. ⁸	22
Figure 4: Charge carrier concentration dependence of transport parameters required for optimum thermoelectric performance. ⁹	23
Figure 5: The temperature-dependent ZT- values of (a) n-type and (b) p-type compounds. Approximate compositions are presented. ¹	24
Figure 6: (a) Schematic comparison between different thermoelectric materials for waste heat harvesting, in terms of the temperature range of operation, abundance, and environmental friendliness of their constituent elements. (b) The abundance of elements present in TE materials. Elements represented by dark-colored columns exhibit abundance of <1 ppm. ¹²	25
Figure 7: The timeline of the development of the highest ZT-values of oxide thermoelectric materials. ⁹	26
Figure 8: A schematic illustration of the crystal structure of $\text{CaO}(\text{CaMnO}_3)_m$ Ruddlesden-Popper compound for (a) $m=1$, (b) $m=2$, (c) $m=3$, showing the layering between the CaMnO_3 perovskite and CaO rock-salt structures. The periodicities of $m=1$ through 3 are denoted by a tetragonal-crystal structure having the $I4/mmm$ symmetry space group (JCPDS numbers: 040067894, 040165273, and 000180298 for $m=1$, 2, and 3, respectively).....	32

Figure 9: A schematic description of the 4pp technique for electrical conductivity measurement.....	38
Figure 10: A schematic description of the Seebeck coefficient measurement setup applied at the Physics Department, Technion.	39
Figure 11: A schematic description of the SBA-458 Seebeck coefficient measurement setup.....	41
Figure 12: A typical configuration for the measurement of the Seebeck coefficient.	42
Figure 13: A schematic description of the laser flash analysis (LFA) method.	44
Figure 14: An X-ray diffraction (XRD) pattern acquired from the undoped compound of the $m=1$ periodicity, fitting the tetragonal-crystal structure having the $I4/mmm$ -symmetry (JCPDS number 040067894).....	47
Figure 15: An X-ray diffraction (XRD) pattern acquired from the La-doped compound of the $m=1$ periodicity, fitting the tetragonal-crystal structure having the $I4/mmm$ -symmetry (JCPDS number 040067894).....	47
Figure 16: An X-ray diffraction (XRD) pattern acquired from the Nb-doped compound of the $m=1$ periodicity, fitting the tetragonal-crystal structure having the $I4/mmm$ -symmetry (JCPDS number 040067894).....	48
Figure 17: An X-ray diffraction (XRD) pattern acquired from the undoped compound of the $m=2$ periodicity, fitting the tetragonal-crystal structure having the $I4/mmm$ -symmetry (JCPDS number: 040165273).	48
Figure 18: An X-ray diffraction (XRD) pattern acquired from the La-doped compound of the $m=2$ periodicity, fitting the tetragonal-crystal structure having the $I4/mmm$ -symmetry (JCPDS number: 040165273).	49

Figure 19: An X-ray diffraction (XRD) pattern acquired from the Nb-doped compound of the $m=2$ periodicity, fitting the tetragonal-crystal structure having the $I4/mmm$ -symmetry (JCPDS number: 040165273).	49
Figure 20: An X-ray diffraction (XRD) pattern acquired from the undoped compound of the $m=3$ periodicity, fitting the tetragonal-crystal structure having the $I4/mmm$ -symmetry (JCPDS number: 000180298)	50
Figure 21: An X-ray diffraction (XRD) pattern acquired from the Nb-doped compound of the $m=3$ periodicity, fitting the tetragonal-crystal structure having the $I4/mmm$ -symmetry (JCPDS number: 000180298)	50
Figure 22: An X-ray diffraction (XRD) pattern acquired from the undoped compound of the $m=\infty$ periodicity, fitting the orthorhombic-crystal structure having the $Pnma$ - symmetry (JCPDS number 040078030).	51
Figure 23: An X-ray diffraction (XRD) pattern acquired from the La-doped compound of the $m=\infty$ periodicity, fitting the orthorhombic-crystal structure having the $Pnma$ -symmetry (JCPDS number 040078030).	51
Figure 24: An X-ray diffraction (XRD) pattern acquired from the Nb-doped compound of the $m=\infty$ periodicity, fitting the orthorhombic-crystal structure having the $Pnma$ -symmetry (JCPDS number 040078030).	52
Figure 25: An X-ray diffraction (XRD) pattern acquired from the La-doped compound of the $m=3^*$ periodicity, fitting to the combination of $m=\infty$ (blue dots) and $m=2$ (red diamonds).	53
Figure 26: An X-ray diffraction (XRD) pattern acquired from the Nb-doped compound of the $m=4^*$ periodicity, fitting to the combination of $m=\infty$ periodicity (blue dots) and $m=3$ periodicity (red diamonds).	54
Figure 27: An X-ray diffraction (XRD) pattern acquired from the Nb-doped compound of the $m=5^*$ periodicity, fitting to the combination of $m=\infty$ periodicity (blue dots) and $m=3$ periodicity (red diamonds).	54

Figure 28: HRSEM micrographs of the different undoped and doped specimens having the $m=1,2,3$, and inf. periodicities.....	56
Figure 29: HRSEM micrographs taken from the Nb-doped specimens with $m=4^*$ and 5^* periodicities.....	57
Figure 30: Average grain widths measured for all compounds of the different periodicities (m-values).....	58
Figure 31: Grain Size distribution for the $m=\text{inf}$ undoped sample.....	59
Figure 32: Graphical representation of the electrical conductivities plotted for the extended temperature range of 80 through 1000 K for the $m=1$ compounds: undoped (squares), La-doped (triangles), and Nb-doped (circles).....	60
Figure 33: Graphical representation of the electrical conductivities plotted for the extended temperature range of 80 through 1000 K for the $m=2$ compounds: undoped (squares), La-doped (triangles), and Nb-doped (circles).....	60
Figure 34: Graphical representation of the electrical conductivities plotted for the extended temperature range of 80 through 1000 K for the $m=3$ compounds: undoped (squares), La-doped (triangles), and Nb-doped (circles).....	61
Figure 35: Graphical representation of the electrical conductivities plotted for the extended temperature range of 80 through 1000 K for the $m=\text{inf}$ compounds: undoped (squares), La-doped (triangles), and Nb-doped (circles).....	61
Figure 36: Electrical conductivity Vs. temperature for the La-doped samples having the periodicities of $m=\text{inf}$ (red markers), $m=1$ (black), $m=2$ (green), and $m=3^*$ (blue).....	62
Figure 37: Electrical conductivity Vs. temperature for the Nb-doped samples having the periodicities of $m=\text{inf}$ (red markers), $m=1$ (black), $m=2$ (green), and $m=3$ (blue).	63

Figure 38: The temperature-dependent Seebeck coefficients measured for the compounds with the $m=1$ periodicity, plotted for the undoped (squares), La-doped (triangles), and Nb-doped (circles) states.	64
Figure 39: The temperature-dependent Seebeck coefficients measured for the compounds with $m=2$ periodicity plotted for the undoped (squares), La-doped (triangles), and Nb-doped (circles) states.	65
Figure 40: The temperature-dependent Seebeck coefficients measured for the compounds with $m=3$ periodicity plotted for the undoped (squares), La-doped (triangles), and Nb-doped (circles) states.	65
Figure 41: The temperature-dependent Seebeck coefficients measured for the compounds with $m=\infty$ periodicity plotted for the undoped (squares), La-doped (triangles), and Nb-doped (circles) states.	66
Figure 42: The temperature-dependent Seebeck coefficients measured for the La-doped compounds of different periodicities: $m=\infty$ (red), $m=3^*$ (green), $m=2$ (blue) and $m=1$ (black).	67
Figure 43: The temperature-dependent Seebeck coefficients measured for the Nb-doped compounds of different periodicities: $m=\infty$ (red), $m=5^*$ (purple), $m=4^*$ (aqua), $m=3$ (green), $m=2$ (blue) and $m=1$ (black).	67
Figure 44: The temperature-dependent thermal diffusivities of the compounds having $m=1$ periodicity measured for the undoped (squares), La-doped (triangles), and Nb-doped (circles) ones.	68
Figure 45: The temperature-dependent thermal diffusivities of the compounds having $m=2$ periodicity measured for the undoped (squares), La-doped (triangles), and Nb-doped (circles) ones.	69
Figure 46: The temperature-dependent thermal diffusivities of the compounds having $m=3$ periodicity measured for the undoped (squares), La-doped (triangles), and Nb-doped (circles) ones.	69

Figure 47: The temperature-dependent thermal diffusivities of the compounds having $m=i$ periodicity measured for the undoped (squares), La-doped (triangles), and Nb-doped (circles) ones.....	70
Figure 48: The temperature-dependent thermal diffusivity measured for the La-doped compounds of different periodicities: $m=\text{inf}$ (magenta), $m=1$ (black), $m=2$ (red), and $m=3^*$ (blue).....	71
Figure 49: The temperature-dependent thermal conductivity measured for the Nb-doped compounds of different periodicities: $m=\text{inf}$ (magenta), $m=1$ (black), $m=2$ (red), $m=3$ (blue), $m=4^*$ (dark green), and $m=5^*$ (light green).	71
Figure 50: Specific heat vs. temperature as measured for several specimens employing laser flash analyzer (LFA).	73
Figure 51: An interpolated function for the heat capacity, representative for all specimens.....	73
Figure 52: The temperature-dependent thermal conductivities of the compounds having $m=1$ periodicity measured for the undoped (squares), La-doped (triangles), and Nb-doped (circles) ones.....	74
Figure 53: The temperature-dependent thermal conductivities of the compounds having $m=2$ periodicity measured for the undoped (squares), La-doped (triangles), and Nb-doped (circles) ones.....	75
Figure 54: The temperature-dependent thermal conductivities of the compounds having $m=3$ periodicity measured for the undoped (squares), La-doped (triangles), and Nb-doped (circles) ones.....	75
Figure 55: The temperature-dependent thermal conductivities of the compounds having $m=\text{inf}$ periodicity measured for the undoped (squares), La-doped (triangles), and Nb-doped (circles) ones.	76

Figure 56: The temperature-dependent thermal conductivity measured for the La-doped compounds of different periodicities: $m=\text{inf}$ (magenta), $m=1$ (black), $m=2$ (red), and $m=3^*$ (blue).....	77
Figure 57: The temperature-dependent thermal conductivity measured for the Nb-doped compounds of different periodicities: $m=\text{inf}$ (magenta), $m=1$ (black), $m=2$ (red), $m=3$ (blue), $m=4^*$ (dark green), and $m=5^*$ (light green).	77
Figure 58: The temperature-dependent thermal conductivities of the undoped $m=1,2,3$, and inf structures. The values were calculated based on the Callaway model and on the sound velocities and Debye temperatures that were obtained from first-principles.	81
Figure 59: The temperature-dependent thermal conductivities of the undoped $m=1, 2, 3, 4, 5$, and inf structures. The values were calculated based on the Callaway model and on the average sound velocities and Debye temperatures that were obtained from first-principles	82
Figure 60: The temperature-dependent thermal conductivities of the undoped $m=1, 2, 3, 4$, and 5 structures. The values were calculated based on the Callaway model and on the average sound velocities and Debye temperatures that were obtained from first-principles	83
Figure 61: Relative thermal conductivity calculated using a Callaway-based model for homogeneously-dispersed precipitates of different number densities, plotted for 100 (squares), 200 (circles), and 300 K (diamonds). ²⁶	85
Figure 62: The room-temperature values of electrical conductivity as measured for the different m -periodicities for the La-doped samples.	87
Figure 63: The room-temperature values of electrical conductivity as measured for the different m -periodicities for the Nb-doped samples.....	87
Figure 64: The temperature-dependent power factor (PF) values calculated for all La-doped samples, based on the measured thermopower and electrical conductivity.....	89

Figure 65: The temperature-dependent power factor (PF) values calculated for all Nb-doped samples, based on the measured thermopower and electrical conductivity.....	89
Figure 66: The ratio between the PF for a given m-value and that of m=inf. at room temperature, plotted for the La-doped materials with m=1, 2, and 3*	90
Figure 67: The ratio between the PF for a given m-value and that of m=inf. at room temperature, plotted for the Nb-doped materials with m=1, 2, 3, 4*, and 5*	91
Figure 68: The temperature-dependent ZT-values calculated for all La-doped samples, based on the measured thermopower, electrical conductivities, and thermal conductivities	93
Figure 69: The temperature-dependent ZT-values calculated for all Nb-doped samples, based on the measured thermopower, electrical conductivities, and thermal conductivities	93
Figure 70: The temperature-dependent ZT-values calculated for the m=inf.-type La- (blue) and Nb-doped (red) samples, based on the measured thermopower, electrical conductivities, and thermal conductivities.....	94

List of tables

Table 1: Room temperature crystallographic data for the $\text{CaO}(\text{CaMnO}_3)_m$ -compounds with $m=1, 2, 3$, and ∞ (inf.).....	32
Table 2: the nominal stoichiometries of the undoped, La-doped, and Nb-doped compounds that were synthesized, denoted by $m=\infty$ (inf.), and 1 through 5.	36
Table 3: Average grain widths measured for the compounds investigated in this study...	58
Table 4: the bulk densities calculated for all samples produced.....	72
Table 5: The sound velocities and Debye temperatures calculated for the undoped $m=1, 2, 3$, and inf. from first-principles.	80

List of symbols and acronyms

TE – thermoelectric

ZT – figure of merit

S - Seebeck coefficient

σ - The material's electrical conductivities

κ - The material's thermal conductivities.

κ_{ph} – Phonon contribution to thermal conductivity.

κ_{el} - Conduction electrons contribution to thermal conductivity.

η - The total efficiency of a TE module.

RP - Ruddlesden-Popper

PGEC - phonon glass electron crystal

U - umklapp processes

GB – grain boundaries

PF – power factor

T_D – Debye temperature

ν_D - Debye frequency

ν_s -Sound velocity

XRD - x-ray diffraction

SEM - scanning electron microscopy

HRSEM - high-resolution scanning electron microscope

LFA - laser flash analysis

SBA – Seebeck Analyzer

k_B - The Boltzmann constant: $k_B = 1.38 \times 10^{-23} \text{ J} \cdot \text{K}^{-1}$

\hbar - The reduced Planck's constant: $\hbar = h/2\pi = 1.054 \times 10^{-34} \text{ J} \cdot \text{s}$

ω - The phonon angular frequency.

γ - The Grüneisen parameter.

τ - Phonon relaxation time

μ - The charge carrier mobility

n - The charge carrier concentration.

ρ - The electrical resistivity

e - The electron charge

C_V - The constant-volume specific heat (heat capacity)

R - Average resistance.

α - The thermal diffusivity.

C_p - The specific heat.

1. Abstract

One of the directions in the search for alternative energy sources is capturing waste heat and converting it into electricity using thermoelectric (TE) generators. Such generators are based on the Seebeck effect, which was discovered in 1821 by T. J. Seebeck (1770-1831). In the Seebeck effect, a temperature gradient across a material initiates a diffusion of charge carriers across that gradient, thus creating an open-circuit voltage between the hot and cold poles of the material. A TE device consists of several TE couples of n-type and p-type legs, which are connected electrically in series and thermally in parallel.

An efficient TE material is characterized by a high TE *figure of merit*, ZT , which is manifested by a large Seebeck coefficient (*thermopower*, i.e. the ratio of voltage to temperature difference), high electrical conductivity, and low thermal conductivity. These three physical magnitudes embodied in ZT depend on the carrier concentration. Thus, improving ZT by minimizing the thermal conductivity without significantly affecting the electrical conductivity is a main challenge in the TE field. Furthermore, these properties are highly sensitive to the finest features of microstructure.

TE oxides offer many advantages, among them are structural and chemical stability at high temperatures, non-toxicity, and low-cost. Whereas the figures of merit of both Na_xCoO_2 and $\text{Ca}_3\text{Co}_4\text{O}_9$ p-type cobaltates approach unity, which is the criterion of applicability, the ZT -values of their n-type counterparts are significantly lower (~ 0.3 at 1000 K) and should, therefore, be improved.

The present study focuses on Ruddlesden-Popper (RP) $\text{CaO}(\text{CaMnO}_3)_m$ n-type compounds, which are modulated structures formed of m perovskite CaMnO_3 -layers separated by single rock-salt CaO -layers. In this study we aim at drawing the correlation between the thermal conductivity of $\text{CaO}(\text{CaMnO}_3)_m$ -based compounds and the periodicity of the planar CaO defects, denoted by the m -values. We are, additionally, interested in studying the effects of the planar periodicity on the other TE properties, namely electrical conductivity and thermopower.

We prepared several pure, La-, and Nb-doped $\text{CaO}(\text{CaMnO}_3)_m$ compounds having different periodicities by mixing oxide powders followed by multi-step sintering processes at several temperatures up to 1673 K. We characterized the obtained microstructures employing x-ray diffraction (XRD) and high-resolution scanning electron microscopy (SEM). We measured the thermal conductivities of the different compounds applying the laser flash analysis (LFA) technique, as well as the electrical conductivity and thermopower in the range of 300 through 1000 K. We observed a remarkable reduction in thermal conductivity as a result of increasing the CaO-planes density for the RP compounds from a value of $2.9 \text{ W m}^{-1}\text{K}^{-1}$ for $m=\infty$ down to $1.3 \text{ W m}^{-1}\text{K}^{-1}$ for $m=1$ (Nb-doped) at 1000 K. This apparent correlation between thermal conductivity and CaO-planes density is elucidated in terms of phonon scattering, implying how to manipulate lattice thermal conductivity via microstructural modifications. This trend is, however, accompanied by a respective reduction in electrical conductivity values from 76 down to $2.9 \text{ }\Omega^{-1}\text{cm}^{-1}$, which yields an overall decrease of ZT. We conclude that further study concentrating on increasing electrical conductivity by doping should be performed, for optimizing dopant identity and concentrations.

2. Literature review

2.1 Basics of thermoelectricity

The thermoelectric (TE) effect enables direct conversion of heat into electrical power. With TE devices, waste heat and natural heat sources can be utilized to generate electrical power in an environmentally clean way. TE generators are solid state devices with no moving parts, which are lightweight and noiseless, CO₂ emission-free during operation, and durable.^{1,2}

TE power generation is based on the Seebeck effect, a phenomenon discovered in 1821.³ In this effect an open-circuit voltage is formed due to the existence of a temperature difference between two poles of a material. The Seebeck coefficient is defined in Eq. (1).⁴

$$(1) S(T) = \frac{\partial V}{\partial T}$$

A material that possesses a Seebeck coefficient having an absolute value of 150–250 $\mu V/K$ is considered to be a good TE material.⁵

The basic TE generator consists of two semiconductor legs, n-type and p-type, which form a junction, and are connected to an electrical circuit as shown in Fig. 1.⁶ When a temperature gradient is applied on a TE couple, the mobile charge carriers at the hot side (T_H) tend to diffuse to the cold side (T_C), producing an automotive force.

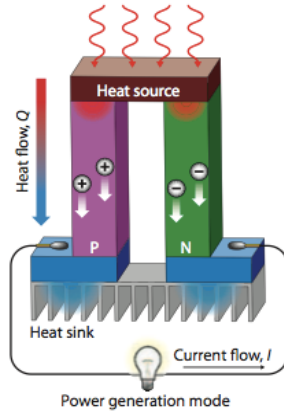


Figure 1: A schematic illustration of a thermoelectric module for power generation (Seebeck effect).⁶

A TE device commonly contains several TE junctions, which are connected electrically in series and thermally in parallel, as shown in Fig. 2.¹

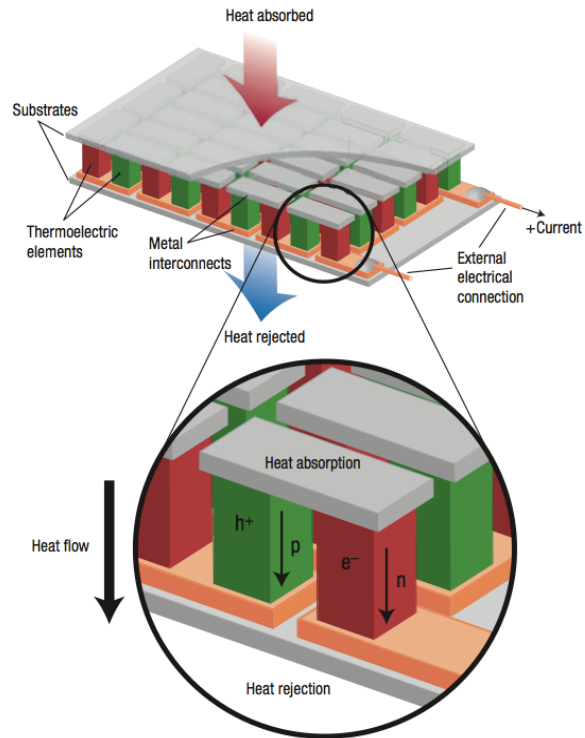


Figure 2: A schematic illustration of a thermoelectric module showing the thermoelements connected electrically in series and thermally in parallel.¹

The energy conversion efficiency of a TE device depends directly on both temperatures of the cold and hot poles (determining the *Carnot* limit) as well as on the dimensionless figure of merit, ZT , which depends on the material's properties, and is given by Eq. (2):^{1,5}

$$(2) \quad ZT = \frac{S^2 \sigma T}{\kappa} \quad ;$$

T is the absolute temperature, and S is the Seebeck coefficient, which is commonly referred to as *thermopower*. σ and κ are the material's electrical and thermal conductivities, respectively. There are two contributions for the thermal conductivity; one is related to phonons due to vibrations, κ_{ph} , and the second to conduction electrons, κ_{el} . The total thermal conductivity is given by Eq. (3):

$$(3) \quad \kappa = \kappa_{ph} + \kappa_{el}$$

The most common TE materials that are currently in-use, such as Bi_2Te_3 , PbTe , CoSb_3 , or SiGe , exhibit ZT values that barely exceed 1.¹ This relatively low value leads to device performance of about 10% of the Carnot limit, where the total efficiency of a TE module is expressed as the product of the Carnot efficiency $\left(\frac{T_H - T_C}{T_H} \equiv \frac{\Delta T}{T_H}\right)$ and a material-dependent factor, as shown in Eq. (4).⁷

$$(4) \quad \eta = \frac{\Delta T}{T_H} \cdot \frac{\sqrt{1 + ZT_{avg}} - 1}{\sqrt{1 + ZT_{avg}} + \frac{T_C}{T_H}}$$

T_H , T_C , ΔT , and T_{avg} are the temperatures of the hot and cold sides, their difference, and their average value, respectively. The dependence of the total efficiency on temperature for several ZT -values, compared to those of other heat engines is displayed in Fig. 3.⁸

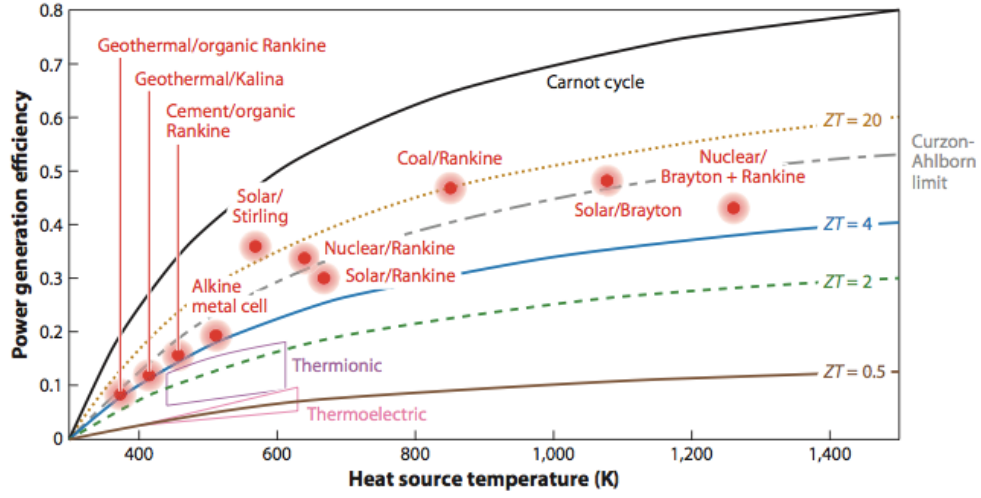


Figure 3: Thermoelectric power generation efficiency versus T_{hot} (for $T_{\text{cold}} = 300$ K). Efficiency for conventional mechanical engines as the Carnot limit are also shown.⁸

Eq. (4) implies that high ZT -values and large temperature differences across the TE unit are required to increase the device efficiency. For achieving high ZT , we require relatively high σ and S -values at the same time with low κ -values. These three magnitudes, in turn, depend on the charge carrier (holes or electrons) concentration, n , as illustrated in Fig. 4.⁹

As the Seebeck coefficient decreases with increasing charge carrier concentrations, the electrical conductivity increases, Eq. (5),¹⁰ and so does the electrical component of thermal conductivity, Eq. (3), as demonstrated by the Wiedemann-Franz law.¹¹

$$(5) \quad \sigma = \frac{1}{\rho} = ne\mu$$

μ denotes the charge carrier mobility, n represents their concentration, ρ is the electrical resistivity and e is an electron charge. For high charge carrier concentration the electrical and thermal conductivities attain their highest values; however, the Seebeck coefficient attains its lowest values. On the other hand, for low charge carrier concentrations, the Seebeck coefficient exhibits its highest values whereas both thermal and electrical

conductivities are the lowest. Thus, an optimum value of charge carrier concentration is required to improve ZT, which can be found in semiconductors.

The product $S^2\sigma$, defined as the *power factor* (PF), which is part of the numerator in the expression for ZT, Eq. (2), is maximized for charge carrier concentrations ranging between 10^{19} and 10^{21} cm⁻³, in the semiconductor region, regardless of the material type.⁴ It turns out that for an optimum n -value, higher ZT can be achieved by lowering the thermal conductivity.

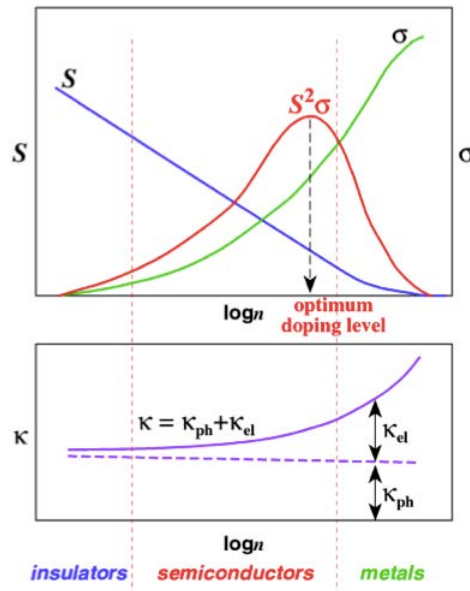


Figure 4: Charge carrier concentration dependence of transport parameters required for optimum thermoelectric performance.⁹

2.2 State-of-the-art TE materials and the interest in thermoelectric oxides

The conventional TE materials are semiconducting compounds consisting of elements such as Bi, Te, Pb, and Sb. The common compounds for near room temperature applications up to 200°C are n-type Bi₂Te₃ and p-type Sb₂Te₃. Their maximum ZT-values range between 0.8 and 1.1, as shown on Fig. 5.¹ For the mid-temperature range (500-900

K), the highest ZT values are obtained for materials based on group-IV-tellurides, such as PbTe, GeTe and SnTe. For temperatures higher than 900 K, the most widely used TE materials are silicon-germanium compounds.

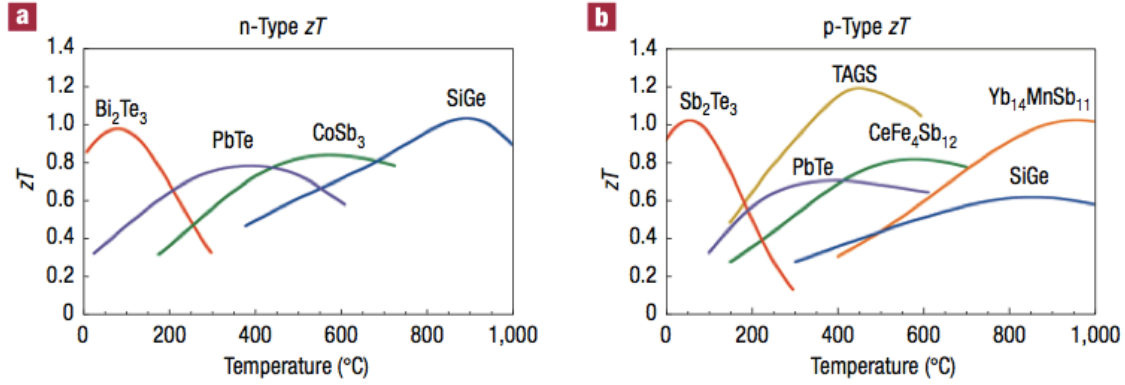


Figure 5: The temperature-dependent ZT- values of (a) n-type and (b) p-type compounds. Approximate compositions are presented.¹

The above classic TE materials are incapable of extensive TE applications because of their toxicity, low stability at high temperature in air due to either low melting temperatures or volatility, low abundance and high cost, as exemplified in Fig. 6.¹² Oxide thermoelectric compounds, on the other hand, are promising candidates owing to several advantages; among them is non-toxicity, high thermal stability in air, and low cost. The major drawback of such TE oxides is, however, their relatively low ZT-values.⁹ This situation has changed since the discovery of layered cobalt oxides, such as $\text{Na}_x\text{Co}_2\text{O}_4$ ¹³ and $\text{Ca}_3\text{Co}_4\text{O}_9$ ¹⁴, both are p-type, with figures of merit that approach unity (at 1000 K). These high ZT values are due to their high thermopower and PFs, coupled with a low thermal conductivities.¹⁵ In contrast, the ZT-values of the best n-type oxide are still lower (~ 0.3 at 1000 K) despite continuing efforts^{12,16} as shown in Fig. 7.⁹ Improving the ZT-values of the best n-type TE oxides and searching for new ones is, therefore, of great technological importance.

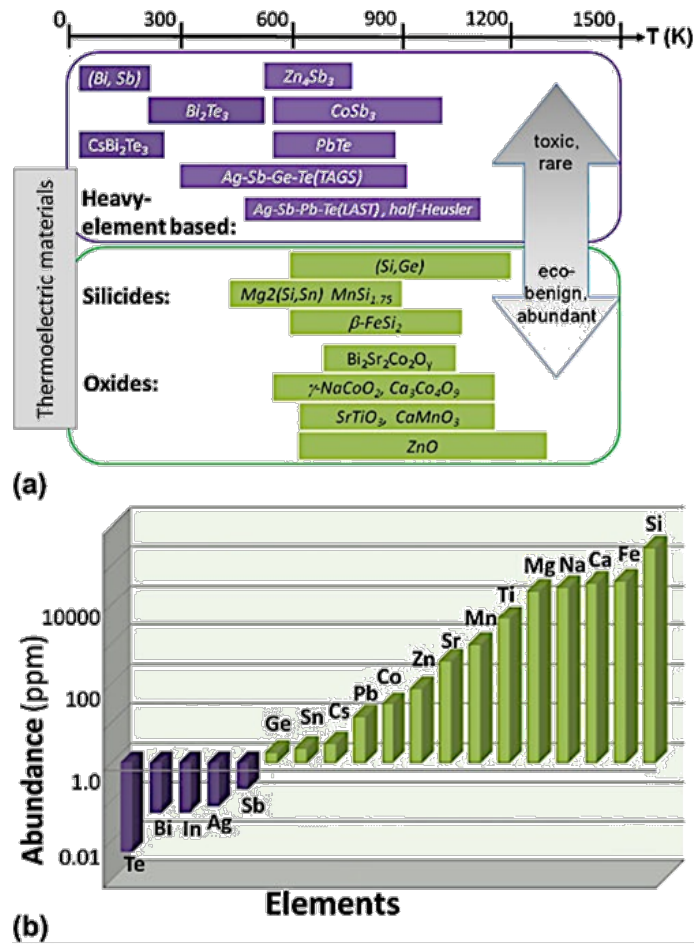


Figure 6: (a) Schematic comparison between different thermoelectric materials for waste heat harvesting, in terms of the temperature range of operation, abundance, and environmental friendliness of their constituent elements. (b) The abundance of elements present in TE materials. Elements represented by dark-colored columns exhibit abundance of <1 ppm.¹²

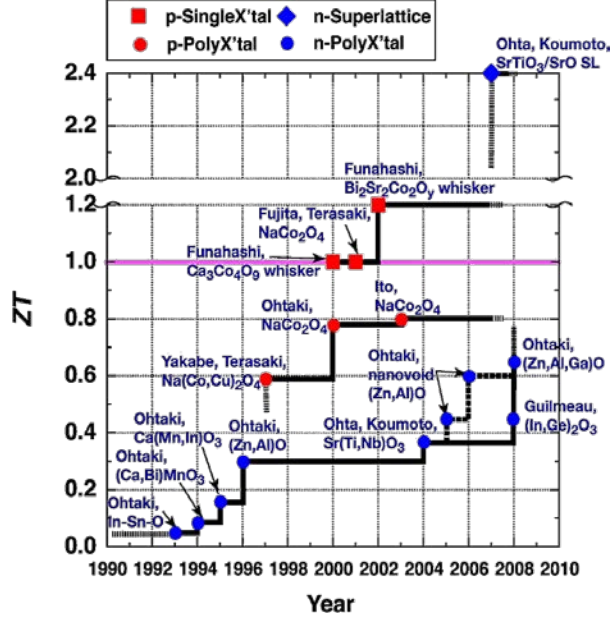


Figure 7: The timeline of the development of the highest ZT-values of oxide thermoelectric materials.⁹

2.3 Thermal conductivity in crystalline solids

In this section we introduce the fundamentals of heat conduction in crystals, followed by a description of a model for lattice thermal conductivity that is widely used in the TE field, as well as in the present study.

2.3.1 Fundamentals of thermal conductivity

The total thermal conductivity in crystalline solid materials comprises two components, related to electrons and phonons, as mentioned in Eq. (3).

The electronic contribution for either metal or degenerate n-type or p-type semiconductors is shown in Eq. (6):¹¹

$$(6) \quad \kappa_e = \frac{\pi^2}{3} k_B^2 \frac{n_{e/h} \tau_{e/h}}{m_{e/h}}$$

where k_B is the Boltzmann constant, $n_{e/h}$ is the electron or hole concentration, $\tau_{e/h}$ is

their relaxation time, i.e the average time between two successive scattering events, and $m_{e/h}$ is their effective masses. The classical kinetic theory provides a good approximation for the lattice thermal conductivity, as presented in Eq. (7):¹⁷

$$(7) \quad \kappa_p = \frac{1}{3} \cdot C_v \cdot l \cdot v_s$$

Here, C_v is the constant-volume specific heat (heat capacity), v_s is the average sound velocity, and l is the phonon mean free path, which is estimated as the average distance that a single phonon passes between two successive scattering events. Phonon scattering events can be classified into two main categories: scattering by lattice defects, such as internal boundaries, impurity atoms, strain fields, precipitates, dislocations, etc.; and scattering by other phonons via *Normal* (N) or *Umklapp* (U) processes. In the N-processes, there is no change in the phonon momentum during the interactions, while the U-processes are non-momentum conserving processes.^{10,11} Each scattering mechanism is characterized by its own relaxation time, which is highly dependent on the material. Matthiessen's rule suggests that the equivalent inverse phonon relaxation time in a system with distinct scattering mechanisms is the sum of the inverse relaxation times corresponding to the individual mechanisms, Eq. (8):¹⁸

$$(8) \quad \frac{1}{\tau} = \sum_i \frac{1}{\tau_i}$$

The Debye model provides an estimation of the phonon contribution to the specific heat in a solid. In this approach, lattice vibrations are treated as phonons in a confined volume, as compared to Einstein's theory, in which the crystalline solid is considered as an accumulation of harmonic oscillators that vibrate with the same frequency. According to the Debye theory, the Debye temperature, T_D , is defined as the temperature in which the highest vibrational mode is occupied, and is given by Eq. (9):¹⁹

$$(9) \quad T_D = \frac{h v_D}{k}$$

Where h is Planck's constant and v_D is the Debye frequency.

The behavior of κ_p at very low temperatures ($T \ll T_D$) is dominated by the heat capacity, which scales as T^3 . U-processes are insignificant at this temperature range. However, at high temperatures ($T \gg T_D$) C_V approaches the classical value of $3R$, namely the Dulong-Petit limit,¹¹ meaning that κ_p primarily depend on l (see Eq. 6). l is determined by phonon-phonon scattering, and depends inversely on the density of phonons that interact. It turns out that for high temperatures κ_p is proportional to T^{-1} .

2.3.2 The Callaway model for thermal conductivity

Several models have been proposed to describe the temperature-dependence of lattice thermal conductivity; among them is the Callaway model that was developed in 1959,²⁰ and has been commonly used in the field of TE materials to correlate between the material micro/nano-structure and the lattice thermal conductivity.^{21–26}

In the Callaway model an isotropic Debye-like phonon spectrum is assumed, i.e. no distinction between longitudinal and transvers phonons; also, the phonon branches are non-dispersive. This model is, therefore, predictive for the frequency range where the Debye-like phonon spectrum prevails. The Callaway model essentially integrates the product $C_v \cdot l$ of Eq. (7) over the entire phonon frequency range up to the Debye frequency, and expresses the phonon thermal conductivity for temperatures above T_D in the following form:²⁷

$$(10) \quad \kappa_p(T) = \frac{k_B}{2\pi^2 v_s} \left(\frac{k_B T}{\hbar} \right)^3 \int_0^{T_D/T} \tau_t(x) \frac{x^4 e^x}{(e^x - 1)^2} d\omega$$

Where ω is the phonon angular frequency, \hbar is the reduced Planck's constant: $\hbar/2\pi$, $x \equiv \frac{\hbar\omega}{k_B T}$ and τ_t is the equivalent relaxation time. The latter is calculated considering the relaxation times for the relevant scattering processes according to Eq. (8). The main scattering mechanisms that are commonly taken into account are scattering from boundaries, dislocations, strains, nanometer-scale precipitates, and the phonon-phonon interactions;²⁷

$$(11) \quad \frac{1}{\tau_t} = \frac{1}{\tau_U} + \frac{1}{\tau_N} + \frac{1}{\tau_B} + \frac{1}{\tau_D} + \frac{1}{\tau_P} + \frac{1}{\tau_S}$$

Where τ_U , τ_N , τ_B , τ_D , τ_P and τ_S correspond to relaxation times for scattering in the U- and N-processes, and from boundaries, dislocations, precipitates, and strain fields, respectively.^{22,28-31} In our research, we consider the contributions of only two mechanisms, which are the U-processes and the scattering from internal boundaries.²⁶ The relaxation time for U-processes is expressed by:²⁸

$$(12) \quad \tau_U^{-1} \approx \frac{\hbar \gamma^2}{M v_s^2 T_D} \omega^2 \exp\left(\frac{-T_D}{3T}\right)$$

where γ is the Grüneisen parameter that reflects the lattice anharmonicity, and M is the average atomic mass. For boundary scattering, the relaxation time is approximated by:

$$(13) \quad \tau_B^{-1} \approx \frac{v_s}{L} ,$$

Where L is a characteristic length, which is approximated by the grain size.

2.3.3 The microstructure-thermal conductivity relationship

As shown before, a very high electrical conductivity is not always an advantage, despite the linear dependence of the PF on electrical conductivity, because of the resultant increase in the electronic contribution to the thermal conductivity.³² The electrical conductivity scales linearly with the carrier thermal conductivity κ_{el} , as implied by the Wiedemann-Franz relationship. This means that both conductivities are inter-related; therefore, lowering electrical conductivity without significantly damaging the thermal conductivity is difficult to achieve. An efficient strategy to achieve this goal is maximizing ZT by manipulating the lattice thermal conductivity alone, which is the only parameter that is independent of electronic structure, to a good approximation.¹⁵ The electrical conductivity and Seebeck coefficient are, conversely, associated to the electronic structure and in most cases cannot be optimized independently.⁹

Slack et al. suggested the concept of maximizing ZT by forming a “phonon glass electron crystal” (PGEC) system, having a high carrier mobility combined with minimum lattice thermal conductivity.⁴ According to the PGEC approach, materials having “cages” or “tunnels” inside their crystal structure, and comprising massive or large atoms, will potentially exhibit low-thermal conductivity values. This structure allows the atoms to “rattle” in the cages, which damp phonon vibrations and, thereby, reduce lattice thermal conductivity. PGEC materials exhibit this property together with high mobility of charge carriers. Prominent examples for compounds that are engineered based on the PGEC approach are clathrates and skutterudites.^{1,4,33}

An additional approach to reduce lattice thermal conductivity is by controlling the lattice periodicity (i.e. enlarging the unit cell parameters), thereby shortening the phonon mean free paths.¹⁵ This strategy is being utilized for complex structures with large unit cells such as ternary and quaternary bismuth chalcogenides.³⁴

Another strategy applied for reducing the lattice thermal conductivity is phonon scattering by formation of nanostructured features such as thin films, superlattices, bulk materials with nano scale precipitates, nano-wires and quantum dots.^{35–39} The latter affects electronic density of states, as well. Phonon scattering from lattice imperfections such as phase boundaries, interphase dislocations and precipitates,^{21,26,27,40–43} can also decrease the thermal conductivity.

2.4 The interest in Ruddlesden Popper phases

Metal oxides have proven to be promising candidates for TE applications, especially layered cobaltate structures, i.e., Na_xCoO_2 ¹³ and $\text{Ca}_3\text{Co}_4\text{O}_9$ ¹⁴ as well as perovskite-type phases, with the general formula ABO_3 ; where A is a rare-earth or alkaline metal and B is a transition metal. A and B can be selected from a wide variety of elements. Perovskite-type phases such as, for example, manganate,⁴⁴ titanate,⁴⁵ or cobaltate⁴⁶ phases exhibit relatively large Seebeck coefficients ranging from ~100 to ~550 $\mu\text{V}/\text{K}$ at 300 K. This is an essential prerequisite for a good TE material. In particular, electron-donor-doped manganates exhibit good TE performance at elevated

temperatures up to 1000 K. ^{47–58} The TE properties of CaMnO_3 -based compounds in which either the A- or B-sites contain substituting elements have been widely investigated. ^{48,52,54,59,60} Recent studies on the new n-type Nb-doped CaMnO_3 phase reveal ZT value of 0.32 at 1070 K in air. ⁶⁰ This suggests that doped manganates can serve as a good starting point for the search of new base n-type materials for TE applications. Their relatively low ZT values compared to state-of-the-art lead-chalcogenide compounds make their development challenging. ⁶¹ Reducing their electrical resistivity can be accomplished by slight cationic or anionic substitutions. ^{62,63} Since phonons dominate heat conductivity in metal-oxide materials, ⁶⁰ different strategies are utilized to reduce lattice thermal conductivity by phonon scattering, as explained in Section 2.3.3. Another promising approach to reduce κ is to design layered materials or superlattices. ^{64–66} The key point in reducing κ of superlattices is controlling the density of interfaces that scatter phonons.

In this study we focus on superlattices of the Ruddlesden-Popper (RP)-type compounds, which are modulated microstructures with the general formula $\text{AO}(\text{AMO}_3)_m$ (A -a rare earth or alkaline earth metal, M -a transition metal and O -oxygen). ^{67–71} This layered structure is formed of m perovskite AMO_3 layers separated by one rock-salt AO layer, as shown in Fig. 8. It is hypothesized that the thermal conductivity of these oxides can be manipulated by altering the density of the $\text{AO}/(\text{AMO}_3)_m$ interfaces (number of interfaces per unit length). In this study, we investigate the TE properties of La- and Nb-doped $\text{CaO}(\text{CaMnO}_3)_m$, in which these dopants preferentially substitute for either the A or B sublattice site, respectively. The crystallographic data of the compounds investigated in our study are summarized in Table 1.

Substitution of La^{3+} at the A site or Nb^{5+} at the B site in the $\text{CaO}(\text{CaMnO}_3)_m$ matrix induce the formation of Mn^{3+} cations in the Mn^{4+} matrix, resulting in n-type conduction. ^{70,72} The thermoelectric properties of La- and Nb-doped RP phases are expected to be sensitive to the superlattice periodicities (m -values), which sets the framework of our study reported in this research thesis.

Sample	m	Crystal structure	Space group	JCPDS number	a (Å)	b (Å)	c (Å)
CaMnO ₃	inf	Orthorhombic	Pnma	040078030	5.282	5.277	7.459
Ca ₄ Mn ₃ O ₁₀	3	Tetragonal	I4/mmm	000180298	5.258	5.258	26.807
Ca ₃ Mn ₂ O ₇	2	Tetragonal	I4/mmm	040165273	3.703	3.704	19.449
Ca ₂ MnO ₄	1	Tetragonal	I4/mmm	040067894	3.667	3.667	12.060

Table 1: Room temperature crystallographic data for the CaO(CaMnO₃)_m-compounds with $m=1, 2, 3$, and ∞ (inf).

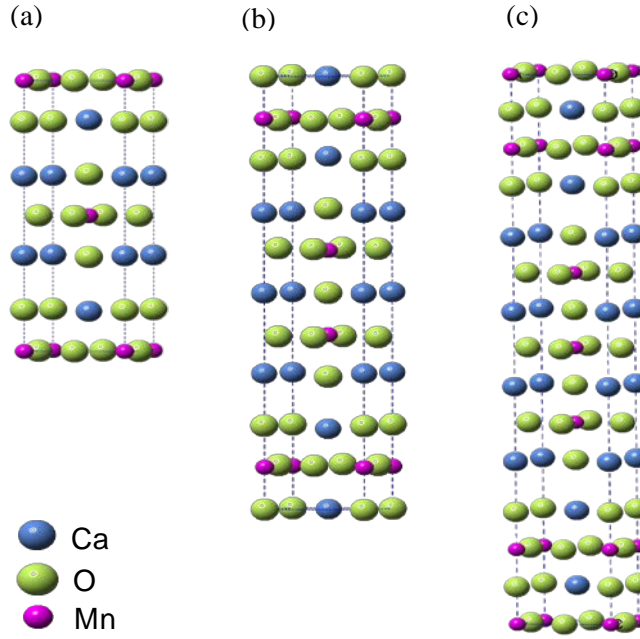


Figure 8: A schematic illustration of the crystal structure of CaO(CaMnO₃)_m Ruddlesden-Popper compound for (a) $m=1$, (b) $m=2$, (c) $m=3$, showing the layering between the CaMnO₃ perovskite and CaO rock-salt structures. The periodicities of $m=1$ through 3 are denoted by a tetragonal-crystal structure having the $I4/mmm$ symmetry space group (JCPDS numbers: 040067894, 040165273, and 000180298 for $m=1, 2$, and 3 , respectively).

2.5 Summary

One of the directions in the search for alternative energy sources is capturing waste heat and converting it into electricity using thermoelectric (TE) generators. An efficient TE material is characterized by high TE *figure of merit*, ZT , requiring a large Seebeck coefficient (thermopower), high electrical conductivity, and low thermal conductivity; these properties are highly sensitive to the finest features of microstructure. TE oxides offer many advantages, among them are structural and chemical stability at high temperatures, non-toxicity, and low-cost. Whereas the figure of merit of both Na_xCoO_2 and $\text{Ca}_3\text{Co}_4\text{O}_9$ p-type cobaltates approaches unity, which is the criterion of applicability, the ZT -values of their n-type counterparts are significantly lower (~ 0.3 at 1000 K) and should, therefore, be improved.

The present study focuses on Ruddlesden-Popper (RP) $\text{CaO}(\text{CaMnO}_3)_m$ n-type compounds, which are modulated structures formed of m perovskite CaMnO_3 layers separated by a single rock-salt CaO layer. In this study we aim at drawing the correlation between the thermal conductivity of $\text{CaO}(\text{CaMnO}_3)_m$ -based compounds and the periodicity of the planar CaO defects, denoted by the m -values, and investigating the influence of these crystal structures on the other TE properties.

2.6 Research goals

We hypothesize that introducing extra CaO -planes within the perovskite CaMnO_3 -based crystal should scatter heat-carrying phonons, thereby reducing lattice thermal conductivity. The primary goal of this research is to manipulate lattice thermal conductivity of different RP-based $\text{CaO}(\text{CaMnO}_3)_m$ compounds by determining the periodicity of the CaO -planes, and to investigate their effects on thermoelectric performance. This goal will be accomplished by formation of $\text{CaO}(\text{CaMnO}_3)_m$ compounds with different m -values and experimental measurements of their temperature-dependent thermal conductivity, electrical conductivity, and Seebeck coefficient, and drawing the correlation between these functional properties and the materials microstructures.

The secondary goal is to study the effects of La- and Nb- doping on the above thermoelectric properties. Both research goals are oriented toward improving the material TE figure of merit.

3. Experimental and analytical methods

In this section we describe the experimental and computational methods applied in this study, including details on materials synthesis and characterization. The latter include both microstructure characterization and thermoelectric measurements.

3.1 Sample preparation

Two groups of compounds made of $\text{CaO}(\text{Ca}_{1-x}\text{La}_x\text{MnO}_3)_m$ with $m=1,2,3$, and ∞ and $\text{CaO}(\text{CaMn}_{1-x}\text{Nb}_x\text{O}_3)_m$ with $m=1,2,3,4,5$, and ∞ were synthesized from pure oxide powders mixed in the appropriate stoichiometric ratios. The two main raw oxide powders used for preparation of the undoped compounds include calcium carbonate (CaCO_3) powder having $\sim 14 \mu\text{m}$ average particle size (Merck KGaA Co. 64271 Darmstadt, Germany), and manganese dioxide, MnO_2 (Baker Co.). The major impurities ($>0.01 \%$) in CaCO_3 declared by the manufacturer are: SO_4 ($<0.03 \%$), Mg ($<0.02 \%$), Na ($<0.2 \%$), and Sr ($<0.1 \%$). The major impurities in MnO_2 declared by the manufacturer are: Cl ($<0.01 \%$), NO_3 ($<0.05 \%$), SO_4 ($<0.05 \%$), and Fe ($<0.03 \%$). Doping was performed by mixing of either La_2O_3 or Nb_2O_5 pure powders with the above CaCO_3 and MnO_2 raw powders in the appropriate ratios to obtain a doping level of $x=4 \text{ at.}\%$ for both classes of compounds. We will further use the acronym *inf.* to denote the $m=\infty$ structure.

Both classes of compounds were prepared using a standard solid state reaction protocol⁷⁰ that includes mixing the powders and room-temperature, uniaxial pressing under pressure of 900 MPa to form both pellet- (12.5 mm dia. and ca. 2 mm thick) and bar- (2×2×12.5 mm) shaped specimens, followed by sintering in air at several stages with increasing temperatures ranging from 950 up to 1400 °C, which are optimized for each compound, for 24 hours in each step. The process was determined by sintering at a given temperature and re-grinding to fine powder, followed by X-ray diffraction (XRD) analysis to make sure that the desirable, single-phase RP compound was obtained. This process was repeated at the following optional temperatures with intermediate grinding steps: 950, 1100, 1200, 1300, 1350, and 1400 °C until the desirable material was obtained. Finally, all sintered pellet- or bar-shaped specimens were air-cooled. Table 2

summarizes the nominal stoichiometries of the undoped, La-doped, and Nb-doped compounds that were synthesized.

Doping	Lattice periodicity (m-value)					
	inf	1	2	3	4	5
Undoped	✓	✓	✓	✓		
La-doped	✓	✓	✓	✓		
Nb-doped	✓	✓	✓	✓	✓	✓

Table 2: the nominal stoichiometries of the undoped, La-doped, and Nb-doped compounds that were synthesized, denoted by $m=\infty$ (inf.), and 1 through 5.

3.2 Microstructure analysis

3.2.1 X-ray diffraction (XRD)

XRD measurements were carried out using a Siemens D5000 powder diffractometer with an angular resolution of 0.02° , located at the Physics Department, Technion, applying Cu-K α radiation at the angular range of $2\theta = 10-60^\circ$. The data were collected by angular scanning with 0.03° steps.

3.2.2 High-resolution scanning electron microscopy (HR-SEM)

Microstructure characterization of the samples was carried out using a Zeiss Ultra Plus high-resolution scanning electron microscope (HR-SEM) that is located at the Materials Science & Engineering Department, equipped with a Schottky field-emission electron gun. The images presented in this study were taken with a secondary electron detector, operated at 4 keV.

3.2.3 Grain size analysis

The grain boundaries were marked manually on HRSEM micrographs. We characterized the dimensions of the elongated grains using a Matlab © code employing ellipses that are circumscribed in each grain, representing both long and short elliptical

axes. The Matlab code was developed by Mr. Elad Joseph of the Technion Thermoelectric Materials Laboratory.

3.2.4 Density measurements

The samples' bulk density values were calculated from measurements of the specimens' weight using balance with 1 mg accuracy and their volume using caliper with 0.01 mm accuracy. This yields a 1% relative accuracy in the calculated densities.

3.3 Thermoelectric characterization

We performed physical measurements that are divided into two main categories: electrical and thermal measurements. The electrical measurements include both electrical conductivity and Seebeck coefficient (thermopower), and the thermal measurements include thermal diffusivity and heat capacity.

3.3.1 Electrical conductivity and thermopower measurements

The temperature-dependent electrical conductivity, σ (T), and thermopower, S (T), were measured employing the D.C. standard four-point-probe (4pp) method⁷³ for the bar-shaped specimens in the temperature range of 80-300 K using a self-engineered device at Prof. Bertina Fisher's laboratory, Physics Department, Technion. Further electrical analysis in the temperature range of 300 through 1000 K was performed at the NETZSCH-Gerätebau GmbH laboratory (Selb, Germany) employing the *Nemesis SBA-458* apparatus that is designed for simultaneous measurements of electrical conductivity and thermopower for planar geometry. This apparatus is currently at its final stages of development, and is not commercial yet.

3.3.1.1 Electrical conductivity measurement for bar-shaped specimens

The 4pp method is one of the simplest and most conventional methods for electrical resistivity measurements. The concept of the measurement is illustrated in Fig. 9. In the 4pp method electrical current is passed between two outer probes and the resulted voltage is measured between the inner two probes, with a high resistance

voltmeter. In this manner, the contact resistivity does not have an influence on the measurement.

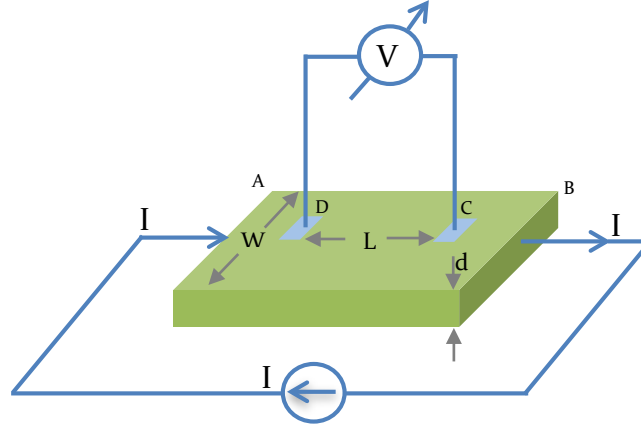


Figure 9: A schematic description of the 4pp technique for electrical conductivity measurement

The average resistance, R , between contacts D and C is calculated from the Ohm Law as:

$$(14) \quad R = \frac{V}{I}$$

where V is the voltage prevailing between contacts D and C, and I is the electrical current. For a specimen having a length L and a cross-sectional area A , the electrical resistivity, ρ , is given by:

$$(15) \quad \rho = \frac{A}{L} R = \frac{W d}{L} R$$

The electrical conductivity, σ , is represented by:

$$(16) \quad \sigma = \frac{1}{\rho},$$

And is regularly given in units of $\Omega^{-1}\text{cm}^{-1}$ or $\text{S}\cdot\text{cm}^{-1}$.

3.3.1.2 Thermopower measurements for bar-shaped specimens

The Seebeck coefficient of a material, as defined by Eq. (1), denotes the

magnitude of the induced thermoelectric voltage in response to a temperature difference across it. The measurement principle is illustrated in Fig. 10. A bar-shaped sample ($\sim 2 \times 2 \times 10 \text{ mm}^3$) is set in a vertical position between both upper and lower blocks of a furnace. While the entire specimen is heated up to a given temperature, a local heater heats up one pole only, one at a time, to provide a temperature difference between both poles. After the temperature difference along the specimen reaches at a steady state, the Seebeck coefficient is derived from the built-in voltage divided by the temperature difference.

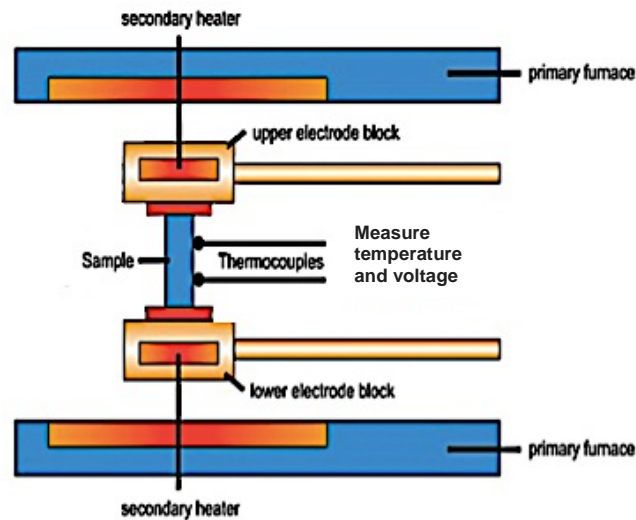


Figure 10: A schematic description of the Seebeck coefficient measurement setup applied at the Physics Department, Technion.

3.3.1.3 Electrical conductivity measurement for planar specimens

The Netzsch SBA-458 system is a newly-developed instrument that simultaneously measures both electrical conductivity and the Seebeck coefficient for thin films and bulk materials having any planar geometry (ca. 10 through 25.4 mm dia.), at temperatures ranging from 300 to 1050 K. Measurements are done under flowing, high-purity (5N) Ar. As the furnace reaches at a given temperature set point, a measurement of the electrical conductivity takes place using the electrical contacts. Afterwards, the two micro heaters generate a temperature difference along the sample and measurement of the Seebeck coefficient takes place.

The sheet resistivity of a sample is determined by a method called “linear four terminal arrangement”. According to Smits and Valdes,⁷³ the sheet resistivity of quasi-infinite sized sheets is given by Eq. (17):

$$(17) \quad \rho = \frac{\Delta V}{I} \frac{2\pi}{\left(\frac{1}{s_1} + \frac{1}{s_3} - \frac{1}{s_1 + s_2} - \frac{1}{s_2 + s_3}\right)}$$

where the s_i - parameters are the spacings between the probes at the sample holder. For the present configuration, these distances are: $s_1=s_3=1.5$ mm, and $s_2=7.8$ mm, which leads to a simplified formula given by Eq. (18):

$$(18) \quad \rho = \frac{\Delta V}{I} \frac{2\pi}{\left(\frac{1}{s_1} - \frac{1}{s_1 + s_2}\right)}$$

Due to the specimens' finite dimensions, scattering factors have to be considered in the calculation of the resistivity, having the form:

$$(19) \quad \delta_x = \sum A_n \cdot e^{-x/t_n}$$

where x stand for either the thickness, width or length. The corrected expression for resistivity is, therefore:

$$(20) \quad \rho_{final} = \frac{\rho}{\delta_x \cdot \delta_y \cdot \delta_z}$$

The scattering factors are obtained from the theory of mirror charges in electrostatics, and usually cannot be determined analytically. Therefore, finite element analysis is applied to determine the scattering factors for the present sample geometries, and this code is automatically applied by the SBA-458 analysis interface for a given specimen geometry. The sample thickness range for this evaluation is limited to the range of 10 μ m through 2 mm.

3.3.1.4 Thermopower measurements for the planar geometry

Measurements of the Seebeck coefficient are performed using two differential thermocouples, where one of the junctions of each thermocouple is juxtaposed onto the sample, and the other junction is placed at a reference temperature T_{REF} (both on the same T_{REF}), as shown in Fig. 11.

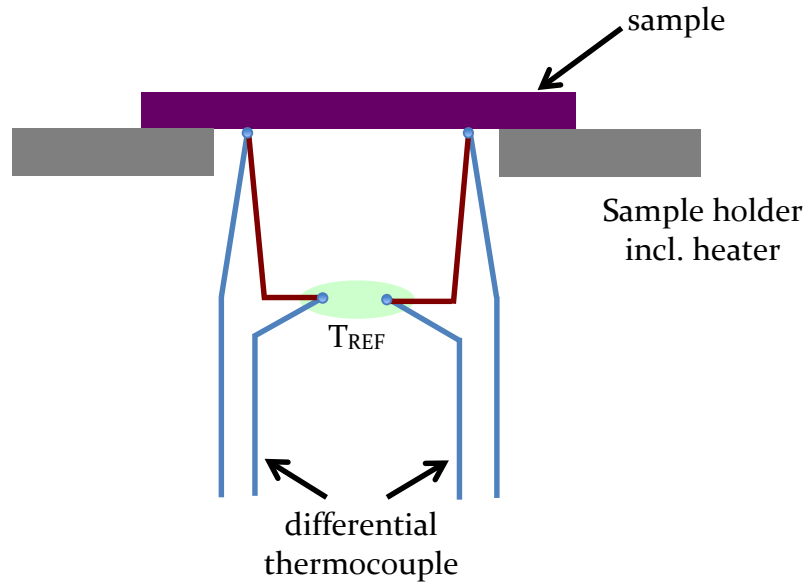


Figure 11: A schematic description of the SBA-458 Seebeck coefficient measurement setup.

This measurement setup allows a simple way of determination of the Seebeck coefficient of a sample, since it is reduced to the configuration shown in Fig. 12.

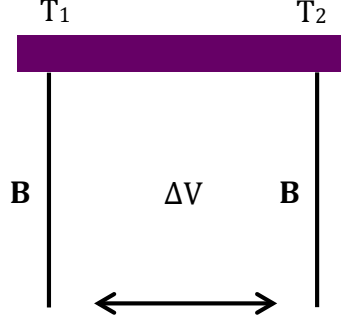


Figure 12: A typical configuration for the measurement of the Seebeck coefficient.

External heaters produce a temperature difference of $T_2 - T_1$ on the sample, and the voltages at these positions are probed, as well. The Seebeck coefficient is then calculated using Eq. (21), given the Seebeck coefficient of material B (S_B).

$$(21) \quad S - S_B = \lim_{\Delta T \rightarrow 0} \frac{\Delta V}{\Delta T}$$

where $\Delta T = T_2 - T_1$

3.3.2 Thermal conductivity measurements

We determine the materials' thermal conductivity, κ , by measuring their thermal diffusivity, α , specific heat, C_p , and density, ρ , as a function of temperature; κ is expressed by ⁴:

$$(22) \quad \kappa(T) = \alpha(T) \cdot \rho \cdot C_p(T)$$

We employ the Netzsch *Microprobe* LFA-457 system to directly measure the thermal diffusivity of pellet-shaped specimens. This instrument is based on the “half-time” method, as described in figure 13, where a thermal pulse is generated by a 18.5 J/pulse Nd-YAG laser system (pulse duration 0.5 ms) onto the sample's surface on one side, and the thermal response is detected using one of the two user interchangeable mercury-cadmium-telluride or indium-antimonide infra-red detectors. The thermal signal is then temporally resolved on the opposite side of the specimen, thus yielding the temperature-dependent thermal diffusivity, as follows:

$$(23) \quad \alpha(T) = 0.1388 \cdot \frac{d^2}{t_{0.5}};$$

where d is the sample's thickness and $t_{0.5}$ is the characteristic time at which the thermal signal reaches 50% of its intensity.

The main features of the LFA-457 system are:

- Temperature range: -125 to 1100 °C;
- Thermal conductivity range: 0.1 to 2000 Wm⁻¹K⁻¹;
- Thermal diffusivity range: 0.01 to 1000 mm²s⁻¹;
- Accuracy: $\pm 2\%$ in thermal diffusivity, and $\pm 3\%$ in thermal conductivity;
- Dimensions of samples: round having 6, 10, 12.5, and 25.4 mm dia., and <5 mm thick.

In the current experimental procedure we measured thermal conductivity in the range of 300–1000 K using an indium-antimonide detector. The temperature-dependent heat capacity is simultaneously measured in the LFA by a comparative method using a pure reference Al₂O₃-sample having similar geometry.

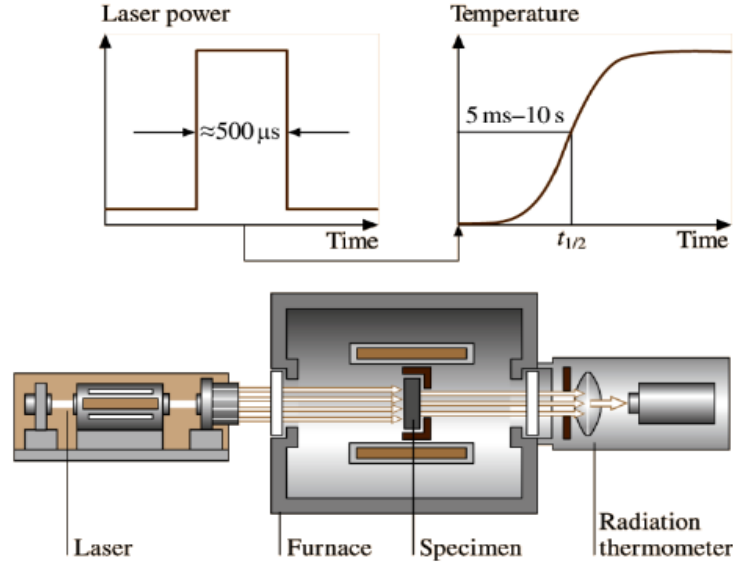


Figure 13: A schematic description of the laser flash analysis (LFA) method.

3.4 First-principles calculations

In this study we employ first-principles calculations of the average sound velocities and Debye temperatures for the undoped RP phases with $m = 1, 2, 3$, and ∞ , to be utilized as input for the model applied by us for analyzing our thermal conductivity results in the Discussion Section. The following is a description of the outline of first-principles calculations.

The fundamentals of quantum mechanics state that the wave function of any physical system contains all information about the system, including energy, momentum, position, and particle density. Solving the Schrödinger equation (SE) for a wave function representing a many-body system (tens to hundreds of atoms, each incorporates tens of electrons) is much beyond the capabilities of modern computational methods.⁷⁴ The density functional theory (DFT) addresses this problem by transition from solving the many-body (N -particles) SE having $3N$ degrees of freedom (DOFs) to solving a set of N Kohn-Sham equations, each having only three DOFs.^{75–79} Thus, DFT enables us calculating a lattice internal energy and electronic structure, or any physical property derived from them.

We perform DFT calculations utilizing the Vienna *ab initio* simulation package (VASP),^{80–82} and the *MedeA* software environment,⁸³ employing the PBE energy functional based on the generalized gradient approximation (GGA) to express the exchange-correlation energy,⁸⁴ as well as the projector augmented wave (PAW) potentials to represent the core electron density.⁸⁵ We utilize a plane-wave basis set with 400 eV energy cutoff to represent the Kohn–Sham wave functions, and set a uniform 9×9×3 Monkhorst–Pack *k*-point mesh.^{76,86} We optimize the structure of the simulated phases with force convergence of ionic relaxations set to 10^{−5} eV·Å^{−1} and energy convergence threshold of 10^{−6} eV.

We further calculate the lattice elastic constants from the total energy variations resulted in response to a 0.005 strain, which is applied along the principal axes. The resulting three independent elastic constants C_{11} , C_{12} , and C_{44} of the RP phases yield the shear and bulk moduli, G and K , respectively. The transverse, v_t , and longitudinal, v_l , sound velocities are calculated directly from the elastic constants and the lattice density, ρ ,^{87,88} as follows:

$$(24) \quad v_t = \sqrt{\frac{G}{\rho}}$$

and:

$$(25) \quad v_l = \sqrt{\frac{K + \frac{4}{3}G}{\rho}}$$

The average sound velocity is calculated from:^{89,90}

$$(26) \quad v_m = \left[\frac{1}{3} \left(\frac{2}{v_t^3} + \frac{1}{v_l^3} \right) \right]^{-1/3},$$

which is averaged over the one longitudinal and two transverse phonon modes. We calculate the Debye temperature as well, which is given by:¹¹

$$(27) \quad T_D = \frac{h}{k_B} \left(\frac{6\pi^2 N}{V_0} \right)^{1/3} v_m$$

where N is the number of atoms in the unit cell of the volume V_0 .

4. Results

This chapter displays the experimental results acquired in this study, and consists of two sections. The first one, 4.1, refers to microstructure characterization using X-ray diffraction for phase identification (4.1.1) and scanning electron microscopy for defect and grain size analysis (4.1.2 and 4.1.3). The second one, 4.2, introduces thermoelectric characterization, including electrical conductivity (4.2.1), thermopower (4.2.2), and thermal conductivity measurements (4.2.3).

4.1 Microstructure characterization

4.1.1 X-ray diffraction (XRD) analysis

We performed XRD analyzes for the specimens sintered in the multi-stage process detailed in Chapter 3 to make sure that we obtained the desirable RP single-phase materials. The XRD patterns presented in figures 14-24, show that all of the undoped compounds as well as the Nb-doped ones of the $m=1,2,3$ and inf type, as well as the La-doped ones of the $m=1,2$ and inf type exhibit the expected single-phase states, as follows:

- The XRD patterns taken from the undoped, La-doped, and Nb-doped compounds of the $m=\text{inf}$ periodicity fit the orthorhombic crystal structure having the Pnma space group symmetry (JCPDS number: 040078030).
- The XRD patterns taken from the undoped, La-doped, and Nb-doped compounds of the $m=1$ periodicity fit the tetragonal crystal structure having the I4/mmm space group symmetry (JCPDS number 040067894).
- The XRD patterns taken from the undoped, La-doped, and Nb-doped compounds of the $m=2$ periodicity fit the tetragonal crystal structure having the I4/mmm space group symmetry (JCPDS number: 040165273).
- The XRD patterns taken from the undoped and Nb-doped compounds of the $m=3$ periodicity fit the tetragonal crystal structure having the I4/mmm space group symmetry (JCPDS number: 000180298)

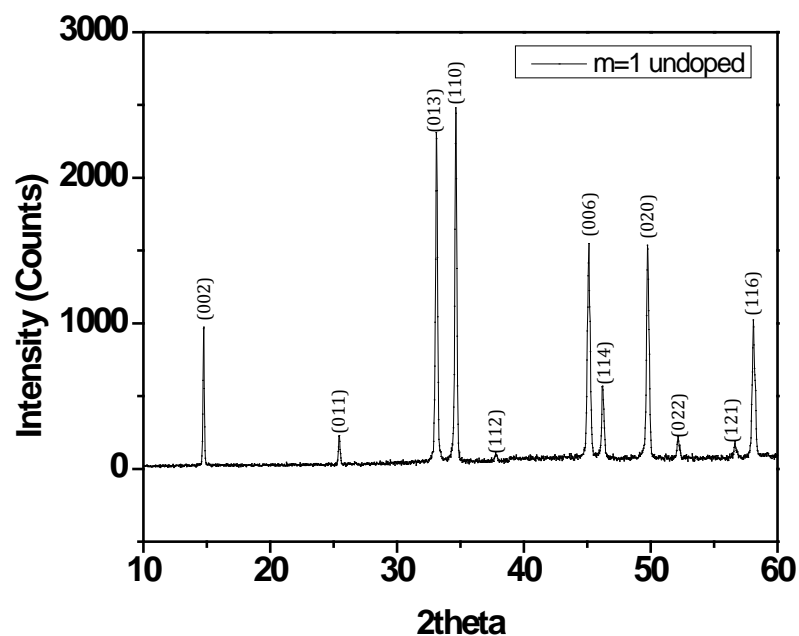


Figure 14: An X-ray diffraction (XRD) pattern acquired from the undoped compound of the m=1 periodicity, fitting the tetragonal-crystal structure having the I4/mmm-symmetry (JCPDS number 040067894).

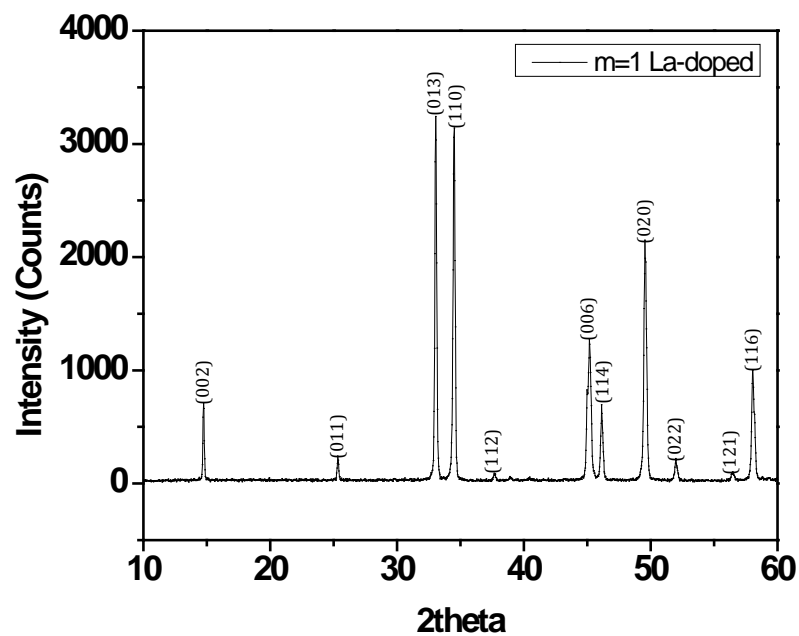


Figure 15: An X-ray diffraction (XRD) pattern acquired from the La-doped compound of the m=1 periodicity, fitting the tetragonal-crystal structure having the I4/mmm-symmetry (JCPDS number 040067894).

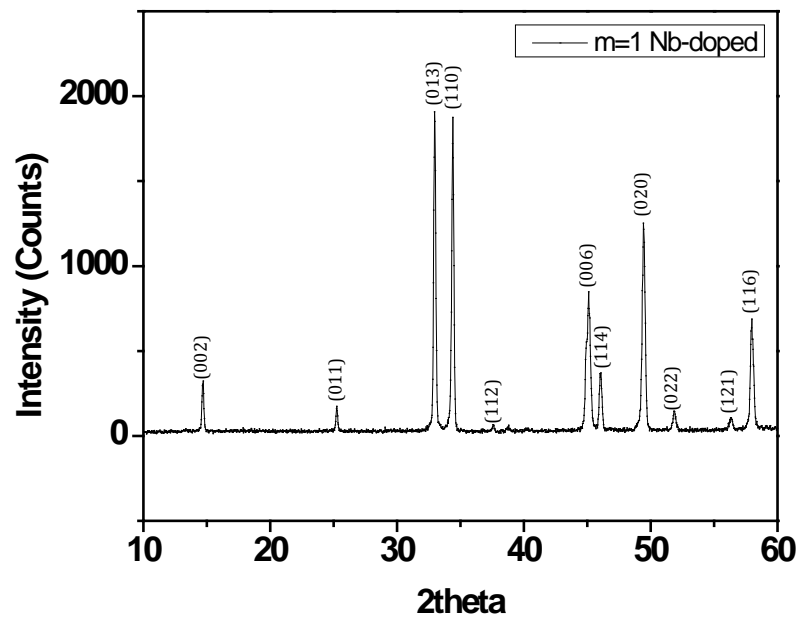


Figure 16: An X-ray diffraction (XRD) pattern acquired from the Nb-doped compound of the m=1 periodicity, fitting the tetragonal-crystal structure having the I4/mmm-symmetry (JCPDS number 040067894).

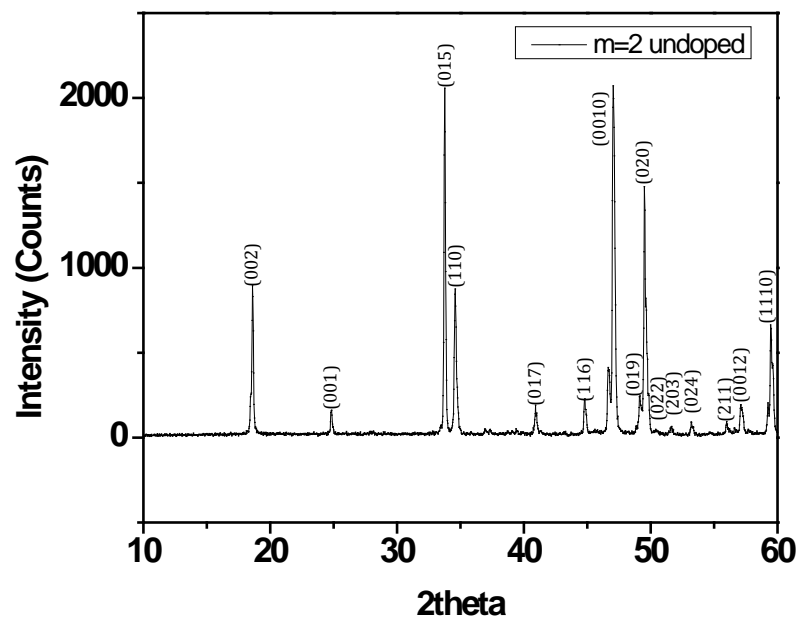


Figure 17: An X-ray diffraction (XRD) pattern acquired from the undoped compound of the m=2 periodicity, fitting the tetragonal-crystal structure having the I4/mmm-symmetry (JCPDS number: 040165273).

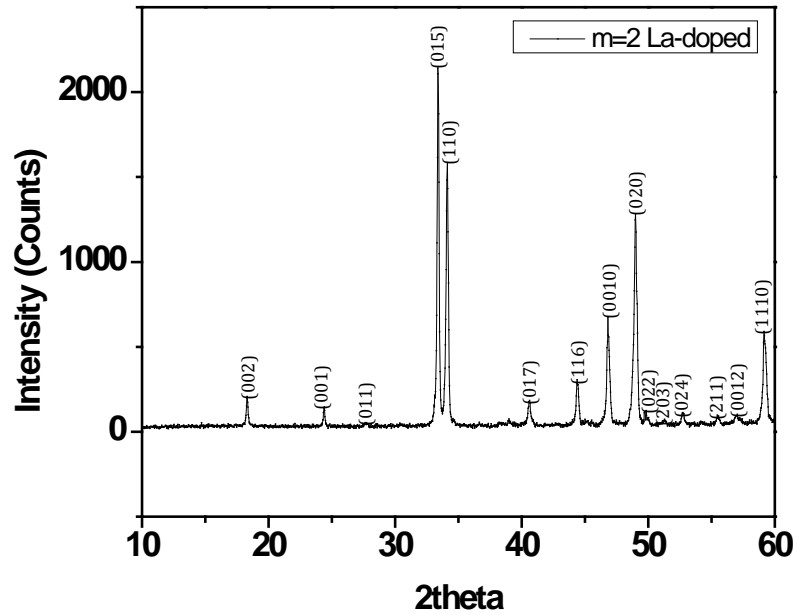


Figure 18: An X-ray diffraction (XRD) pattern acquired from the La-doped compound of the m=2 periodicity, fitting the tetragonal-crystal structure having the I4/mmm-symmetry (JCPDS number: 040165273).

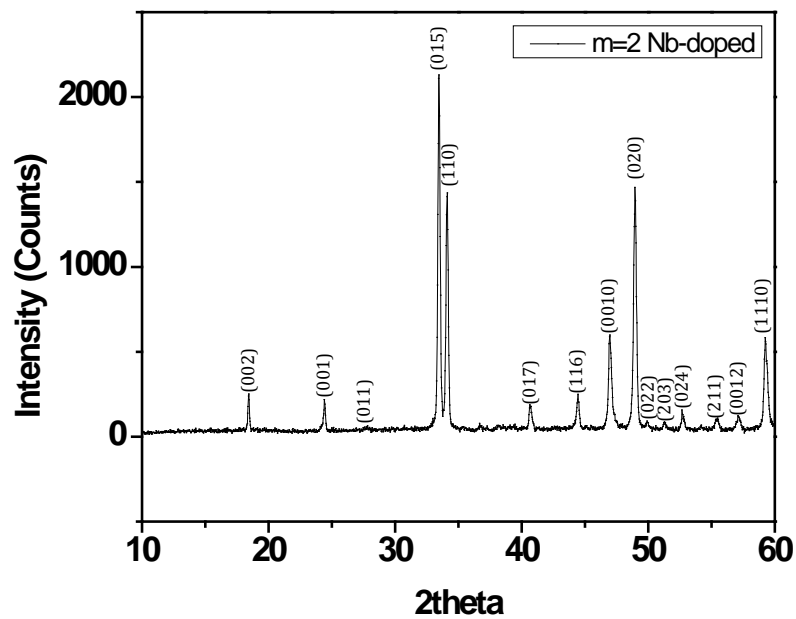


Figure 19: An X-ray diffraction (XRD) pattern acquired from the Nb-doped compound of the m=2 periodicity, fitting the tetragonal-crystal structure having the I4/mmm-symmetry (JCPDS number: 040165273).

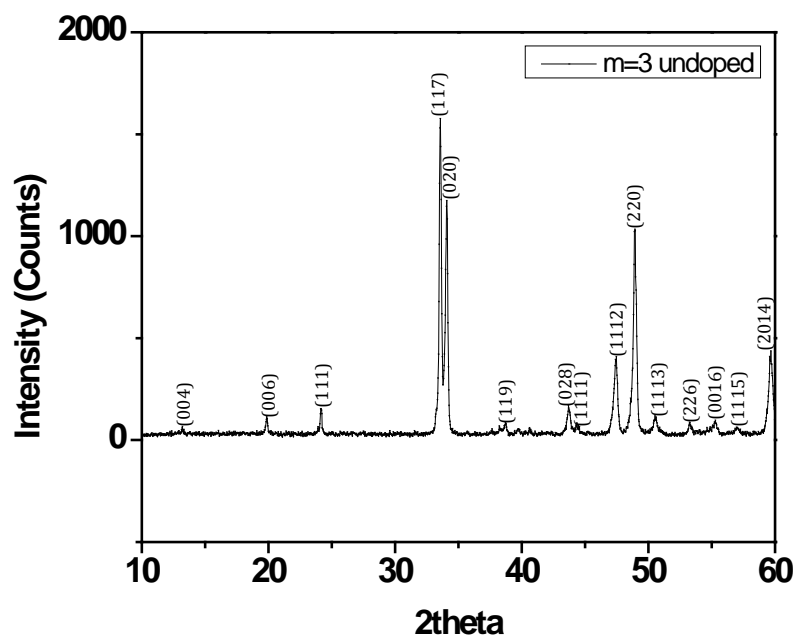


Figure 20: An X-ray diffraction (XRD) pattern acquired from the undoped compound of the m=3 periodicity, fitting the tetragonal-crystal structure having the I4/mmm-symmetry (JCPDS number: 000180298)

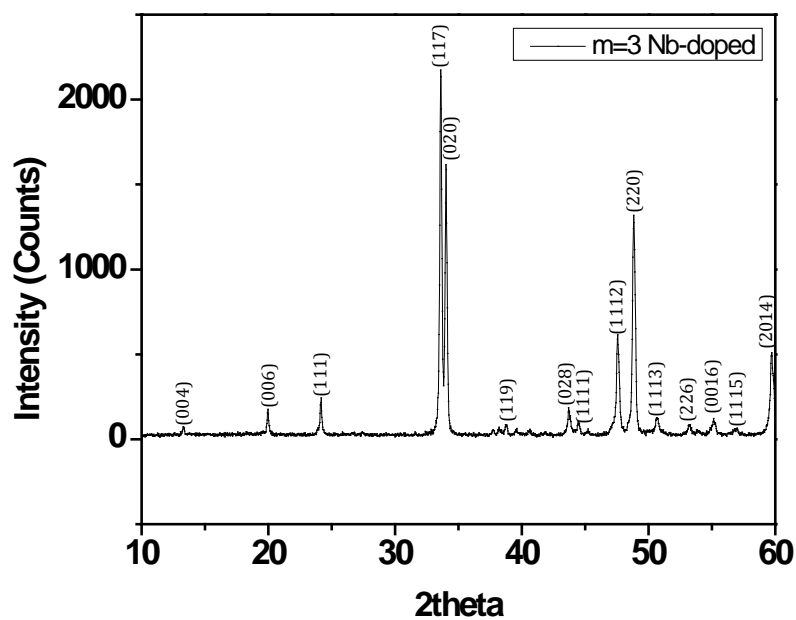


Figure 21: An X-ray diffraction (XRD) pattern acquired from the Nb-doped compound of the m=3 periodicity, fitting the tetragonal-crystal structure having the I4/mmm-symmetry (JCPDS number: 000180298)

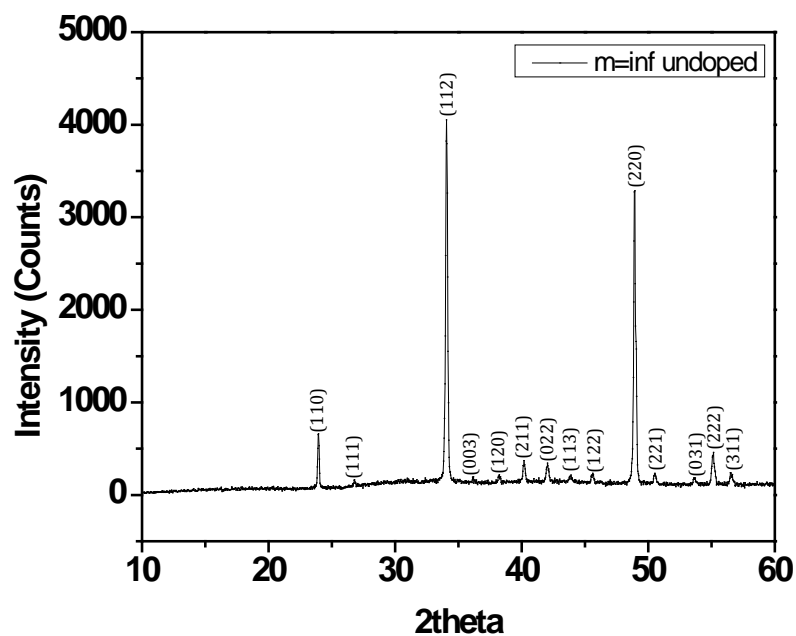


Figure 22: An X-ray diffraction (XRD) pattern acquired from the undoped compound of the $m=\infty$ periodicity, fitting the orthorhombic-crystal structure having the Pnma -symmetry (JCPDS number 040078030)

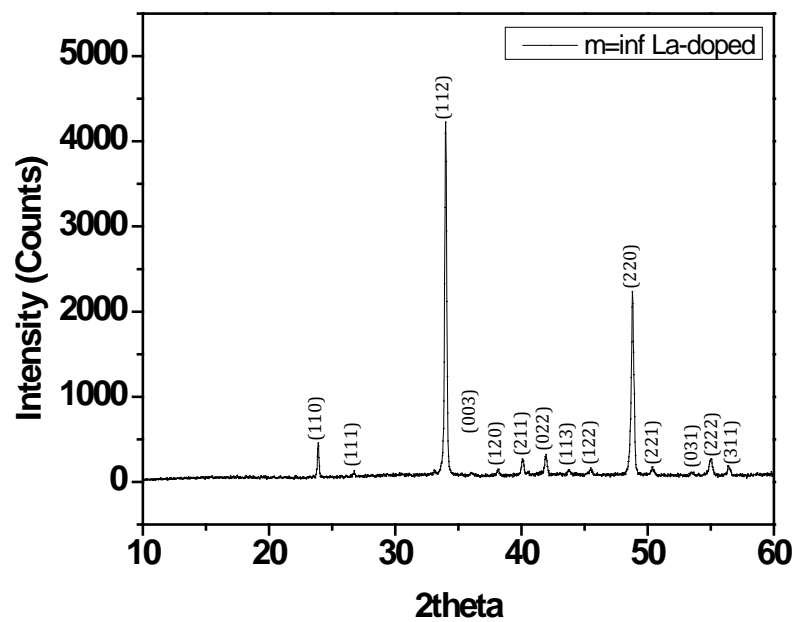


Figure 23: An X-ray diffraction (XRD) pattern acquired from the La-doped compound of the $m=\infty$ periodicity, fitting the orthorhombic-crystal structure having the Pnma-symmetry (JCPDS number 040078030)

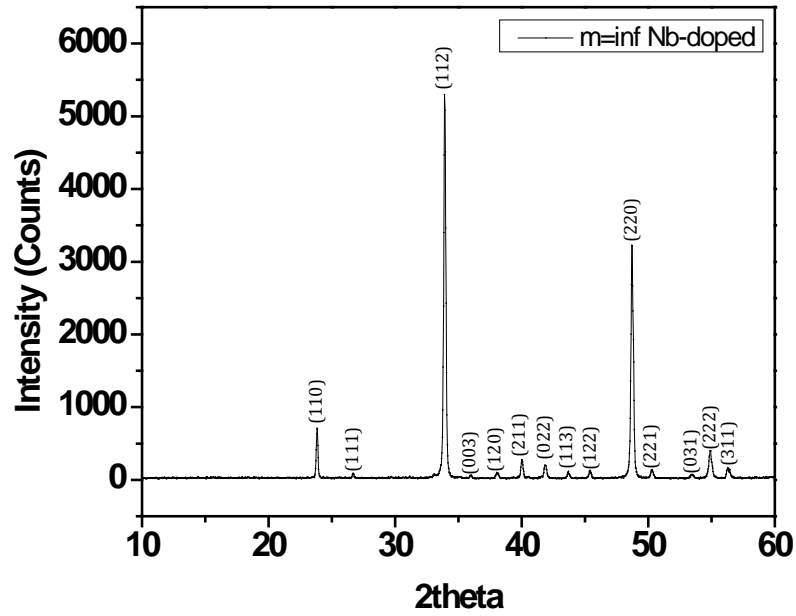


Figure 24: An X-ray diffraction (XRD) pattern acquired from the Nb-doped compound of the $m=\text{inf}$ periodicity, fitting the orthorhombic-crystal structure having the $Pnma$ -symmetry (JCPDS number 040078030)

In contrast to the above-listed results, the XRD pattern collected from the La-doped compound of the nominal $m=3$ periodicity, Fig. 25, does not fit the expected $I4/mmm$ space group symmetry represented by the JCPDS number 000180298, but to a combination of $m=\text{inf}$ and $m=2$. This composition will be, therefore, denoted by us as $m=3^*$ La-doped further on.

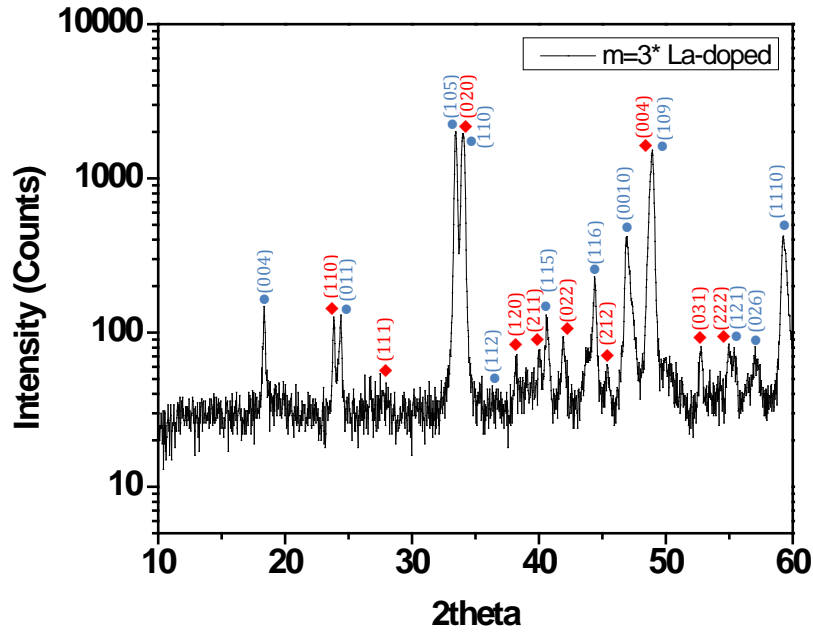


Figure 25: An X-ray diffraction (XRD) pattern acquired from the La-doped compound of the $m=3^*$ periodicity, fitting to the combination of $m=\text{inf}$ (blue dots) and $m=2$ (red diamonds).

Similarly, the XRD patterns collected from the Nb-doped compounds of the nominal periodicities of $m=4$ and 5 , Figs. 26 and 27, respectively, show correspondence to the combination of $m=\text{inf}$ and $m=3$, and will, therefore, be denoted as $m=4^*$ and $m=5^*$ further on.

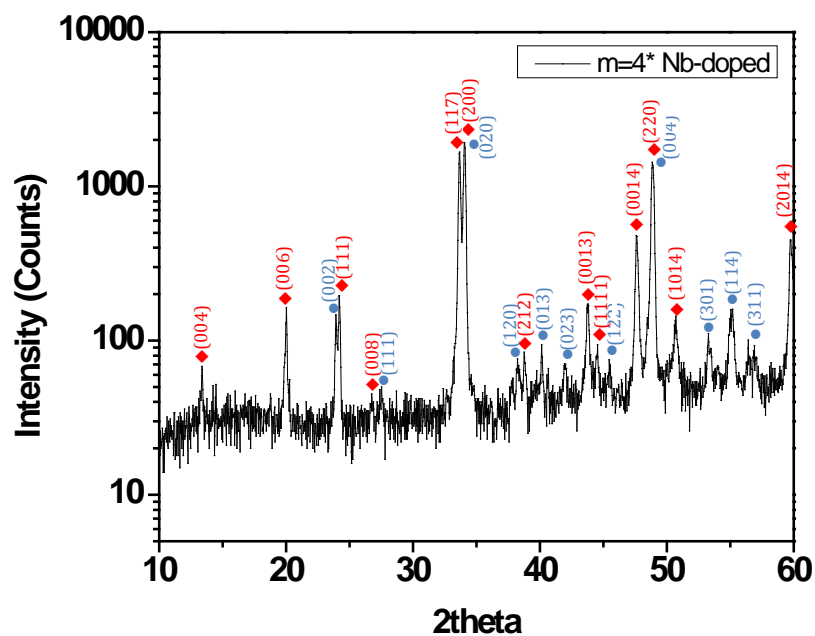


Figure 26: An X-ray diffraction (XRD) pattern acquired from the Nb-doped compound of the $m=4^*$ periodicity, fitting to the combination of $m=\infty$ periodicity (blue dots) and $m=3$ periodicity (red diamonds).

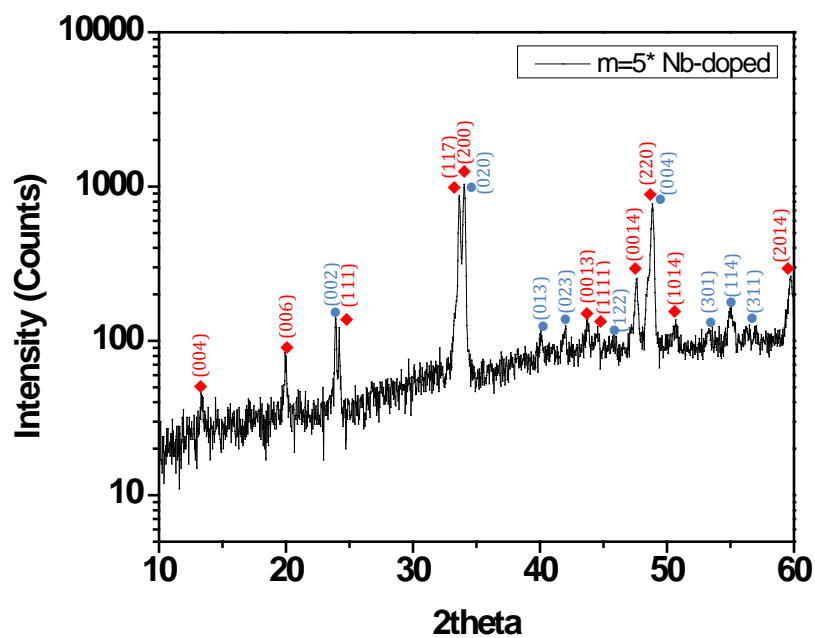


Figure 27: An X-ray diffraction (XRD) pattern acquired from the Nb-doped compound of the $m=5^*$ periodicity, fitting to the combination of $m=\infty$ periodicity (blue dots) and $m=3$ periodicity (red diamonds).

4.1.2 High-resolution scanning electron microscopy (HR-SEM) analysis

We performed HRSEM analysis for several purposes related to thermal conductivity analysis, given that the latter strongly correlates with a material's microstructure. First, we are interested in the grain size distribution, which will be taken into account in the analysis of thermal conductivity, Chapter 5. Second, we are interested in a rough estimate of the average pore size and porosity level; and, third, detection of the presence of sub-micrometer size second-phase precipitates, which are undetectable in XRD analysis, would be beneficial for understanding the thermal conductivity behavior. All micrographs were taken for the as-sintered specimens that did not undergo any surface treatment. Fig. 28, (a) through (l) displays HRSEM micrographs of the undoped, La-doped, and Nb-doped specimens of the $m=\infty$, 1, 2, and 3 periodicities.

The grain boundaries of all specimens are clearly visible due to thermal etching of the external surfaces taking place during the sintering process. It is also shown that the different compounds exhibit either equiaxed or elongated grain morphologies. Most importantly, the observable grain size ranges from a minimum value of $\sim 1 \mu\text{m}$ up to ca. $20 \mu\text{m}$ dia. It is noteworthy that no second-phase precipitates are detected. Furthermore, the compounds incorporate a certain level of porosity, a few vol. percents, with pores that are separated from each other by an average distance of $50\text{-}10 \mu\text{m}$. These data will serve us in the analysis of the thermal conductivity, Chapter 5.

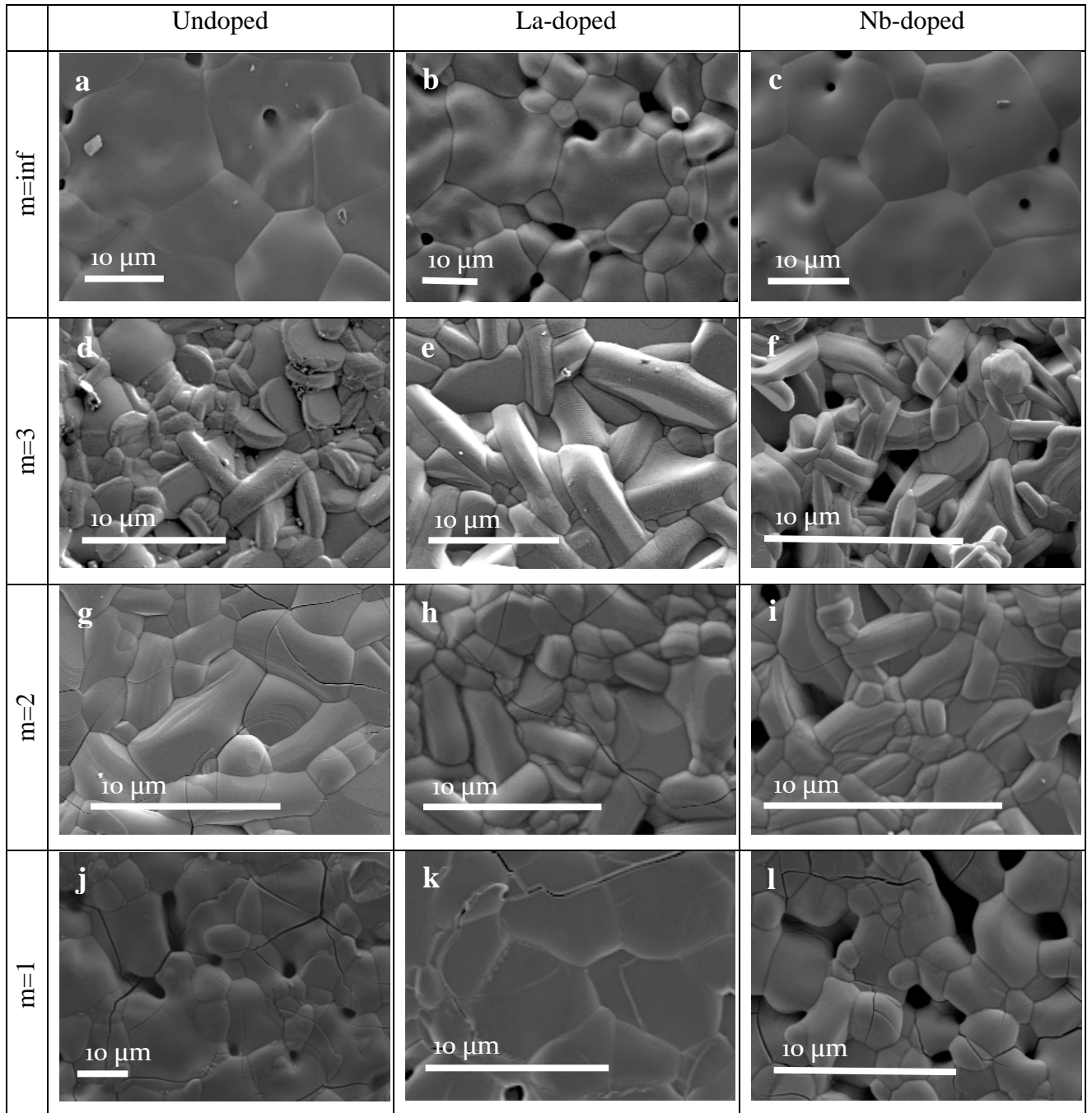


Figure 28: HRSEM micrographs of the different undoped and doped specimens having the $m=1,2,3$, and inf . periodicities.

Figure 29, (a) and (b) displays HRSEM micrographs taken from the Nb-doped specimens of the $m=4^*$ and 5^* periodicities.

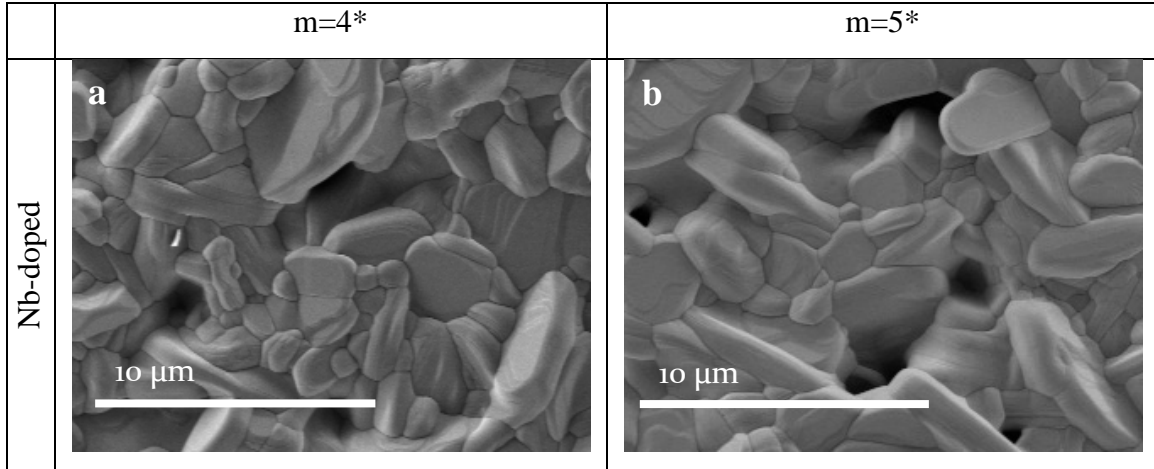


Figure 29: HRSEM micrographs taken from the Nb-doped specimens with $m=4^*$ and 5^* periodicities.

4.1.3 Grain size analysis

We are interested in grain size analysis for our compounds, since grain boundaries may play a significant role in scattering phonons, thereby reducing lattice thermal conductivity, depending on their density, i.e. grain size. Since many compounds exhibit elongated grain morphologies characterized by length and width (length > width), we consider the average *grain width* as the characteristic dimension that is significant for thermal conductivity. Table 3 summarizes the average grain widths measured for all compounds investigated in this study, based on the HRSEM micrographs. The average values were calculated from a population of about 500 grains per specimen. We note that the values listed in Table 3 represent the average grain sizes apparent on the specimens' surface, and may differ from the bulk grain size. We are, however, interested in an order of magnitude rather than in exact values.

Doping	m-value	Average grain width [μm]
Undoped	1	7.74 ± 0.65
La-doped	1	4.73 ± 0.55
Nb-doped	1	2.43 ± 0.71
Undoped	2	7.6 ± 0.55
La-doped	2	3.09 ± 0.44

Nb-doped	2	1.27 ± 0.78
Undoped	3	3.39 ± 0.53
La-doped	3*	2.74 ± 0.46
Nb-doped	3	1.23 ± 0.74
Nb-doped	4*	2.36 ± 0.72
Nb-doped	5*	2.22 ± 0.6
Undoped	inf	17.40 ± 0.45
La-doped	inf	8.52 ± 0.47
Nb-doped	inf	17.59 ± 0.63

Table 3: Average grain widths measured for the compounds investigated in this study.

Fig. 30 is a graphical representation of the materials average grain widths, classified by the doping nature: Undoped, La-doped, and Nb-doped compounds. It is observed that all grain widths range between ca. 2 and 20 μm , where doping reduces the average grain width, possibly owing to solute drag induced grain growth inhibition.

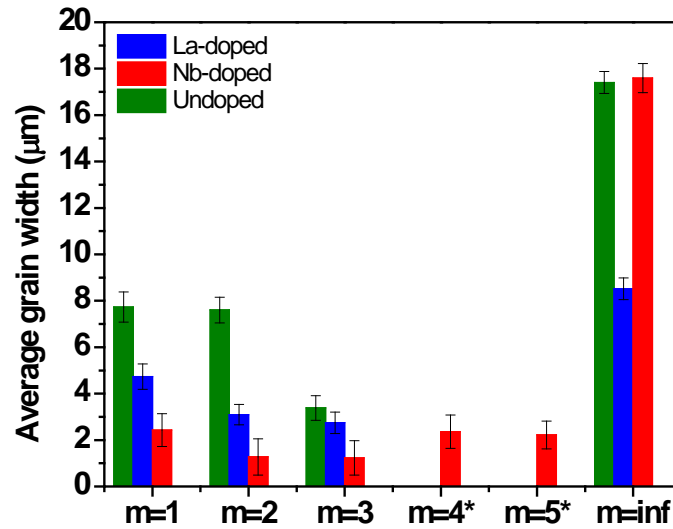


Figure 30: Average grain widths measured for all compounds of the different periodicities (m-values).

It is observed that all compounds exhibit log-normal-like distribution of grain widths. Fig. 31 shows an example of such distribution acquired from the undoped $m=\infty$ compound.

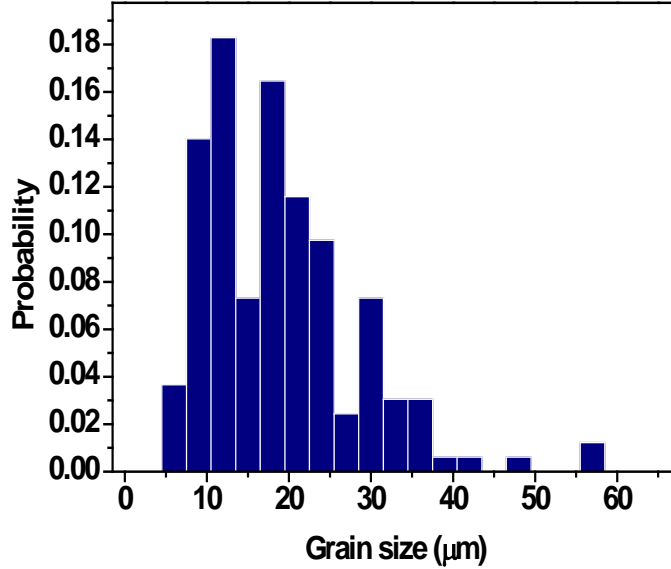


Figure 31: Grain Size distribution for the $m=\infty$ undoped sample.

4.2 Electrical measurements

We performed electrical measurements including electrical conductivity and Seebeck coefficient (thermopower) measurements. All electrical measurements are divided into two temperature ranges: measurements at 80 through 300 K were performed at the Physics Department, Technion, while those at 300 through 1000 K were done at the NETZSCH R&D laboratory, Germany.

4.2.1 Electrical conductivity measurements

We combined both electrical conductivity datasets in one temperature range from 80 to 1000 K. Figures 32 through 35 are graphical representations of the temperature-dependent electrical conductivities, classified according to the crystal periodicity (m -values).

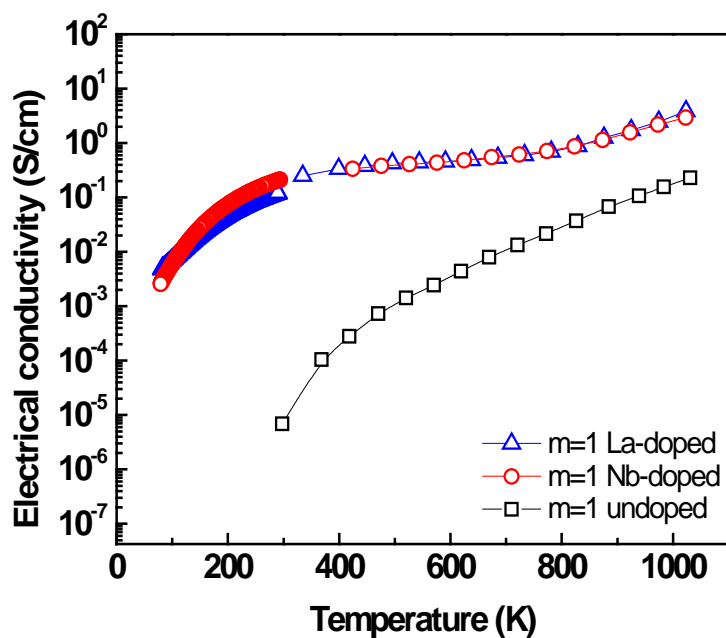


Figure 32: Graphical representation of the electrical conductivities plotted for the extended temperature range of 80 through 1000 K for the $m=1$ compounds: undoped (squares), La-doped (triangles), and Nb-doped (circles).

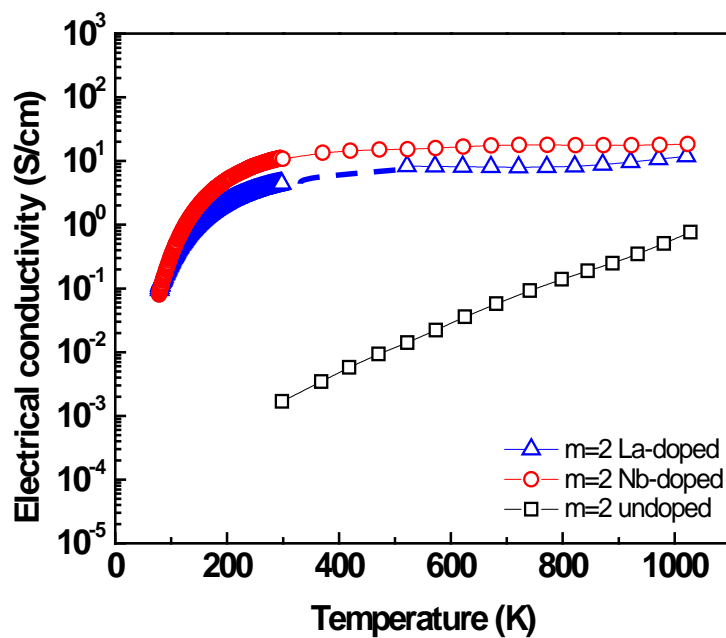


Figure 33: Graphical representation of the electrical conductivities plotted for the extended temperature range of 80 through 1000 K for the $m=2$ compounds: undoped (squares), La-doped (triangles), and Nb-doped (circles).

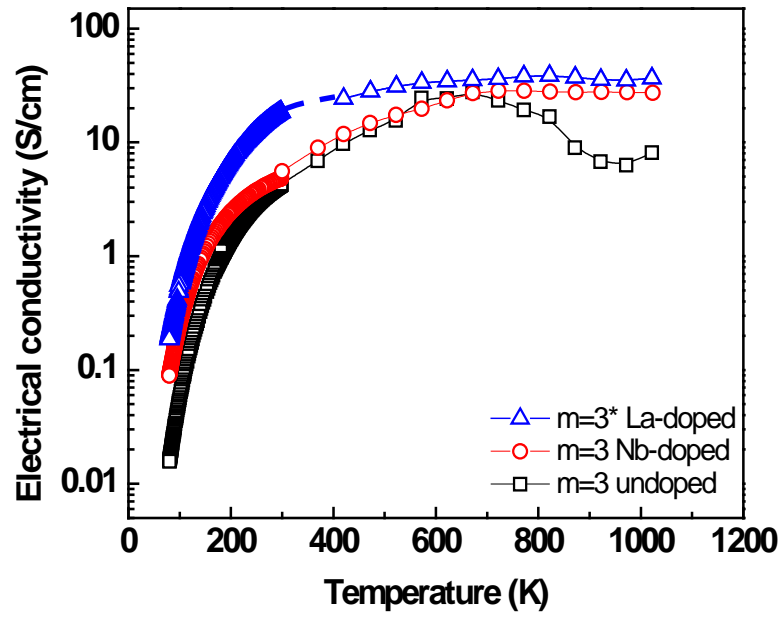


Figure 34: Graphical representation of the electrical conductivities plotted for the extended temperature range of 80 through 1000 K for the $m=3$ compounds: undoped (squares), La-doped (triangles), and Nb-doped (circles).

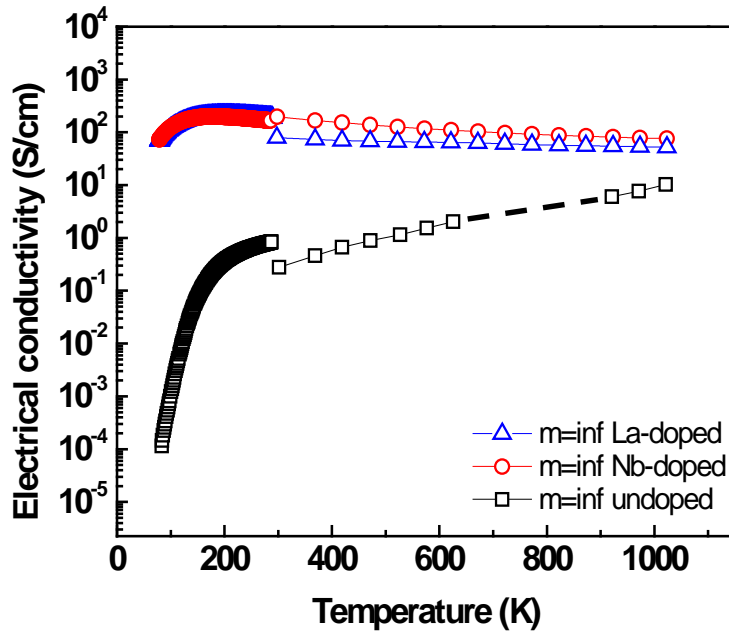


Figure 35: Graphical representation of the electrical conductivities plotted for the extended temperature range of 80 through 1000 K for the $m=\text{inf}$ compounds: undoped (squares), La-doped (triangles), and Nb-doped (circles).

The datasets presented in Figs. 32 through 35, when examined for each periodicity (m -value) individually, indicate a significant increase in electrical conductivity due to either La- or Nb-doping; for instance, by ~ 2 -4 orders of magnitude at room temperature. Interestingly, the effects of both La and Nb dopants are very similar. Particularly, it can be observed that for the $m=1$ compounds the effects of La- and Nb- are practically identical, whereas for the $m=2$ compounds the Nb-doped one exhibits electrical conductivity that is slightly higher than that of the La-doped one. Conversely, for the $m=3$ compounds, the La-doped sample exhibits the highest electrical conductivity values, and for the $m=\text{inf}$ compounds both of the doped samples exhibit identical electrical conductivity values up to 300 K. For higher temperatures, the electrical conductivity of the Nb-doped sample is slightly higher than that of the La-doped one.

Owing to the enhanced electrical conductivity measured for the doped compounds, we will focus on them further on. Since we are interested in the effects of lattice periodicity (m -value) on electrical conductivity, we plot the temperature-dependent conductivity for the different m -values, for the La-doped compounds (Fig. 36), and for the Nb-doped ones (Fig. 37).

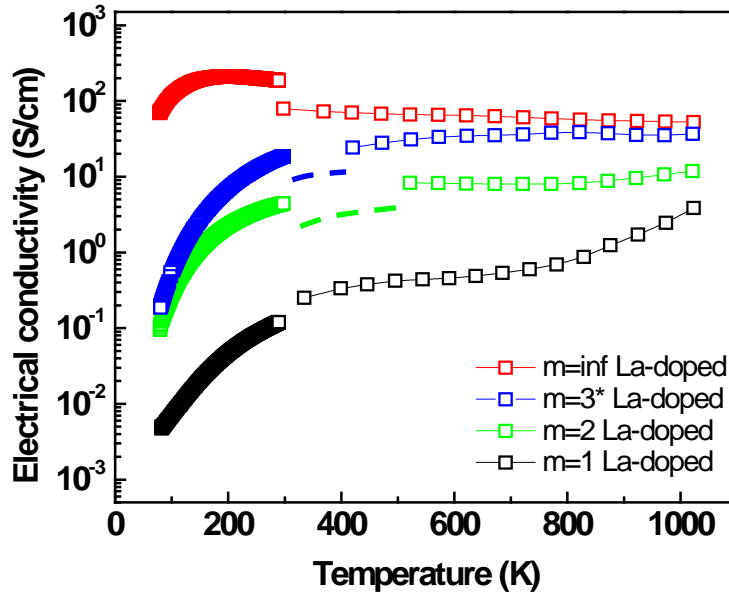


Figure 36: Electrical conductivity Vs. temperature for the La-doped samples having the periodicities of $m=\text{inf}$ (red markers), $m=1$ (black), $m=2$ (green), and $m=3^*$ (blue).

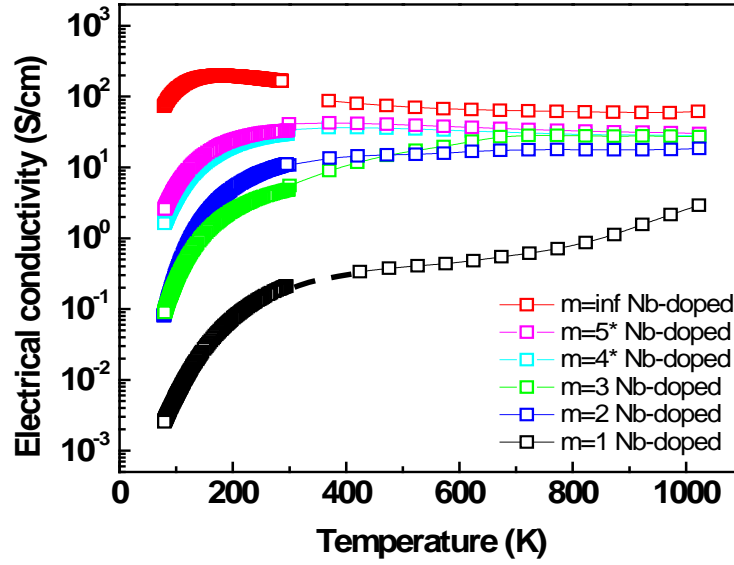


Figure 37: Electrical conductivity Vs. temperature for the Nb-doped samples having the periodicities of $m=\text{inf}$ (red markers), $m=1$ (black), $m=2$ (green), and $m=3$ (blue).

It is shown that the electrical conductivity values of all La-doped RP-phases ($m=1-3$) are lower than those of the $m=\text{inf}$ ones. This is attributed to the planar density of the insulating rock-salt (RS) CaO-layers in the polycrystalline RP samples. Moreover, it can be seen that the electrical conductivity values decrease systematically with increasing CaO planar density (decrease in m). Additionally, it is evident that the differences between electrical conductivity values of the RP phases decrease with increasing temperature.

4.2.2 Seebeck coefficient measurements

We measured the Seebeck coefficients for all compounds, and the results are graphically-represented in Figs. 38-41 for both doped and undoped specimens with the different periodicities (m -values). It can be seen that all samples exhibit negative S -values, implying on their n -type nature. As expected, the doped compounds possess lower $|S|$ -values than the undoped ones, due to increased charge carrier concentrations. At temperatures higher than 150-170 K, however, the $|S|$ -values increase with increasing

temperature unlike the undoped samples. Interestingly, both Nb- and La-doped samples exhibit similar thermopower, indicating that the dopant identity has almost no or little effect on thermopower, in contrast to its concentration.

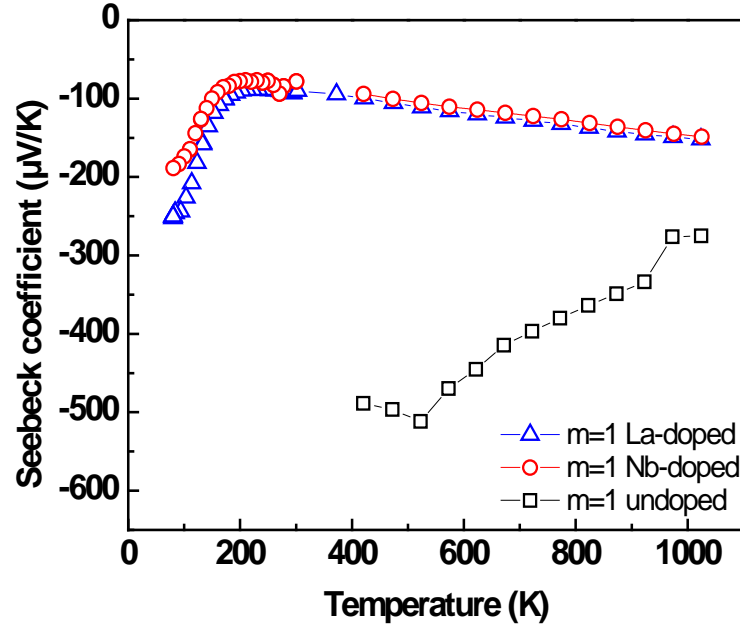


Figure 38: The temperature-dependent Seebeck coefficients measured for the compounds with the $m=1$ periodicity, plotted for the undoped (squares), La-doped (triangles), and Nb-doped (circles) states.

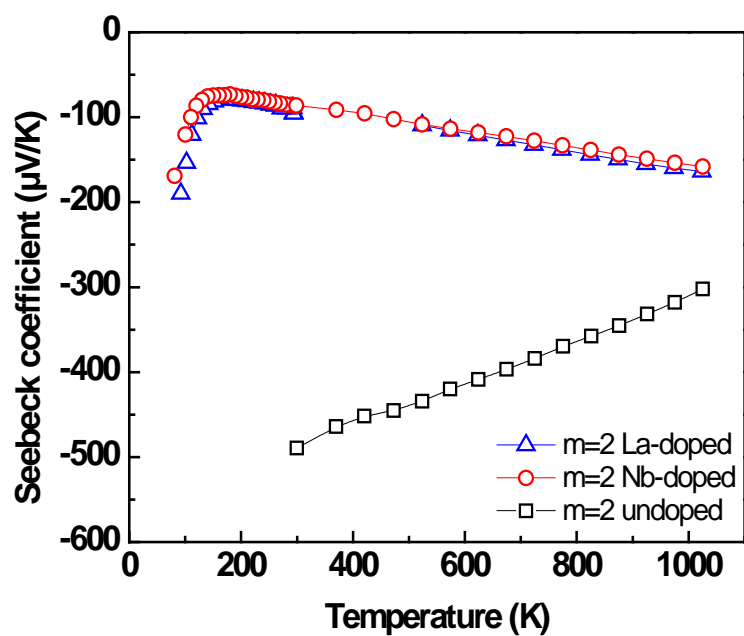


Figure 39: The temperature-dependent Seebeck coefficients measured for the compounds with $m=2$ periodicity plotted for the undoped (squares), La-doped (triangles), and Nb-doped (circles) states.

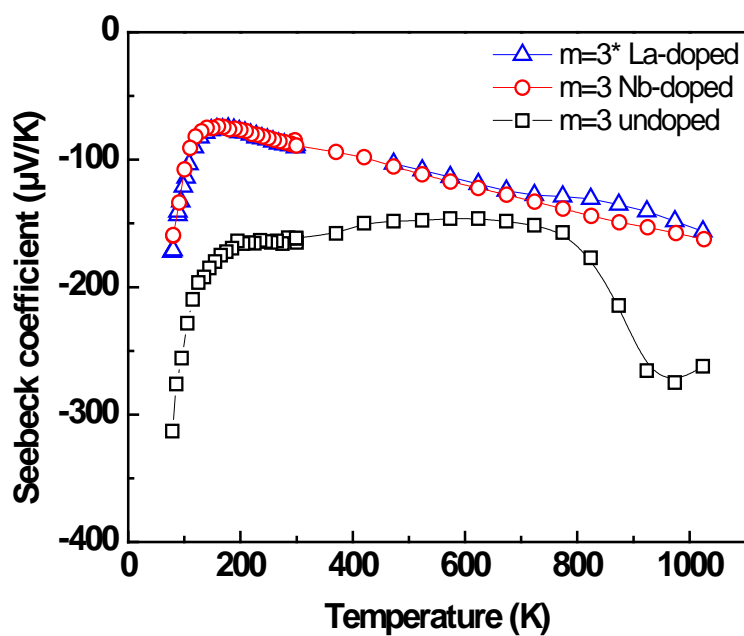


Figure 40: The temperature-dependent Seebeck coefficients measured for the compounds with $m=3$ periodicity plotted for the undoped (squares), La-doped (triangles), and Nb-doped (circles) states.

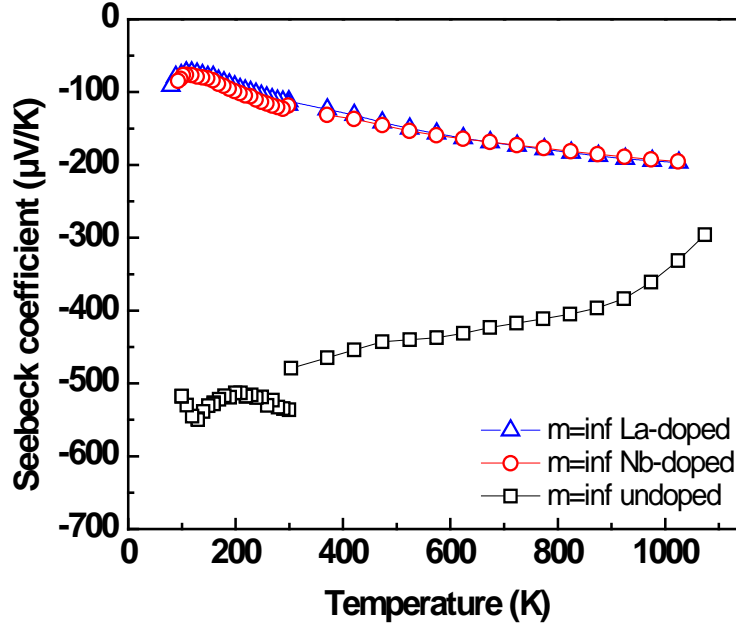


Figure 41: The temperature-dependent Seebeck coefficients measured for the compounds with $m=\text{inf}$ periodicity plotted for the undoped (squares), La-doped (triangles), and Nb-doped (circles) states.

Since we are interested in the effects on lattice periodicity (m -value) on electrical properties, we plot the temperature-dependent thermopower for the different m -values, for the La-doped compounds (Fig. 42), and for the Nb-doped ones (Fig. 43). It is shown that the $|S|$ -values of the RP phases ($m=1-3$) are lower than that of the $m=\text{inf}$. one. Additionally, all RP phases exhibit similar $|S|$ values for the temperature range studied. Moreover, it can be seen that all of the $|S(T)|$ plots attain their maxima around 150-170 K. Below the maximum the behavior is complicated,¹⁰ and is irrelevant for our purpose. At higher temperatures $|S(T)|$ increases with increasing temperature.

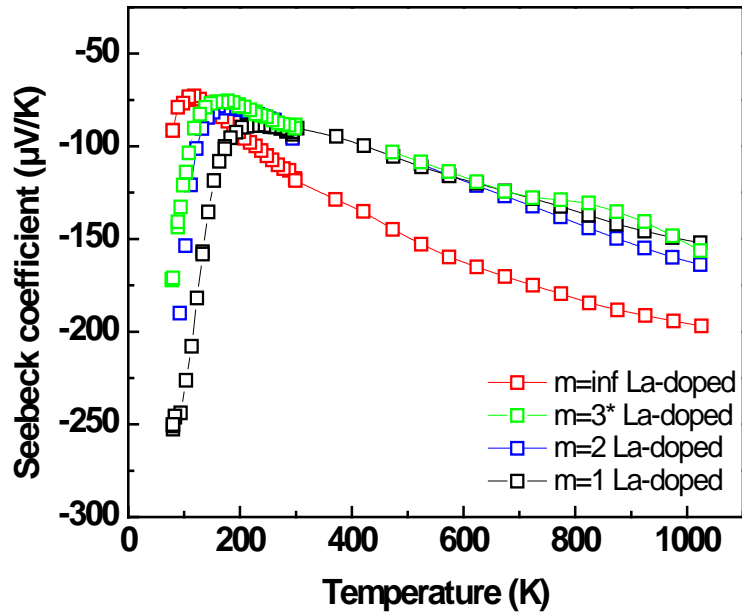


Figure 42: The temperature-dependent Seebeck coefficients measured for the La-doped compounds of different periodicities: $m=\text{inf}$ (red), $m=3^*$ (green), $m=2$ (blue) and $m=1$ (black).

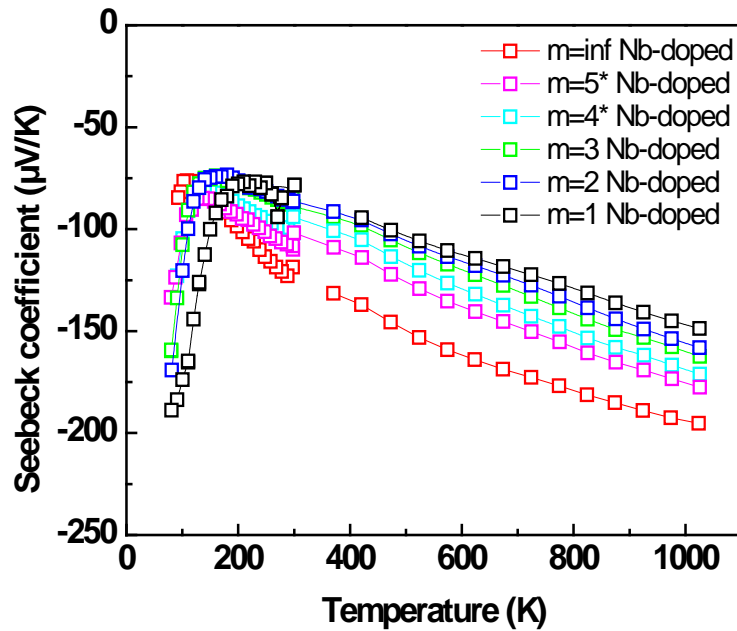


Figure 43: The temperature-dependent Seebeck coefficients measured for the Nb-doped compounds of different periodicities: $m=\text{inf}$ (red), $m=5^*$ (purple), $m=4^*$ (aqua), $m=3$ (green), $m=2$ (blue) and $m=1$ (black).

4.3 Thermal diffusivity measurments

We measured the thermal diffusivities of all samples in the temperatures range of 300 through 1000 K using LFA. Figures 44 through 47 are graphical representations of the temperature-dependent thermal diffusivities, classified according to the crystal periodicity (m-values). It is shown that the effects of both La and Nb dopants are different. The highest thermal diffusivity is obtained for Nb-doping, and can be observed for all periodicities, except for $m=3^*$, whereas no systematic trend can be observed for the La-doped and the undoped samples. Particularly, it can be seen that for the $m=1$ compounds La-doping does not affect thermal diffusivity, whereas for the $m=2$ compounds La-doping increases thermal diffusivity. Conversely, for the $m=3$ compounds, the La-doped sample exhibits the highest thermal diffusivity values and the undoped one possesses the lowest thermal diffusivity values.

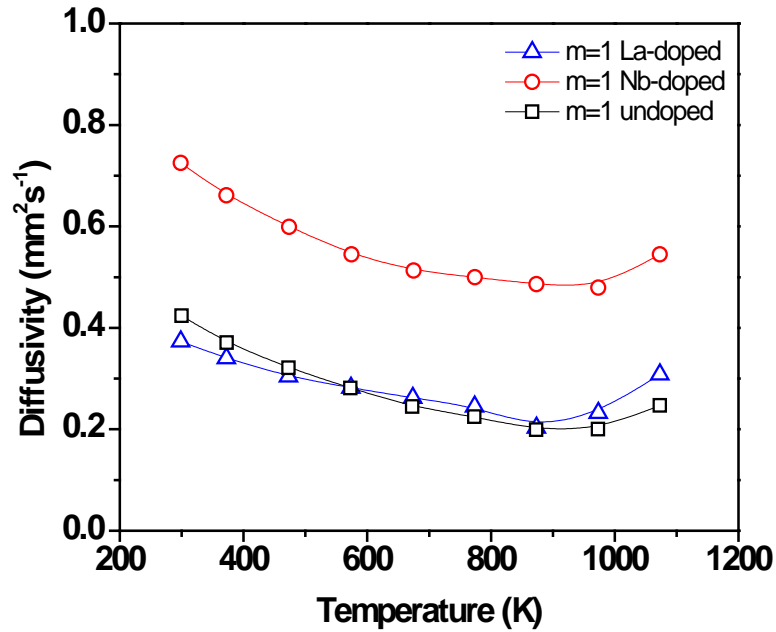


Figure 44: The temperature-dependent thermal diffusivities of the compounds having $m=1$ periodicity measured for the undoped (squares), La-doped (triangles), and Nb-doped (circles) ones.

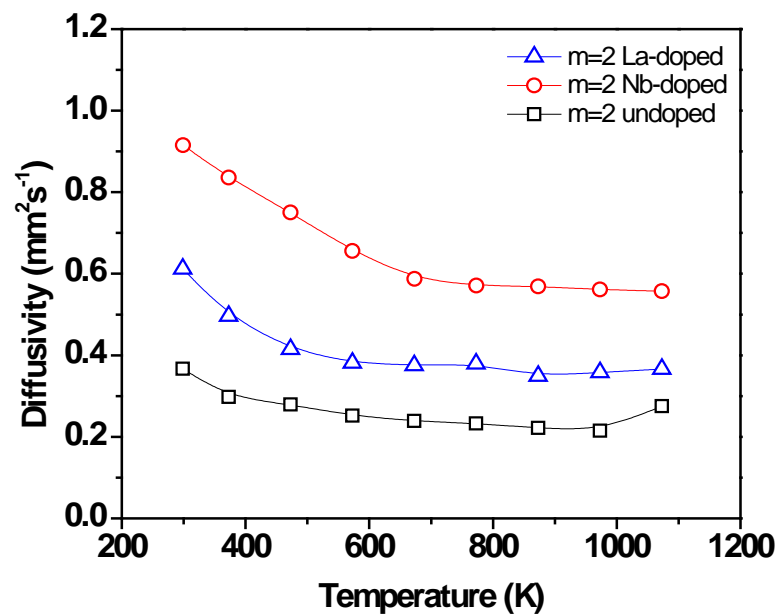


Figure 45: The temperature-dependent thermal diffusivities of the compounds having $m=2$ periodicity measured for the undoped (squares), La-doped (triangles), and Nb-doped (circles) ones.

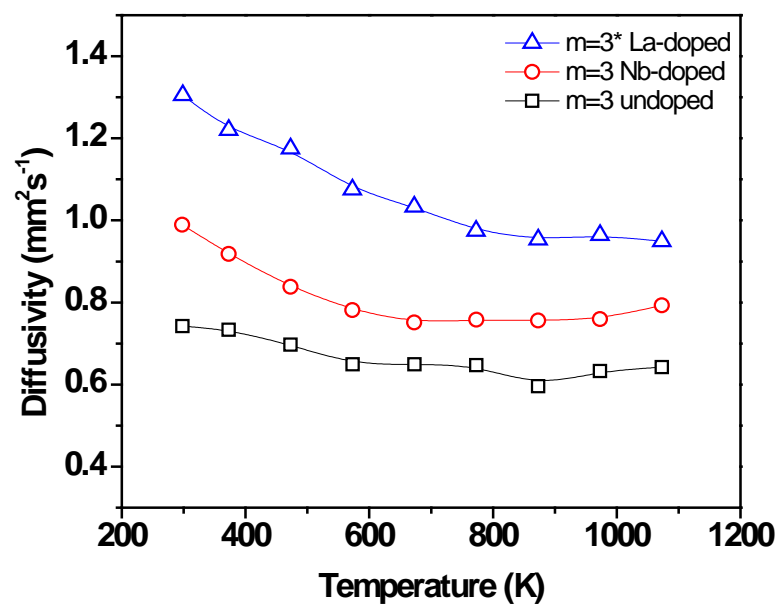


Figure 46: The temperature-dependent thermal diffusivities of the compounds having $m=3$ periodicity measured for the undoped (squares), La-doped (triangles), and Nb-doped (circles) ones.

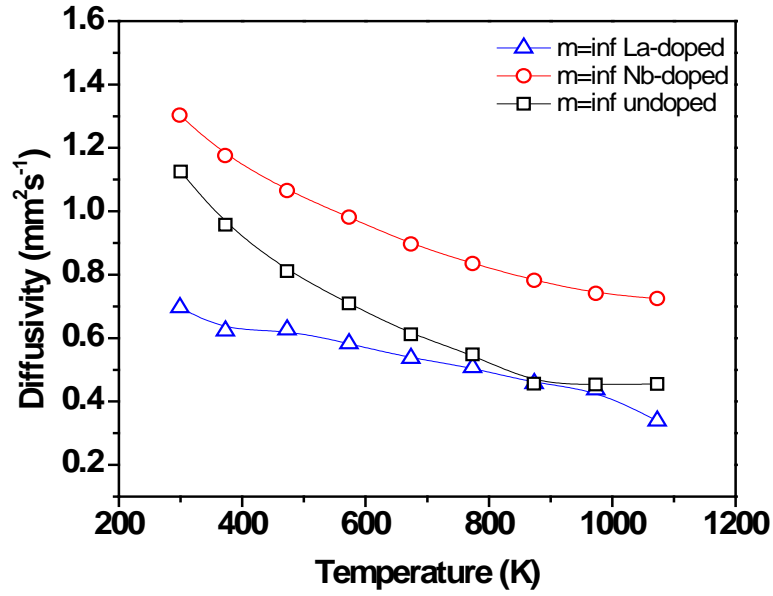


Figure 47: The temperature-dependent thermal diffusivities of the compounds having $m=i$ periodicity measured for the undoped (squares), La-doped (triangles), and Nb-doped (circles) ones.

Since we are interested in the effects of lattice periodicity (m -value) on thermal diffusivity, we plot the temperature-dependent diffusivity for the different m -values, for the La-doped compounds (Fig. 48), and for the Nb-doped ones (Fig. 49). It is shown that the thermal diffusivity values of all La-doped and Nb-doped RP-phases are greater than those of the $m=1$ ones. This is attributed to the maximum planar density of the insulating RS CaO-layers attained for $m=1$. Additionally, it is evident that the differences between the thermal diffusivity values of the RP phases prevail for elevated temperatures, as well.

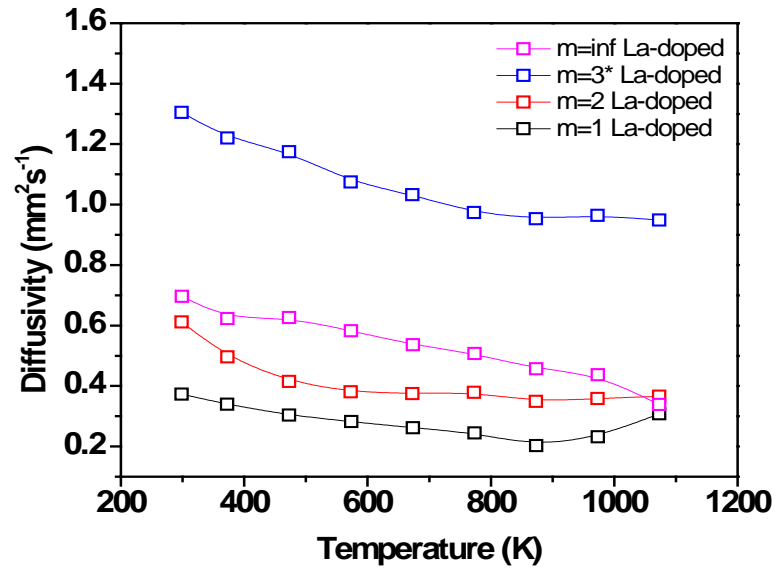


Figure 48: The temperature-dependent thermal diffusivity measured for the La-doped compounds of different periodicities: $m=\text{inf}$ (magenta), $m=1$ (black), $m=2$ (red), and $m=3^*$ (blue).

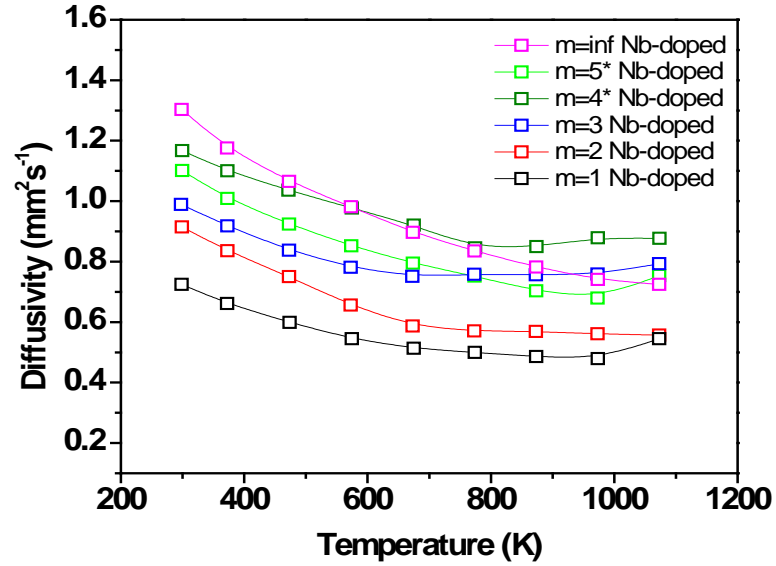


Figure 49: The temperature-dependent thermal conductivity measured for the Nb-doped compounds of different periodicities: $m=\text{inf}$ (magenta), $m=1$ (black), $m=2$ (red), $m=3$ (blue), $m=4^*$ (dark green), and $m=5^*$ (light green).

4.4 Thermal conductivity measurements

We calculated the thermal conductivities of the compounds based on Eq. (22), as a product of the thermal diffusivity, heat capacity, and density. Whereas the materials densities were measured at room temperature and considered to be constant, the thermal diffusivities and heat capacities were determined using LFA for a wide temperature range of 300 through 1000 K. The measured bulk densities appear in Table 4. The heat capacities of some representative samples with different m-values and different dopant types are presented in Fig. 50. It can be seen that the specific heat is similar for several m-values with different doping types, and follow the Dulong-Petit behavior.¹¹ Since thermal diffusivity is measured directly by the LFA, whereas heat capacity is indirectly measured, we interpolate an average $C_p(T)$ -function, Fig. 51, that is representative for all specimens to facilitate the calculation of the $\kappa(T)$ -function.

m-value	Bulk density [g/cm ³]		
	Undoped	La-doped	Nb-doped
m=1	3.29±0.03	3.18±0.03	2.30±0.02
m=2	3.27±0.03	3.20±0.03	3.11±0.03
m=3	3.66±0.04	3.55±0.04	2.22±0.02
m=4	2.95±0.03	————	————
m=5	3.37±0.03	————	————
m=inf	3.70±0.04	3.77±0.04	3.52±0.04

Table 4: The bulk densities calculated for all samples produced.

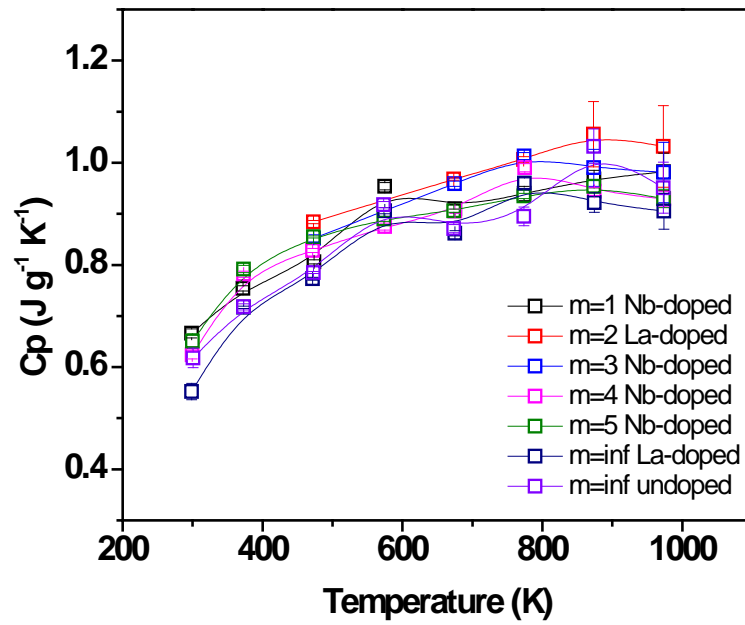


Figure 50: Specific heat vs. temperature as measured for several specimens employing laser flash analyzer (LFA).

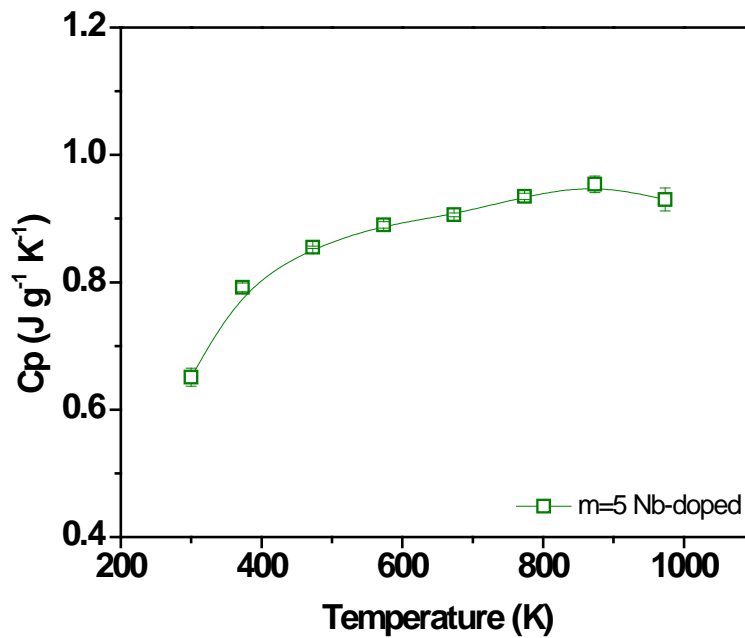


Figure 51: An interpolated function for the heat capacity, representative for all specimens.

The thermal conductivities, as calculated applying the above procedure, are presented in Fig. 52 through 55. It can be seen that for the La-doped compounds, those having m -values other than 3 exhibit lower thermal conductivity values than the Nb-doped ones. The La-doped sample having $m=3^*$ periodicity exhibits the highest thermal conductivity. However, as mentioned in Section 4.1.1, the La-doped $m=3^*$ compound contains a mixture of phases.

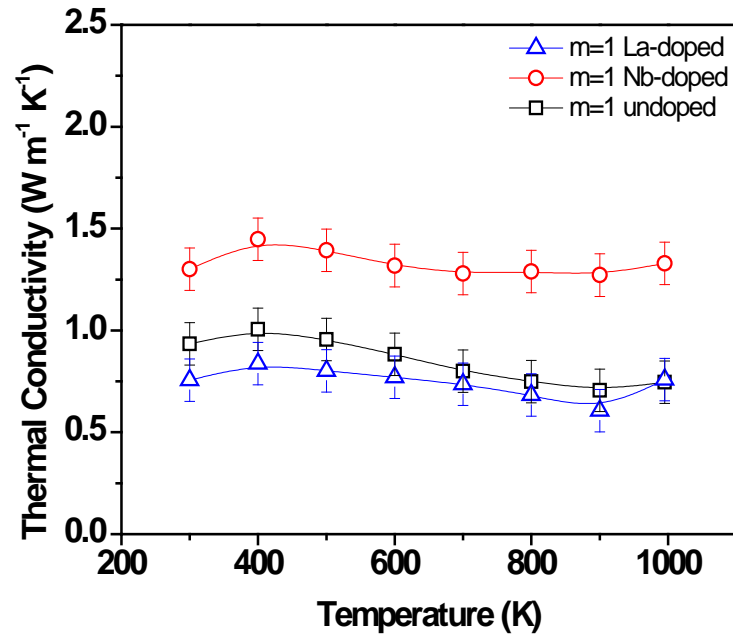


Figure 52: The temperature-dependent thermal conductivities of the compounds having $m=1$ periodicity measured for the undoped (squares), La-doped (triangles), and Nb-doped (circles) ones.

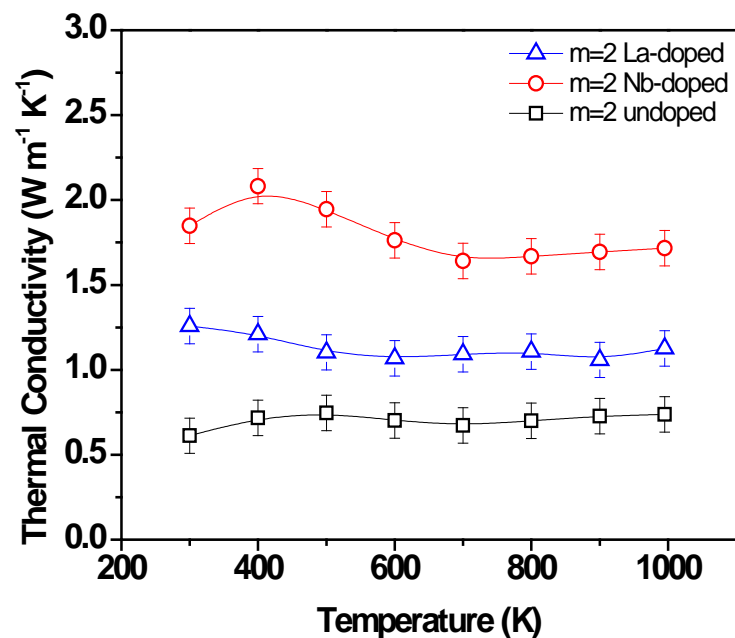


Figure 53: The temperature-dependent thermal conductivities of the compounds having $m=2$ periodicity measured for the undoped (squares), La-doped (triangles), and Nb-doped (circles) ones.

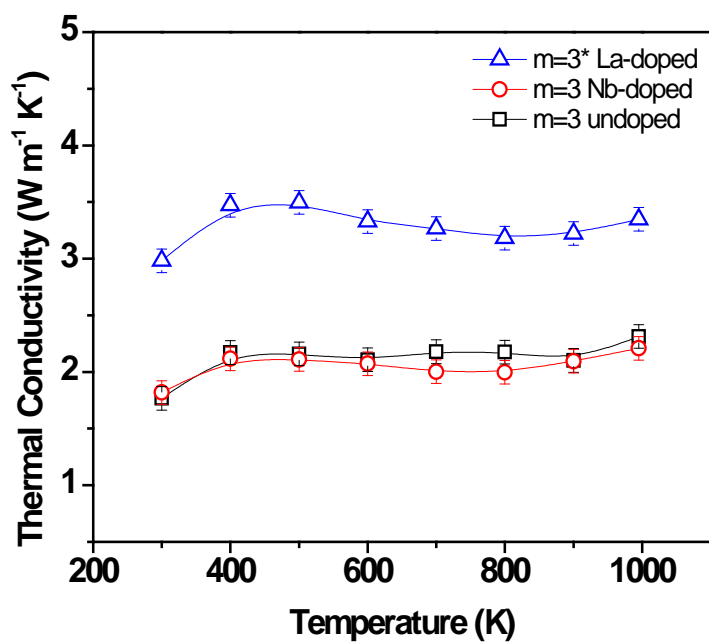


Figure 54: The temperature-dependent thermal conductivities of the compounds having $m=3$ periodicity measured for the undoped (squares), La-doped (triangles), and Nb-doped (circles) ones.

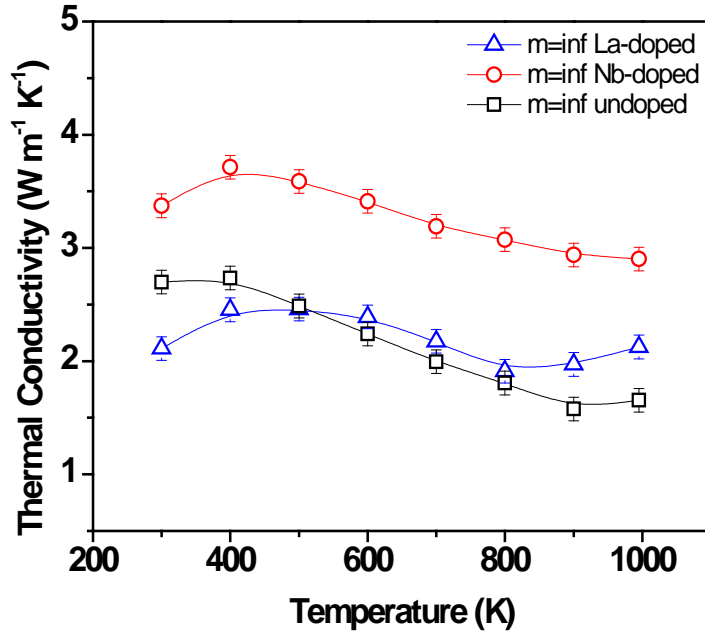


Figure 55: The temperature-dependent thermal conductivities of the compounds having $m=\text{inf}$ periodicity measured for the undoped (squares), La-doped (triangles), and Nb-doped (circles) ones.

Since we are interested in the effects of lattice periodicity (m -value) on thermal conductivity, we plot the temperature-dependent thermal conductivities for the different m -values, for the La-doped compounds (Fig. 56), and for the Nb-doped ones (Fig. 57). A remarkable reduction in thermal conductivity due to the introduction of CaO-planes is observed. Most importantly, the thermal conductivity decreases systematically with increasing RS planes density (decreasing m -value). Additionally, the differences in thermal conductivity of the RP phases do not significantly change with temperature, unlike the electrical conductivity values, as seen in section 4.2.1. This is a remarkable feature, and is important for the design of high-temperature TE materials, and will be discussed in Chapter 5.

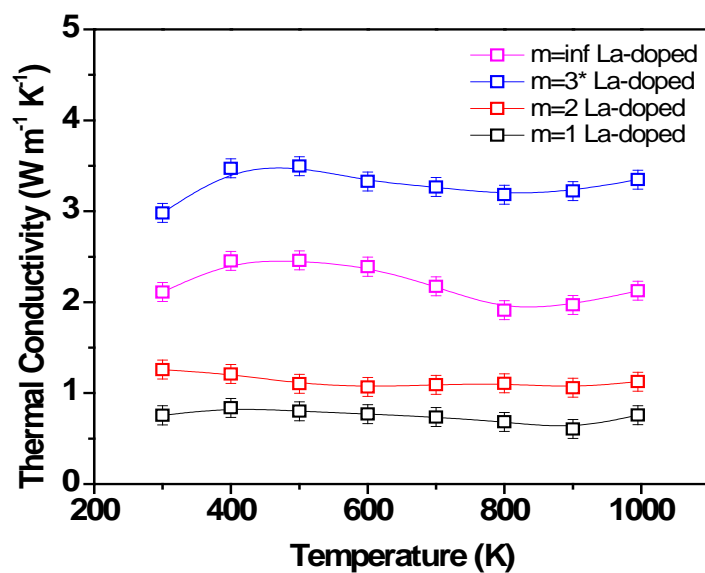


Figure 56: The temperature-dependent thermal conductivity measured for the La-doped compounds of different periodicities: $m=\text{inf}$ (magenta), $m=1$ (black), $m=2$ (red), and $m=3^*$ (blue).

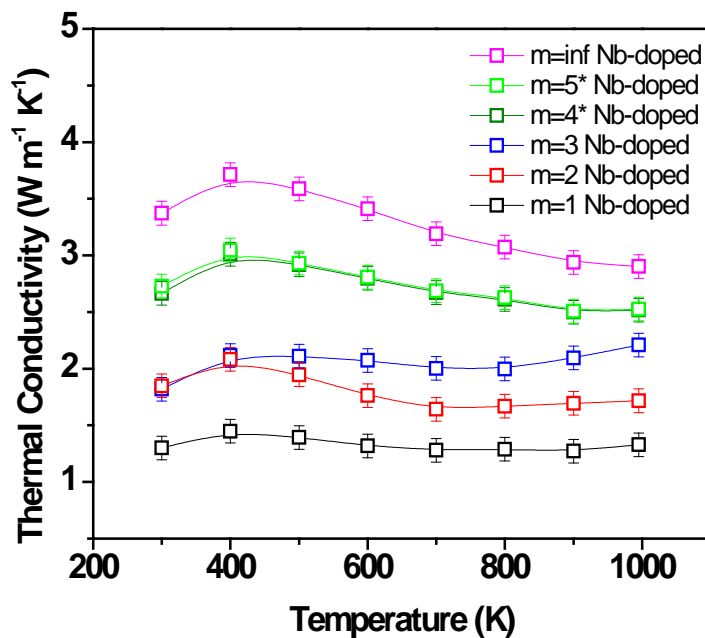


Figure 57: The temperature-dependent thermal conductivity measured for the Nb-doped compounds of different periodicities: $m=\text{inf}$ (magenta), $m=1$ (black), $m=2$ (red), $m=3$ (blue), $m=4^*$ (dark green), and $m=5^*$ (light green).

5. Discussion

In this chapter we discuss the results acquired in this study, in view of the research goals. This chapter consists of four sections. The first one, Section 5.1, introduces our analysis of thermal conductivity, and focuses on qualitative and quantitative explanation of the effects of the extra RS-planes on thermal conductivity employing the Callaway model. The second one, Section 5.2, refers to the electrical conductivity results. The third one, Section 5.3, includes calculations and discussion of the power factors. The last Section, 5.4, discusses the dimensionless figure of merit, ZT, which was calculated for the materials produced in this study.

5.1 Thermal conductivity analysis

5.1.1 The effects of CaO planes

It is clear from our XRD analysis, Section 4.1 that RP-phases with certain m -values exist in our undoped specimens, as well as in the La-doped $m=1$ and 2 , and Nb-doped $m=1$, 2 , and 3 materials. The rest, i.e. La-doped $m=3^*$ and Nb-doped $m=4^*$ and 5^* , exhibit a mixture of RP phases with no single and definite m -value. Furthermore, the systematic reduction in thermal conductivity due to increasing CaO-planes density (decreasing m -values), is evident from Section 4.3. We, therefore, attempt to account for this behavior on a quantitative basis.

To this end, we apply the Callaway model introduced in Section 2.3.2 and represented by Eq. (10), considering the conditions prevailing in the current experimental system. First, as the temperatures in which we measured thermal conductivity range from room temperature up to 1000 K, we assume that U-processes are the dominant phonon-phonon scattering mechanism, which is a conventional approximation.^{10,26} We will, therefore, utilize expression (12) for the phonon relaxation time in the U-process. Second, we identify two types of internal boundaries in our materials that may act as phonon scattering centers: grain boundaries and CaO-planes. To represent the phonon relaxation

times for boundary scattering, we utilize two variants of expression (13), as follows. For scattering from grain boundaries we express the relaxation time as:

$$(28.1) \quad \tau_{B1}^{-1} = \tau_{GBs}^{-1} \approx \frac{v_s}{L(\text{grain size})} \quad ,$$

where L (grain size) denotes an average value of grain width, following our definition in Section 4.1.3. For scattering from the RS (CaO) layers, we express the relaxation time as:

$$(28.2) \quad \tau_{B2}^{-1} = \tau_{RS(m=1,2,3,45,i)}^{-1} \approx \frac{v_s}{L(m)}$$

where L(m) denotes the equivalent distance between the two adjacent RS layers, which is essentially the perovskite unit cell c-parameter times m, Table 1. We note that in the current two-boundary model we neglect the possibility that the two boundaries might have different scattering efficiency, which is manifested by different values of transmission coefficient. The latter should be expressed in terms of the phonon polarizations and velocities, and is beyond the scope of this thesis.²¹ This approximation is, however, sufficient for our needs.

Other parameters that we need in order to employ the Callaway model are the sound velocities and the Debye temperatures of the different structures. As these values are unavailable and were not reported in literature, to the best of our knowledge, we calculated them from first-principles, following the procedure detailed in Section 3.4, for model compounds that are undoped and consist of $m = 1, 2, 3$, and inf. We did not perform these calculations for $m=4$ and 5 since their crystal structures are unknown. The results are shown in Table 5.

Material	v_s [m/s]	T_D [K]
m=1 undoped	5212	693.9
m=2 undoped	4975	670.3
m=3 undoped	3783	512.5
m=inf undoped	4226	632.4

Table 5: The sound velocities and Debye temperatures calculated for the undoped m=1, 2, 3, and inf. from first-principles.

Applying Matthiesen's rule, Eqs. (8) and (11), on our three phonon relaxation times, we calculated the temperature-dependent thermal conductivity values based on Eq. (10). Figure 52 is a graphical representation of the results, where U indicates U-processes scatterings, and GB and RS indicate scattering from grain boundaries and RS layers, respectively. We use an average grain width of 17.4 μm . To emphasize the dominance of scattering from grain boundaries as compared to that of U-processes, we calculate both scattering mechanisms for the m=inf specimens, which contain no RS layers. It can be seen that the calculated values of both m=inf states (U-only and U+GB) are very close to each other, and are significantly greater than those of the RS-containing structures. This fact is very consequential for this study, since it means that grain size of the order of magnitude $>$ several micrometers have negligible contribution for the total thermal conductivity, when compared to the RS-layers. Moreover, it can be stated that grain boundaries in any polycrystal having average grain size larger than several micrometers play no role in determining the lattice thermal conductivity. In such circumstances, lattice thermal conductivity is dominated by inelastic phonon scattering (U-processes). We, therefore, do not consider scattering from grain boundaries in the calculations made for the rest of the RP phases (m=1 through 3). Most importantly, Fig. 58 indicates a reduction in the thermal conductivity values of the RP phases, as compared to the m=inf ones, and that the m=1 configuration exhibits the lowest thermal conductivity values.

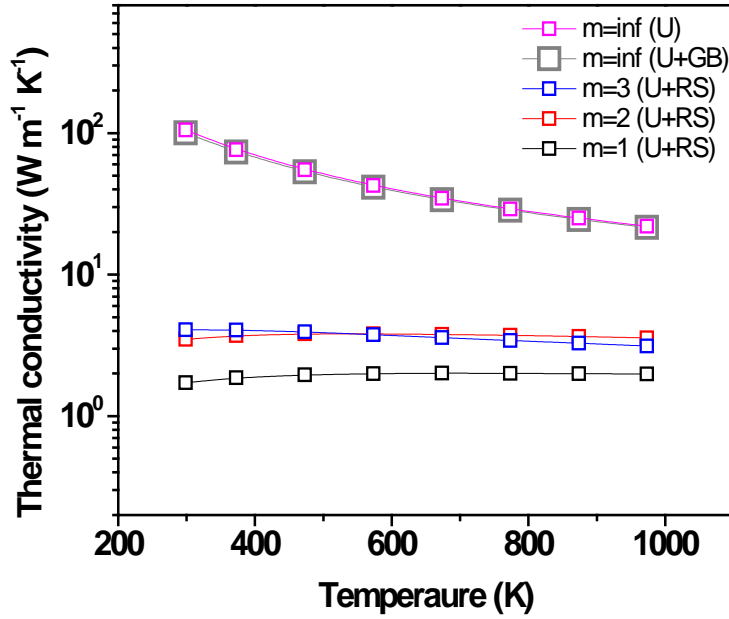


Figure 58: The temperature-dependent thermal conductivities of the undoped $m=1,2,3$, and inf structures. The values were calculated based on the Callaway model and on the sound velocities and Debye temperatures that were obtained from first-principles.

It is shown in Fig. 58 that the thermal conductivities calculated for the $m=2$ and 3 structures closely overlap, which is not expected for such a small difference of one lattice parameter between the two phonon mean free paths in $m=2$ and 3 . We associate this proximity of thermal conductivity values to the differences between sound velocities or Debye temperatures that were calculated for the RP phases. This means that an inaccuracy in these values obtained from first-principles (that might arise from several reasons, such as complexity of unit cells etc.) may obscure the distinction between the different periodicities (m -values). We, therefore, assume constant values of sound velocity and Debye temperatures for all structures, which are averaged from the values listed in Table 5. These values are: $v_s=4549$ m/s and $T_D=627$ K. This procedure allows us to calculate the thermal conductivity values for $m=4$ and 5 , as well. We note that we did not manage to produce these phases experimentally; however, we use these calculations for comparative purpose. Applying the above-described procedure, we calculated the temperature-dependent thermal conductivities for all undoped structures of $m=1, 2, 3, 4, 5$, and inf . The results appear in Figs. 59 and 60. Again, it can be seen in

Fig. 59 that scattering from grain boundaries can be neglected; moreover, there is a reduction in the thermal conductivity values of the RP phases compared to the $m=\infty$ one. Furthermore, one can observe that the reduction is systematic, which means that the thermal conductivity decrease with increasing RS planes density (decrease in m); this applies for all m -values, and is clearly seen in Fig. 60.

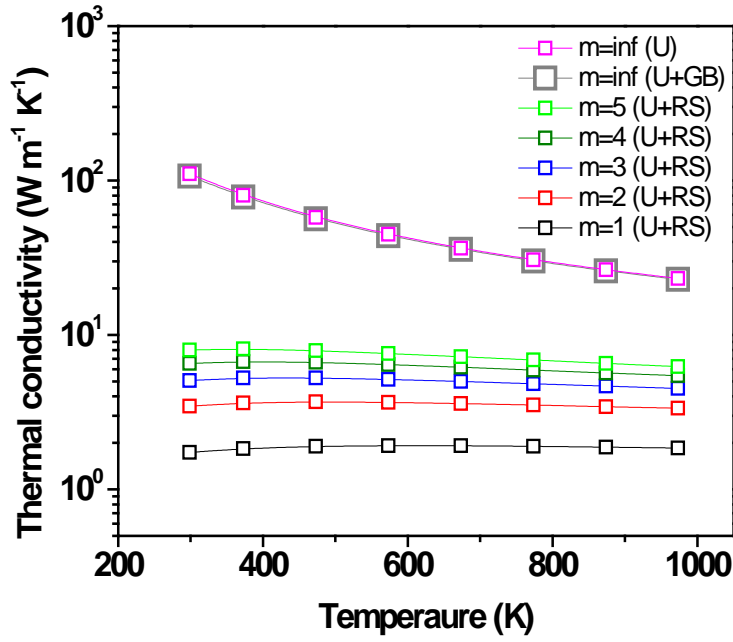


Figure 59: The temperature-dependent thermal conductivities of the undoped $m=1, 2, 3, 4, 5$, and ∞ structures. The values were calculated based on the Callaway model and on the average sound velocities and Debye temperatures that were obtained from first-principles

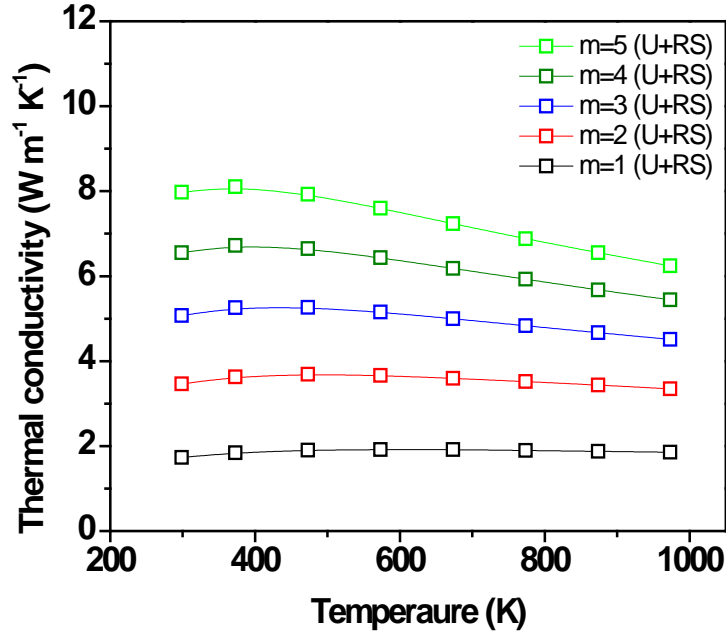


Figure 60: The temperature-dependent thermal conductivities of the undoped $m=1, 2, 3, 4$, and 5 structures. The values were calculated based on the Callaway model and on the average sound velocities and Debye temperatures that were obtained from first-principles

Comparison between the experimental thermal conductivity values of the Nb-doped samples shown in Fig. 57 and the calculated results shown in Figs. 59 and 60 reveals a remarkable similarity. This evidently proves our hypothesis that dense, extra CaO-planes should reduce thermal conductivity. We note that the quantitative values calculated based on the Callaway model should be regarded carefully, as this model is predictive in terms of the dependence of thermal conductivity on temperature and defects concentration only, however does not attempt to predict the thermal conductivity values accurately. In this context, it is noteworthy that both experimental (Fig. 57) and calculated (Figs. 58 and 59) results indicate a weak dependence of the thermal conductivity on temperature, that is, the difference between the thermal conductivities for the different m -values prevails up to 1000 K. This trend is not very common,⁴ as usually the influence of lattice defects on thermal conductivity diminishes at higher temperatures, and the conductivity values of the defect-free and “perfect” lattices approach each other. This finding is very important on the applicative aspect, as it means that the advantage

that we obtained by reduction of thermal conductivity can compensate for the concomitant reduction of electrical conductivity at elevated temperatures.

It should also be noted that the good agreement between the experimental (Fig. 57) and calculated (Figs. 58 and 59) results is valid for the RP phases mainly ($m = 1, 2, 3, 4$, and 5); this calculation, however, overestimates the thermal conductivity value for $m=\text{inf.}$ with respect to the experimental values. This can be explained by oversimplification of the $m=\text{inf.}$ structure, which is considered to be defect-free in the calculations. In practice, our $m=\text{inf.}$ materials are not defect-free.

Last, we discuss the compounds that we did not succeed to synthesize in the desirable single RP-phase forms, which were referred to as La-doped $m=3^*$, and Nb-doped $m=4^*$ and 5^* . It is shown in Fig. 56 that the La-doped $m=3^*$ material exhibits an abnormal behavior, with thermal conductivities greater than those of the $m=\text{inf.}$ specimen. This deviation is associated to the unresolved phase composition of this material, Section 4.1. Conversely, the thermal conductivity results of the Nb-doped $m=4^*$ and 5^* can be easily explained, and considered to be a weighted average of the thermal conductivity values of $m=\text{inf.}$ and $m=3$, given that their XRD spectra demonstrate this phase mixture. This explains why the thermal conductivities of these materials fall between those of $m=3$ and $m=\text{inf.}$

5.1.2. The effects of porosity

Since we produced our specimens by cold pressing and air-sintering, they contain a certain level of porosity, as shown in Section 4.2. It is, therefore, important to resolve the possible effects of porosity on thermal conductivity, to assure that they do not bias our analysis of thermal conductivity. Herein, we will consider the case of pores dispersed in a bulk matrix in the same way as that of a duplex matrix/precipitates microstructure.^{91,92} We, accordingly, apply the Callaway expression for the case of pores that are homogeneously dispersed in the bulk, having a given average diameter and number density.

We infer from the representative HRSEM micrographs shown in Section 4.2 that the average distance between the pores is not smaller than 1 μm ; assuming a simple cubical dispersion, this is equivalent to an upper limit of number density of ca. 10^{18} m^{-3} . Based on recent findings reported in literature,²⁶ such values of defect number density are not likely to influence thermal conductivity. Fig. 61 summarizes the possible effects of precipitates with given number density values on the *relative thermal conductivity*; the latter is defined as the thermal conductivity of a two-phase material incorporating precipitates of a given number density, normalized by the thermal conductivity of the pure matrix. It is shown that precipitates or pores having number density values $> 10^{20} \text{ m}^{-3}$ become effective in reducing thermal conductivity, which is not the present case. It is also noteworthy that the porosity level (i.e. pore volume fraction) by itself is not the only magnitude that should be taken into account considering phonon scattering; rather, the pore average size and number density are the relevant parameters.

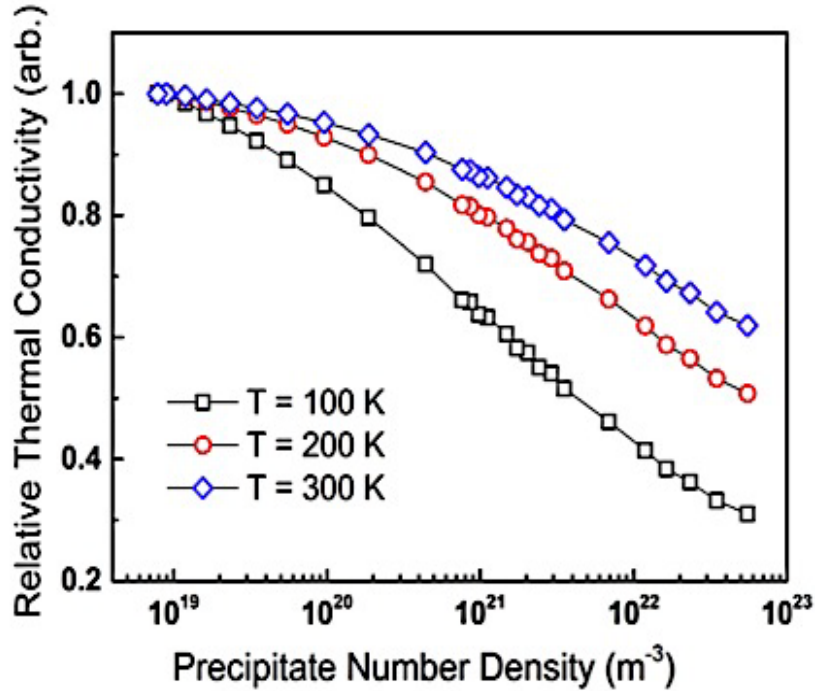


Figure 61: Relative thermal conductivity calculated using a Callaway-based model for homogeneously-dispersed precipitates of different number densities, plotted for 100 (squares), 200 (circles), and 300 K (diamonds).²⁶

5.1.3. The effects of doping

Interestingly, if we examine the effects of La- and Nb-doping on thermal conductivity values, Figs. 52-55, we can observe a general increase of the latter due to doping. This is very instructive; suggesting that these increments can be attributed to the contribution of conduction electrons to thermal conductivity, because La and Nb act as electron donors in the CaMnO_3 -system. This means that the electronic contribution to thermal conductivity, κ_e , cannot be neglected in these materials. It is noteworthy that we cannot distinguish from Figs. 52-55 which of the dopants La or Nb is more effective, since their effects are inconsistent. We assume that the effects of dopant concentrations and their chemical identity (e.g. valence) act in tandem with lattice periodicity (m-value), so that the net effect is complex and cannot be explained based on the available data.

5.2 Analysis of electrical conductivity data

Various trends in the behavior of electrical conductivity for a wide temperature range and for different lattice periodicities (m-values) and doping options are shown in section 4.2.1. To summarize the major trends, we plot the electrical conductivity at room temperature for different m-values and for either La- or Nb- doped samples is presented in Figs. 62 and 63, respectively. It is shown that the general behavior for both doping options is similar, that is, the electrical conductivity decreases with decreasing m-values, which is equivalent to increasing RS (CaO) layer density. We associate this behavior to decrease of the electrons mean free path, λ , as the RS layer density increases. This is an outcome of Eq. (5), in which the charge carrier mobility is represented by: $\mu = \frac{e\tau}{m_e}$, where τ is a charge carrier relaxation time, which can be approximated as the ratio of the charge carriers' mean free path to their drift velocity, as follows: $\tau = \frac{\lambda}{v_f}$; this form is analogous to Eq. (13). As a result, the electrical conductivity is proportional to the mean free path: ¹⁰

$$(29) \quad \sigma = \frac{ne^2}{v_f m_e} \cdot \lambda$$

We note that this formulation is a simplified description that may only qualitatively explain the trend of increasing electrical conductivity with m -values, as shown in Figs. 62 and 63.

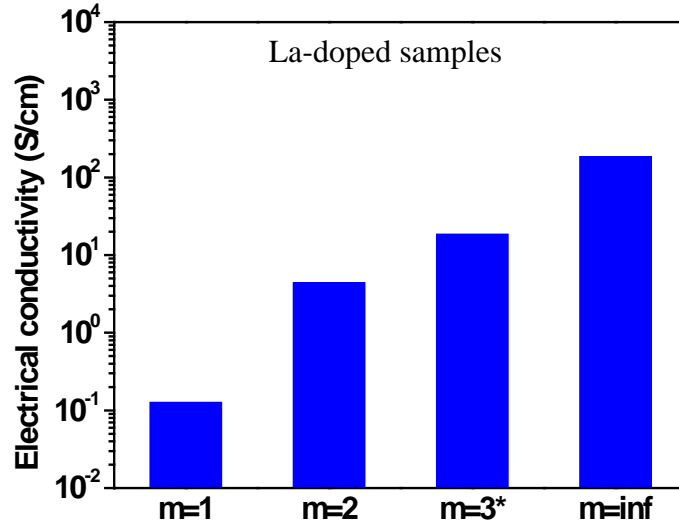


Figure 62: The room-temperature values of electrical conductivity as measured for the different m -periodicities for the La-doped samples.

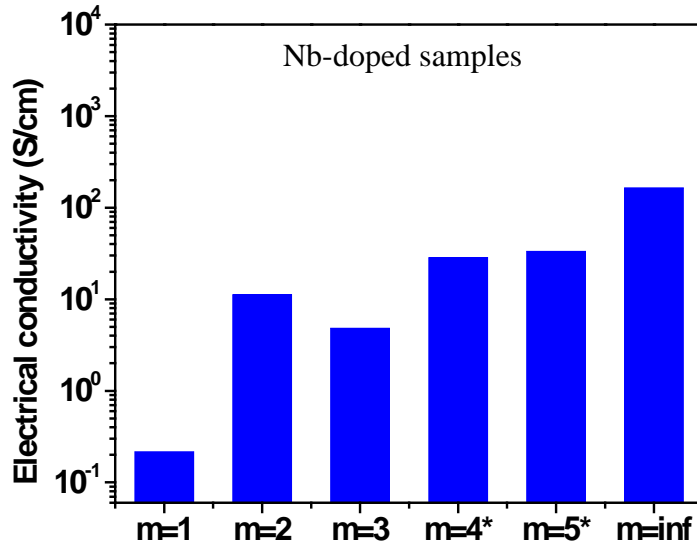


Figure 63: The room-temperature values of electrical conductivity as measured for the different m -periodicities for the Nb-doped samples.

We note that the above-mentioned simplified model may explain why the electrical conductivity grows *linearly* with m ; however, Figs. 62 and 63 indicate an *exponential* dependence on $L(m)$, as defined by Eq. (28.2). To better elucidate this trend, we adapt the approach of De Boor et al.⁹³, who applied an existing model to describe the mobility of charge carriers through a polycrystal with grain size L , where grain boundaries act as barriers with height E_B . In this model, the mobility is given by:

$$(30) \quad \mu_{GB} = Le \left(\frac{1}{2\pi m_e k_B T} \right)^{1/2} \exp \left(-\frac{E_B}{k_B T} \right)$$

Where e is an electron charge and m_e is an electron effective mass. Herein, we consider the insulating CaO-planes as E_B -high energy barriers having a finite width. When the density of CaO-planes increase, these barrier widths overlap, so that the superimposed energy barrier heights are proportional to $L(m)$. Substituting $L(m)$ for E_B in Eq. (30) resulting in exponential dependence on m as indicated by Figs. 62 and 63.

5.3 Power Factor calculation

The positive effects of the lattice periodicity, manifested by the m -values, on reducing thermal conductivity, are evident. Notwithstanding these effects, electrical conductivity is reduced by the extra CaO-planes. There is also an influence of m on the thermopower, as shown in Figs. 42 and 43. To represent the total effects of m -values on the electrical behavior, we will calculate the power factor (PF), which is defined as $PF = S^2 \sigma$, for the different m -values. The resulted PF-values for the La- and Nb-doped samples are displayed in Figs. 64 and 65, respectively. It can be seen that the PF increases with increasing temperature for all samples. Moreover, PF values of the La- and Nb-doped RP phases systematically decrease with increasing density of the CaO, attaining the greatest values for $m=\infty$. We infer from this behavior that the predominating property is the electrical conductivity.

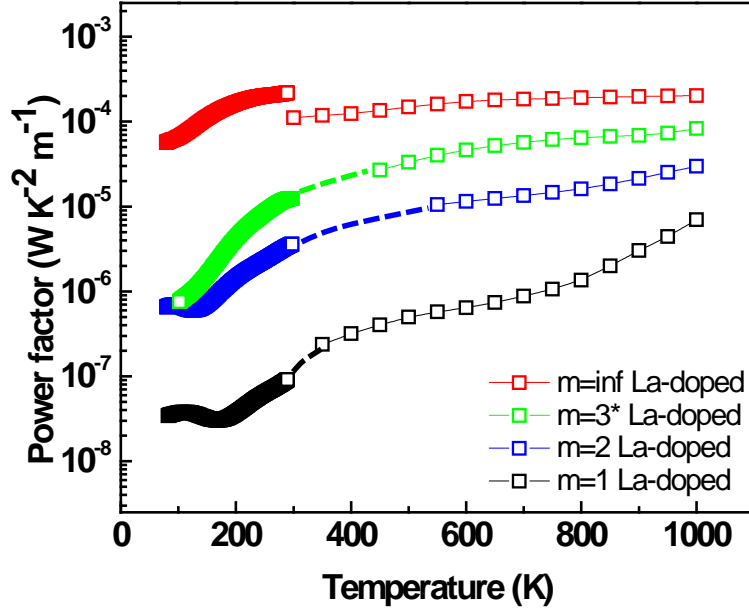


Figure 64: The temperature-dependent power factor (PF) values calculated for all La-doped samples, based on the measured thermopower and electrical conductivity.

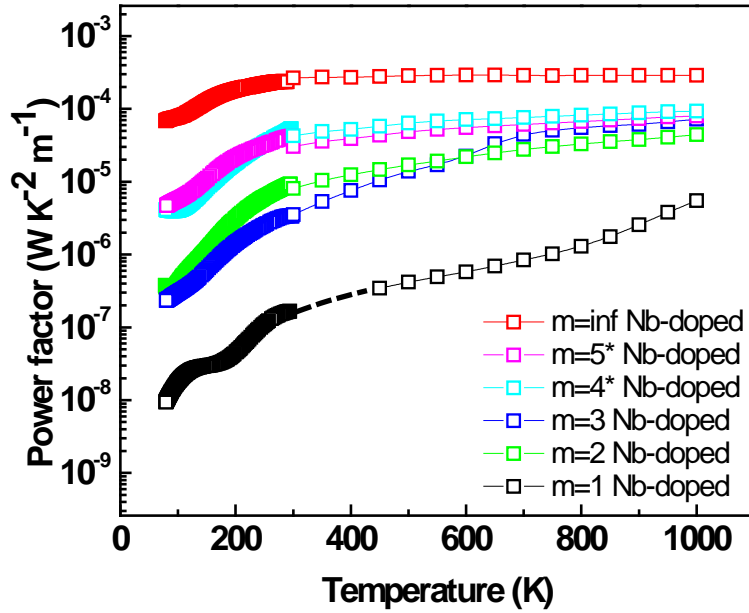


Figure 65: The temperature-dependent power factor (PF) values calculated for all Nb-doped samples, based on the measured thermopower and electrical conductivity.

To visualize the effects of lattice periodicity on the PF, we plot the ratio between the PF for a given m -value and that of $m=\text{inf.}$ at room temperature for the La- and Nb-doped specimens, for the pertinent m -values, Figs. 66 and 67, respectively. It can be seen that the RS (CaO) layers reduce the PF-values for all m -values relative to the $m=\text{inf.}$ state, whereas the ratio $\frac{PF(m)}{PF(\text{inf.})}$ increases with increasing m -values, as expected. We note that we seek adequately large $\frac{PF(m)}{PF(\text{inf.})}$ -ratios, ideally approaching unity, so that the reduction in thermal conductivity will not be compensated by the concurrent reduction in PF, yielding an overall increase in ZT. Figs 66 and 67 indicate that this is not the case, and that the best results for PR compounds are obtained for the Nb-doped materials with $m=4^*$ and 5^* and $\frac{PF(m)}{PF(\text{inf.})} \approx 0.2$.

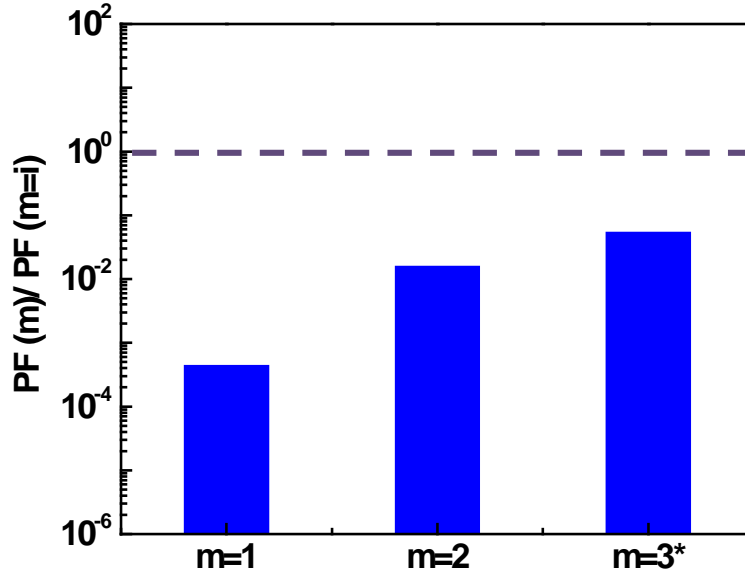


Figure 66: The ratio between the PF for a given m -value and that of $m=\text{inf.}$ at room temperature, plotted for the La-doped materials with $m=1, 2$, and 3^* .

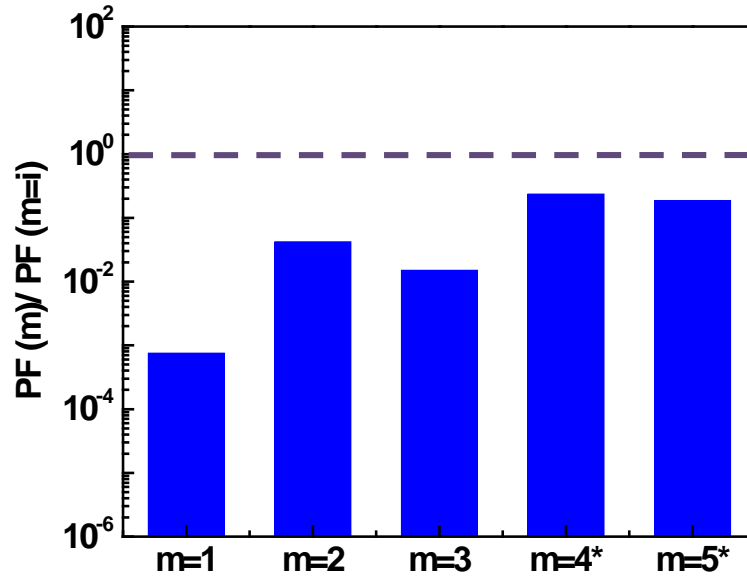


Figure 67: The ratio between the PF for a given m-value and that of m=inf. at room temperature, plotted for the Nb-doped materials with m=1, 2, 3, 4*, and 5*.

Herein, we will make a comparative analysis of the PF results obtained in our study. There are only few studies dealing with manganite-based RP phases in the TE context, however many that deal with the role of substitution elements in the m=inf. CaMnO_3 perovskite phase.^{44,48,52,54,55,59,60,94,95} On the other hand, studies which deal with TE properties of layered perovskite-type RP phases focus on SrTiO_3 (STO) based oxides, that is, the $\text{SrO}(\text{SrTiO}_3)_n$ (n=integer) system.^{68,69,96}

Wang et al.⁶⁹ and Lee et al.⁶⁸ found that the 5 at.% La- and Nb-doped m=1 STO RP phase possesses lower PF than that of the m=2 Nb-doped STO RP phase, by tens of $\mu\text{W} \cdot \text{K}^{-2} \cdot \text{m}^{-1}$, in accordance with our results. In addition, they found that the Nb-doped samples exhibit lower PFs than those of the La-doped ones, while in our research the PFs of both doping states were found to be similar. Furthermore, we note that the PFs reported by them for the STO RP phases are larger than those of our CaMnO_3 RP phases by approximately one order of magnitude. For CaMnO_3 -based RP phases with m=inf., the effects of several dopants with different concentrations were investigated. Lan et al.⁹⁵

studied several concentrations of La in CaMnO_3 compounds. Importantly, for 4 at. % substitution, they reported on PFs that well-correspond with our findings. Furthermore, they have found that this substitution concentration yields the highest PF among the investigated ones (2, 6, 8 at. %).

Wang et al.⁹⁴ investigated the TE properties of La-, Dy-, Yb- and Y- doped CaMnO_3 within the 6-18% at. % range. The materials having the lowest doping levels, 6 at. %, exhibit similar PF values compared to our 4 at. % (m=inf.) compound ($\sim 200 \mu\text{W} \cdot \text{K}^{-2} \cdot \text{m}^{-1}$ at 1000K). Moreover, the PF values of the materials with the other dopants of 6 at.% are similar to that of the La-doping (at 1000K). This means that the concentration of dopants plays a more significant role than their identity, for dopant of the same chemical nature. It was also shown by Wang et al. that the PFs decrease with increasing La-doping level, except for 10 at. %.

Similarly, Wang, Sui and Su⁵⁹ investigated the TE properties of 10 at. % La, Pr, Nd, Sm, Eu, Gd, Tb, Dy, Ho, Er, and Yb doping in the CaMnO_3 system. For 10 at. % La-doping, the PF value was found to be slightly larger (by $\sim 20 \mu\text{W} \cdot \text{K}^{-2} \cdot \text{m}^{-1}$) than that of the 4 at. % La-doped m=inf. material investigated by us; the other dopants exhibited an additional improvement in the PF values, where the highest value of $\sim 350 \mu\text{W} \cdot \text{K}^{-2} \cdot \text{m}^{-1}$ were obtained for the Dy-doping.

5.4 The figure of merit, ZT

We calculated the ZT-values for all materials based on the measured electrical conductivities, Seebeck coefficients, and thermal conductivities. The resulting ZT-values of the La- and Nb-doped samples are presented in Figs. 68 and 69, respectively. It can be seen that the ZT values of all La- and Nb-doped samples increase with increasing temperature up to 1000 K. This is a technologically-important finding, indicating that improvement of the conversion efficiency of these materials is a question of thermal stability, in contrast with the common TE compounds in which their ZT-values peak at lower temperatures. Furthermore, it is evident that for both doping options the highest

ZT is obtained for the $m=\text{inf.}$ structures, with no RS (CaO) atomic layers, and their values reach ~ 0.095 for La-doped and ~ 0.1 for Nb-doped samples at 1000 K.

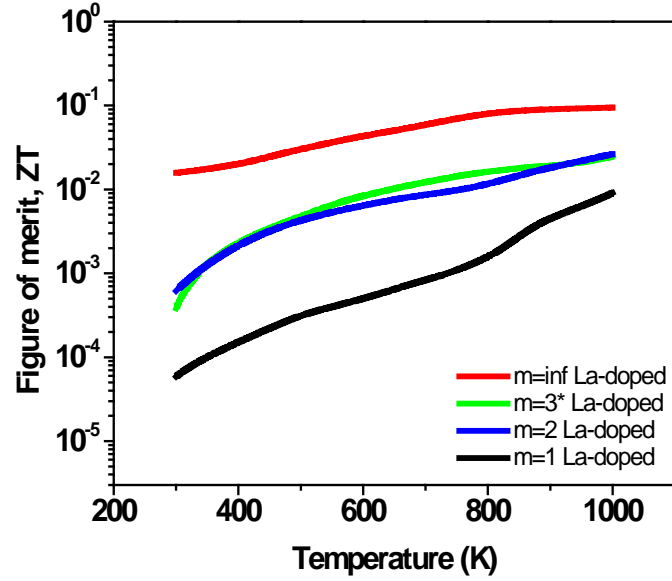


Figure 68: The temperature-dependent ZT-values calculated for all La-doped samples, based on the measured thermopower, electrical conductivities, and thermal conductivities

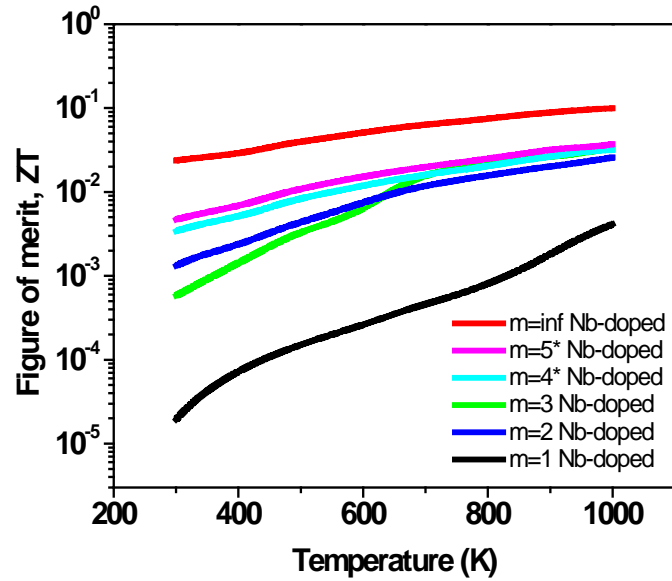


Figure 69: The temperature-dependent ZT-values calculated for all Nb-doped samples, based on the measured thermopower, electrical conductivities, and thermal conductivities

It can be concluded from Figs. 68 and 69 that although the remarkable reduction of thermal conductivity that is obtained by manipulating the m -values, the resulting ZT -values are, still, inferior to those of the base compounds having $m=\infty$ structure. This is attributed to electron scattering by the planar CaO defects.

Figure 70 displays a comparison between the ZT -values of the La- and Nb-doped specimens of the $m=\infty$ structure. It is shown that Nb-doping yields better ZT -values up to 700 K, considering uncertainty level of $\sim 10\%$ (relative error) that is common to such measurements. The ZT -values of both materials are practically identical between 700 and 1000 K.

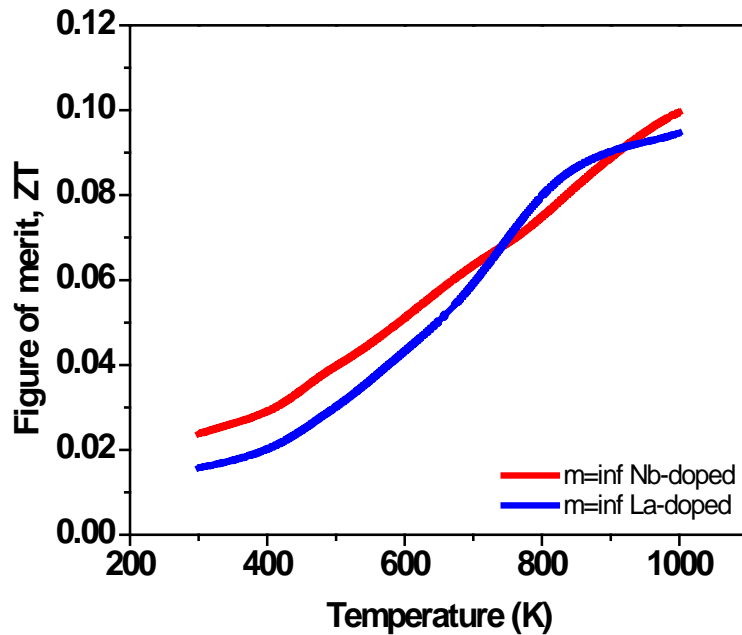


Figure 70: The temperature-dependent ZT -values calculated for the $m=\infty$ -type La- (blue) and Nb-doped (red) samples, based on the measured thermopower, electrical conductivities, and thermal conductivities.

Comparing the resulting ZT values of our manganite-based RP phases to those of the STO RP phases,^{68,69} reveals that the second ones possess higher ZT values, by approximately one order of magnitude, for both $m=1$ and 2 in either of the La or Nb doping types. Interestingly, in the STO RP system, the ZT value of the $m=1$ structure is lower than that of the $m=2$ one, in correspondence with our results.

Considering the effects of doping on ZT, Wang et al.⁹⁴ investigated the TE properties of CaMnO_3 ($m=\infty$) containing several types of dopants in concentrations ranging between 6 and 18 at.%. They have found that the ZT value attained from 6 at.% La-doping is slightly higher (0.1 at 1000K) than our results for 4 at.% La-doping (0.95 at 1000K), and that there is no improvement with changing the dopant type. However, for the 10 at.% compounds they found an increase in the ZT value reaching at 0.12 for La-doping, and at a value of 0.2 for Dy- and Yb-doping. Other studies show $\text{ZT}=0.16$ at 1000 K for 10 at. % Yb-doping,⁵⁴ and $\text{ZT}=0.07$ for Bi-doping.⁴⁸

We emphasize the important influence of the synthesis method on the resulting functional properties, among them is the TE ZT. Bocher et al.⁶⁰ investigated the TE properties of CaMnO_3 with several Nb-doping levels of 2, 5, and 8 at. % ($m=\infty$) that were synthesized in two different methods: “chimie douce” (SC), and the classical solid state reaction (SSR). The SSR method reported by them is the most closely-related to our processing method. Indeed, they report on $\text{ZT}=0.75$ at 1000 K for 5 at. % Nb-doping, which is slightly lower than that achieved by us at similar conditions, 0.95. The highest ZT-values obtained for both methods are obtained for a 2 at.% doped compound, with a clear preference to the SC method (for all compositions) reaching the highest ZT value of 0.32.

In conclusion, we obtain ZT-values for the base compounds ($m=\infty$) that are comparable with those reported in literature, pointing on the reliability of the materials synthesis and measurements applied by us. The ZT-values obtained for the modulated structures having $m=1$ through 5 are inferior to those obtained for the base materials, though the remarkable decrease of thermal conductivity. We associate this to electron scattering due to the extra CaO atomic planes. We believe that further study of the RP compounds including variation of dopants and concentrations, as well as employing other synthesis methods that yield lower porosity levels, will result in improvement of ZT.

6. Summary, conclusions, and recommendations for further research

Our study focuses on $\text{CaO}(\text{CaMnO}_3)_m$ n-type perovskites ($m=\text{inf.}; 1$ through 5), which are modulated structures, formed of m perovskite CaMnO_3 layers separated by a rock-salt CaO layer. We aim at drawing the correlation between thermal conductivity and the planar defects periodicity, denoted by m , in $\text{CaO}(\text{CaMnO}_3)_m$ - based compounds. We prepare several pure, La- and Nb- doped $\text{CaO}(\text{CaMnO}_3)_m$ compounds with different periodicities (m -values) by mixing of elemental powders and sintering at temperatures up to 1673 K. We perform basic materials characterization employing XRD and high-resolution SEM in concert with laser flash analysis (LFA) for thermal conductivity measurements as well as electrical conductivity and thermopower measurements at the range of 300 through 1000 K. Our main findings are summarized as follows:

1. We managed to synthesize Ruddlesden-Popper phases of the $\text{CaO}(\text{CaMnO}_3)_m$ form that are either undoped or doped with 4 at.% La or Nb, having the periodicities of $m = \text{inf.}, 1$, and 2) for La-doping, and $m = \text{inf.}, 1, 2$, and 3) for Nb-doping. The rest ($m=3^*$ La-doped; $m=4^*$ and 5^* Nb-doped) were classified by us as mixtures of lower- m RP phases.
2. The $\text{CaO}/(\text{CaMnO}_3)_m$ multilayering configurations significantly reduce the thermal conductivity values, compared to the $m=\text{inf.}$ base materials ; this is accompanied, however, with a reduction in electrical conductivity and power factor, as well.
3. La- and Nb-substitutions for the Ca- and Mn- sublattice sites, respectively, increase the electrical conductivity. In turn, the Seebeck coefficient values decrease.
4. The differences in the electrical conductivity values of the RP phases decrease with increasing temperature, whereas the differences in thermal conductivity values are maintained up to 1000 K, which have technological implications for high-temperatures.

5. The greatest ZT-values were obtained by us for $m=\infty$ at 1000 K, and are 0.95 and 0.1 for La- or Nb-doping, respectively. These values are typical for calcium-manganite compounds. In spite of the desirable reduction in thermal conductivity, the obtained ZT-values of the RP phases are still low compared to those of the $m=\infty$ phases, possibly due to charge carrier scattering from the CaO layers.

In view of the above, there are several questions that remain open, and should be addressed. On the technological aspect:

- What is the dopant that will lead to the best TE performance? Further doping elements that should be examined are rare-earth elements or transition metal atoms.
- What is the optimal dopant concentration that will lead to the greatest ZT values? Their effects on the electrical and thermal conductivities as well as thermopower, individually, should be studied.
- The synthesis method applied in this study is room-temperature uniaxial powder pressing followed by air-sintering, which yields porous materials. We believe that the pores contribute to electron scattering, thereby reducing electrical conductivity and, consequently, the power factor. In view of this, it is recommended to apply hot-pressing in further study, which is expected to result in greater ZT-values.

On the scientific level, the following questions should be addressed:

- It is known that the La-doping atoms substitute for the Ca-sites; However, it is yet unknown whether they prefer to occupy the perovskite or rock-salt phase.
- How should this substitution preference affect TE properties? e.g. the efficiency of scattering from CaO/MnO₃ interfaces, that is manifested in transport properties.
- How should the above change for other doping elements? Nb, for example?
- Besides the presence of extra CaO-planes, will the doping atoms affect thermal conductivity by means of impurity scattering?
- It is known that thermal conductivity of the La-doped compounds differ from that of the undoped specimen. What is the reason for this behavior? What is the

significance of the electronic component of thermal conductivity?

The above fundamental questions imply that we need to tightly-correlate between TE properties and the materials' atomistic structure, including atomic positions. They could be addressed in a careful combination between TE measurements, high-resolution TEM (HR-TEM) analysis, and total energy-based DFT calculations.

7. References

1. Snyder, G. J. & Toberer, E. S. Complex thermoelectric materials. *Nat. Mater.* **7**, 105–114 (2008).
2. Zebarjadi, M., Esfarjani, K., Dresselhaus, M. S., Ren, Z. F. & Chen, G. Perspectives on thermoelectrics: from fundamentals to device applications. *Energy Environ. Sci.* **5**, 5147 (2012).
3. Seebeck, T. . Ueber die magnetische Polarisation der Metalle und Erze durch Temperatur-Differenz. *Ann. Phys.* **82**, 133–160 (1826).
4. Rowe, D. M. CRC Handbook of Thermoelectrics. *New York* **16**, 1251–1256 (1995).
5. Tritt, T. M. & Subramanian, M. A. Thermoelectric Materials , Phenomena , and Applications : A Bird ' s Eye View. *MRS Bull.* **31**, 188–198 (2006).
6. Li, J.-F., Liu, W.-S., Zhao, L.-D. & Zhou, M. High-performance nanostructured thermoelectric materials. *NPG Asia Mater.* **2**, 152–158 (2010).
7. Ioffe, A. F. *Semiconductor Thermoelements and Semiconductor Colling*, Infosearch, London, UK. (1957).
8. Shakouri, A. Recent Developments in Semiconductor Thermoelectric Physics and Materials. *Annu. Rev. Mater. Res.* **41**, 399–431 (2011).
9. Ohtaki, M. Oxide Thermoelectric Materials for Heat-to-Electricity Direct Energy Conversion. *Kyushu Univ. Glob. COE Progr. Nov. Carbon Resour. Sci. Newsl.* **5**, (2010).
10. Ashcroft, N. W. & Mermin, N. D. *Solid State Physics. Solid State Phys.* **2**, 848 (Brooks Cole, 1976).
11. Kittel, C. *Introduction to Solid State Physics 7th edition. John Wiley Sons* (1996).
12. He, J., Liu, Y. & Funahashi, R. Oxide thermoelectrics: The challenges, progress, and outlook. *J. Mater. Res.* **26**, 1762–1772 (2011).
13. Terasaki, I., Sasago, Y. & Uchinokura, K. Large thermoelectric power in NaCo₂O₄ single crystals. *Phys. Rev. B* **56**, 685–687 (1997).
14. Masset, A. *et al.* Misfit-layered cobaltite with an anisotropic giant magnetoresistance: Ca₃Co₄O₉. *Phys. Rev. B* **62**, 166–175 (2000).

15. Sootsman, J. R., Chung, D. Y. & Kanatzidis, M. G. New and old concepts in thermoelectric materials. *Angew. Chem. Int. Ed. Engl.* **48**, 8616–8639 (2009).
16. Koumoto, K., Wang, Y., Zhang, R., Kosuga, A. & Funahashi, R. Oxide Thermoelectric Materials: A Nanostructuring Approach. *Annu. Rev. Mater. Res.* **40**, 363–394 (2010).
17. Tritt, T. M. *Thermal Conductivity: Theory, Properties, and Applications*. (springer, 2004).
18. Holland, M. Analysis of Lattice Thermal Conductivity. *Phys. Rev.* **132**, 2461–2471 (1963).
19. Hill, T. L. *An Introduction to Statistical Thermodynamics*. (Dover publications, 1986).
20. Callaway, J. Model for Lattice Thermal Conductivity at Low Temperatures. *Phys. Rev.* **113**, 1046–1051 (1959).
21. He, J., Girard, S. N., Kanatzidis, M. G. & Dravid, V. P. Microstructure-Lattice Thermal Conductivity Correlation in Nanostructured PbTe 0.7 S 0.3 Thermoelectric Materials. *Adv. Funct. Mater.* **20**, 764–772 (2010).
22. Kim, W. *et al.* Reducing thermal conductivity of crystalline solids at high temperature using embedded nanostructures. *Nano Lett.* **8**, 2097–9 (2008).
23. Wu, L. J. *et al.* Nanostructures and defects in thermoelectric AgPb₁₈SbTe₂₀ single crystal. *J. Appl. Phys.* **105**, (2009).
24. He, J. *et al.* On the origin of increased phonon scattering in nanostructured PbTe based thermoelectric materials. *J. Am. Chem. Soc.* **132**, 8669–8675 (2010).
25. Kim, W. *et al.* Thermal conductivity reduction and thermoelectric figure of merit increase by embedding nanoparticles in crystalline semiconductors. *Phys. Rev. Lett.* **96**, 045901 (2006).
26. Amouyal, Y. Reducing Lattice Thermal Conductivity of the Thermoelectric Compound AgSbTe₂ (P4/mmm) by Lanthanum Substitution: Computational and Experimental Approaches. *J. Electron. Mater.* **43**, 3772 (2014).
27. Callaway, J. & von Baeyer, H. Effect of Point Imperfections on Lattice Thermal Conductivity. *Phys. Rev.* **120**, 1149–1154 (1960).
28. Morelli, D., Heremans, J. & Slack, G. Estimation of the isotope effect on the lattice thermal conductivity of group IV and group III-V semiconductors. *Phys. Rev. B* **66**, 195304 (2002).

29. Steigmeier, E. & Abeles, B. Scattering of Phonons by Electrons in Germanium-Silicon Alloys. *Phys. Rev.* **136**, A1149–A1155 (1964).
30. Yang, L., Wu, J.-S. & Zhang, L.-T. Effect of phonon scattering mechanisms on the lattice thermal conductivity of skutterudite- related compound. *Chin. Phys. Lett.* **13**, 516–521 (2004).
31. Chen, G., Zeng, T., Borca-Tasciuc, T. & Song, D. Phonon engineering in nanostructures for solid-state energy conversion. *Mater. Sci. Eng. A* **292**, 155–161 (2000).
32. Kumar, G. S., Prasad, G. & Pohl, R. O. Experimental determinations of the Lorenz number. *J. Mater. Sci.* **28**, 4261–4272 (1993).
33. Nolas, G. S., Morelli, D. T. & Tritt, T. M. SKUTTERUDITES: A Phonon-Glass-Electron Crystal Approach to Advanced Thermoelectric Energy Conversion Applications. *Annu. Rev. Mater. Sci.* **29**, 89–116 (1999).
34. Kanatzidis, M. G. *Recent Trends in Thermoelectric Materials Research I. Semicond. Semimetals* **69**, 51–100 (Elsevier, 2001).
35. Minnich, A. J., Dresselhaus, M. S., Ren, Z. F. & Chen, G. Bulk nanostructured thermoelectric materials: current research and future prospects. *Energy Environ. Sci.* **2**, 466 (2009).
36. Venkatasubramanian, R., Siivola, E., Colpitts, T. & O’Quinn, B. Thin-film thermoelectric devices with high room-temperature figures of merit. *Nature* **413**, 597–602 (2001).
37. Kim, W. *et al.* Reducing thermal conductivity of crystalline solids at high temperature using embedded nanostructures. *Nano Lett.* **8**, 2097–2099 (2008).
38. Vineis, C. J., Shakouri, A., Majumdar, A. & Kanatzidis, M. G. Nanostructured thermoelectrics: big efficiency gains from small features. *Adv. Mater.* **22**, 3970–3980 (2010).
39. Chen, G. *Recent Trends in Thermoelectric Materials Research III. Semicond. Semimetals* **71**, 203–259 (Elsevier, 2001).
40. Bhandari, C. M. & Rowe, D. M. Boundary scattering of phonons. *J. Phys. C Solid State Phys.* **11**, 1787–1794 (1978).
41. Biswas, K. *et al.* High-performance bulk thermoelectrics with all-scale hierarchical architectures. *Nature* **489**, 414–418 (2012).

42. Sharp, J. W. & Goldsmid, H. J. Boundary Scattering of Charge Carriers and Phonons. in *18th Int. Conf. Thermoelectr.* 709–712 (1999).
43. Ziman, J. *Electrons and phonons: the theory of transport phenomena in solids. Semicond. Semimetals*, 2000, 69, 51-100. **69**, (Oxford University Press,, 1960).
44. Bocher, L. *et al.* Thermoelectric and magnetic properties of perovskite-type manganate phases synthesised by ultrasonic spray combustion (USC). *Solid State Sci.* **10**, 496–501 (2008).
45. Ohta, S., Ohta, H. & Koumoto, K. Grain Size Dependence of Thermoelectric Performance of Nb-Doped SrTiO₃ Polycrystals. *J. Ceram. Soc. Japan* **114**, 102–105 (2006).
46. Robert, R., Bocher, L., Sipos, B., Döbeli, M. & Weidenkaff, A. Ni-doped cobaltates as potential materials for high temperature solar thermoelectric converters. *Prog. Solid State Chem.* **35**, 447–455 (2007).
47. Kobayashi, T. *et al.* Metal-Insulator in the System Transition and Thermoelectric Properties (R1-xCax) MnO₃-l (R : Tb , Ho , Y). *J. Solid State Chem.* **92**, 116–129 (1991).
48. Ohtaki, M., Koga, H., Tokunaga, T., Eguchi, K. & Arai, H. Electrical Transport Properties and High-Temperature Thermoelectric Performance of (Ca_{0.9}M_{0.1})MnO₃ (M=Y, La, Ce, Sm, In, Sn, Sb, Pb, Bi). *J. Solid State Chem.* **120**, 105–111 (1995).
49. Pi, L., Hébert, S., Martin, C., Maignan, A. & Raveau, B. Comparison of CaMn_{1-x}RuxO₃ and CaMn_{1-y}MoyO₃ perovskites. *Phys. Rev. B* **67**, 024430–7 (2003).
50. Thao, P. X., Tsuji, T., Hashida, M. & Yamamura, Y. High Temperature Thermoelectric Properties of Ca_{1-x}DyxMnO_{2.98} (0≤x≤0.2). *J. Ceram. Soc. Japan* **111**, 544–547 (2003).
51. Cong, B. T., Tsuji, T., Thao, P. X., Thanh, P. Q. & Yamamura, Y. High-temperature thermoelectric properties of Ca_{1-x}PrxMnO_{3-δ} (0≤x<1). *Phys. B Condens. Matter* **352**, 18–23 (2004).
52. Xu, G. *et al.* High-temperature transport properties of Nb and Ta substituted CaMnO₃ system. *Solid State Ionics* **171**, 147–151 (2004).
53. Miclau, M., Hébert, S., Retoux, R. & Martin, C. Influence of A-site cation size on structural and physical properties in Ca_{1-x}SrxMn_{0.96}Mo_{0.04}O₃: A comparison of the and 0.6 compounds. *J. Solid State Chem.* **178**, 1104–1111 (2005).

54. Flahaut, D. *et al.* Thermoelectrical properties of A-site substituted $\text{Ca}_{1-x}\text{R}_x\text{MnO}_3$ system. *J. Appl. Phys.* **100**, 084911 (2006).
55. Bocher, L. *et al.* High-temperature stability, structure and thermoelectric properties of $\text{CaMn}_{1-x}\text{Nb}_x\text{O}_3$ phases. *Acta Mater.* **57**, 5667–5680 (2009).
56. Hung, L. T. *et al.* High-temperature thermoelectric properties of $\text{Ca}_{0.9}\text{Y}_{0.1}\text{Mn}_{1-x}\text{Fe}_x\text{O}_3$ ($0 \leq x \leq 0.25$). *J. Mater. Sci.* **48**, 2817–2822 (2013).
57. Aguirre, M. H. *et al.* Structure, microstructure, and high-temperature transport properties of $\text{La}_{1-x}\text{Ca}_x\text{MnO}_{3-\delta}$ thin films and polycrystalline bulk materials. *J. Appl. Phys.* **103**, 013703 (2008).
58. Weidenkaff, A. *et al.* Development of thermoelectric oxides for renewable energy conversion technologies. *Renew. Energy* **33**, 342–347 (2008).
59. Wang, Y., Sui, Y. & Su, W. High temperature thermoelectric characteristics of $\text{Ca}_{0.9}\text{R}_{0.1}\text{MnO}_3$ ($\text{R}=\text{La}, \text{Pr}, \text{Yb}$). *J. Appl. Phys.* **104**, 093703 (2008).
60. Bocher, L. *et al.* $\text{CaMn}_{1-x}\text{Nb}_x\text{O}_3$ ($x \leq 0.08$) perovskite-type phases as promising new high-temperature n-type thermoelectric materials. *Inorg. Chem.* **47**, 8077–8085 (2008).
61. Tritt, T. M. Holey and Unholey Semiconductors. *Science* (80-.). **283**, 804–805 (1999).
62. Maignan, A., Martin, C., Damay, F., Raveau, B. & Hejtmanek, J. Transition from a paramagnetic metallic to a cluster glass metallic state in electron-doped perovskite manganites. *Phys. Rev. B* **58**, 2758–2763 (1998).
63. Logvinovich, D. *et al.* Synthesis, Mo-valence state, thermal stability and thermoelectric properties of $\text{SrMoO}_{3-x}\text{N}_x$ ($x > 1$) oxynitride perovskites. *J. Solid State Chem.* **180**, 2649–2654 (2007).
64. Lee, S.-M., Cahill, D. G. & Venkatasubramanian, R. Thermal conductivity of Si–Ge superlattices. *Appl. Phys. Lett.* **70**, 2957 (1997).
65. Capinski, W. *et al.* Thermal-conductivity measurements of GaAs/AlAs superlattices using a picosecond optical pump-and-probe technique. *Phys. Rev. B* **59**, 8105–8113 (1999).
66. Touzelbaev, M. N., Zhou, P., Venkatasubramanian, R. & Goodson, K. E. Thermal characterization of $\text{Bi}_2\text{Te}_3/\text{Sb}_2\text{Te}_3$ superlattices. *J. Appl. Phys.* **90**, 763 (2001).

67. Ruddlesden, S. N. & Popper, P. The compound $\text{Sr}_3\text{Ti}_2\text{O}_7$ and its structure. *Acta Crystallogr.* **11**, 54–55 (1958).
68. Lee, K. H., Ohta, H. & Koumoto, K. Thermoelectric properties of layered perovskite-type Nb-doped $\text{SrO}(\text{SrTiO}_3)_n$ ($n=1,2$) Ruddlesden-popper phases. **1**, 3–6 (2006).
69. Wang, Y., Lee, K., Ohta, H. & Koumoto, K. Fabrication and thermoelectric properties of heavily rare-earth metal-doped $\text{SrO}(\text{SrTiO}_3)_n$ ($n= 1, 2$) ceramics. *Ceram. Int.* **34**, 849–852 (2008).
70. Fisher, B., Patlagan, L., Reisner, G. & Knizhnik, a. Systematics in the thermopower of electron-doped layered manganites. *Phys. Rev. B* **61**, 470–475 (2000).
71. Misture, S. & Edwards, D. High-temperature oxide thermoelectrics. *Am. Ceram. Soc. Bull.* **91**, 24–27 (2012).
72. Raveau, B., Zhao, Y. M., Martin, C., Hervieu, M. & Maignan, A. Mn-Site Doped CaMnO_3 : Creation of the CMR Effect. *J. Solid State Chem.* **149**, 203–207 (2000).
73. Smits, F. M. Measurement of Sheet Resistivities with the Four-Point Probe. *Bell Syst. Tech. J.* **37**, 711–718 (1958).
74. Capelle, K. A Bird's-Eye View of Density-Functional Theory. *Brazilian J. Phys.* **36**, 1318–1343 (2006).
75. Kohn, W. & Hohenberg, P. Inhomogeneous Electron Gas. *Phys. Rev.* **136**, B864–B871 (1964).
76. Kohn, W. & Sham, L. J. Self-Consistent Equations Including Exchange and Correlation Effects. *Phys. Rev.* **140**, A1133–A1138 (1965).
77. Parr, R. G. & Yang, W. *Density-Functional Theory of Atoms and Molecules-Oxford University Press, USA. Oxford Univ. Press. New York* (1989).
78. Mishin, Y., Asta, M. & Li, J. Atomistic modeling of interfaces and their impact on microstructure and properties. *Acta Mater.* **58**, 1117–1151 (2010).
79. Martin, R. M. *Electronic Structure: Basic Theory and Practical Methods. Book 624* (Cambridge University Press, 2004). at <http://books.google.com/books?id=dmRTFLpSGNsC>
80. Kresse, G. & Furthmüller, J. Efficiency of ab-initio total energy calculations for metals and semiconductors using a plane-wave basis set. *Comput. Mater. Sci.* **6**, 15–50 (1996).

81. Kresse, G. & Furthmüller, J. Efficient iterative schemes for ab initio total-energy calculations using a plane-wave basis set. *Phys. Rev. B* **54**, 11169–11186 (1996).
82. Kresse, G. & Hafner, J. Ab initio molecular-dynamics simulation of the liquid-metal-amorphous-semiconductor transition in germanium. *Phys. Rev. B* **49**, 14251–14269 (1994).
83. MedeA, v. 2.7.4, Materials Design, Inc. Angel Fire, NM, USA, (2010). 2010 (2010).
84. Perdew, J., Burke, K. & Ernzerhof, M. Generalized Gradient Approximation Made Simple. *Phys. Rev. Lett.* **77**, 3865–3868 (1996).
85. Kresse, G. & Joubert, D. From ultrasoft pseudopotentials to the projector augmented-wave method. *Phys. Rev. B* **59**, 1758–1775 (1999).
86. Monkhorst, H. J. & Pack, J. D. Special points for brillouin-zone integrations. *Phys. Rev. B* **13**, 5188–5192 (1976).
87. Kinsler, L. E., Frey, A. R., Coppens, A. B. & Sanders, J. V. *Fundamentals of acoustics. Fundam. Acoust. 4th Ed. by Lawrence E. Kinsler, Austin R. Frey, Alan B. Coppens, James V. Sanders, pp. 560. ISBN 0-471-84789-5. Wiley-VCH, December 1999.* **1**, 560 (1999).
88. Joseph, E. & Amouyal, Y. Enhancing thermoelectric performance of PbTe-based compounds by substituting elements: a first-principles study. *J. Elect. Mater.* (2014).
89. Amouyal, Y. On the role of lanthanum substitution defects in reducing lattice thermal conductivity of the AgSbTe₂ (P4/mmm) thermoelectric compound for energy conversion applications. *Comput. Mater. Sci.* **78**, 98–103 (2013).
90. Anderson, O. L. A simple method for calculating the debye temperature from elastic constant. *Phys. Chem. Solids* **24**, 909–917 (1963).
91. Tarkhanyan, R. H. & Niarchos, D. G. Reduction in lattice thermal conductivity of porous materials due to inhomogeneous porosity. *Int. J. Therm. Sci.* **67**, 107–112 (2013).
92. Tarkhanyan, R. H., Ioannidou, a. & Niarchos, D. G. Lattice Thermal Conductivity in Nano- to Micro-scale Porous Materials. *Metall. Mater. Trans. E* **1**, 145–152 (2014).
93. De Boor, J. *et al.* Microstructural effects on thermoelectric efficiency: A case study on magnesium silicide. *Acta Mater.* **77**, 68–75 (2014).

94. Wang, Y. *et al.* High Temperature Thermoelectric Response of Electron-Doped CaMnO₃. *Chem. Mater.* **21**, 4653–4660 (2009).
95. Lan, J. *et al.* High-temperature Electric Properties of Polycrystalline La-doped CaMnO₃ Ceramics. **25**, 535–538 (2009).
96. Lee, K. H., Wang, Y. F. & Kim, S. W. Thermoelectric Properties of Ruddlesden–Popper Phase n-Type Semiconducting Oxides: La-, Nd-, and Nb-Doped Sr₃Ti₂O₇. *J. Appl. Ceram. Technol.* **4**, 326–331 (2007).

**השפעת פגמי גביש על התכונות
התרמואלקטריות בתחמוצות סידן מנגן
ליישומי המרת אנרגיה**

איילת גרף

**השפעת פגמי גביש על התכונות
התרמואלקטריות בתחמוצות סידן מנגן
ליישומי המרת אנרגיה**

חיבור על מחקר

לשם מילוי חלקי של הדרישות לקבלת תואר מגיסטר
למדעים במדע והנדסה של חומרים

איילת גרף

הוגש לסנאט הטכניון – מכון טכנולוגי לישראל

תשרי תשע"ד, חיפה, ספטמבר 2014

המחקר נעשה בהנחייתו של פרופ"מ ירון אמויאל בפקולטה למדע והנדסה של חומרים בטכניון – מכון
טכנולוגי לישראל.

אני מודה לטכניון וכמו כן לתוכנית נבט של תוכנית האנרגיה בטכניון על התמיכה הכספית הנדיבה במהלך
השתלמותי.

תקציר

במשק האנרגיה העולמי נעשים מאמצים רבים לפיתוח מקורות אנרגיה חדשים ליצירת חשמל, שבשונה מדלקים פחמימניים, אינם מזהמים את האוויר ואינם יקרים. לכן, התמרה ישירה של חום בלתי מנוצל לחשמל זוכה לעניין רב. ניצול חום שנפלט לסביבה מתהליכים שונים ליצירת אנרגיה חשמלית יכול להתבצע ע"י שימוש בחומרים תרמואלקטריים. חומרים אלו, מבוססים על אפקט Seebeck אשר התגלה בשנת 1821. לפי אפקט זה, כאשר מחממים צומת הנוצרת מחיבור בין שני חומרים שונים נוצר מתח חשמלי בצומת, בצד בו אינם מחוברים.

מעגל תרמואלקטרי בסיסי מורכב משני מוליכים למחצה מסוגים p - n , אשר מחוברים למוליך בצד החם. בהנתן הפרש טמפרטורה, מתרחשת דיפוזיה של נושאי מטען מהכיוון החם לעבר הכיוון הקר. כתוצאה מכך, נוצר מתח הדקים התלוי בהפרש הטמפרטורות, ומאפשר זרם במעגל החיצוני. התקן תרמואלקטרי בנוי ממערך של צמתי p - n אשר מחוברים חשמלית בטור ותרמית במקביל.

מאפיין חשוב של החומרים התרמואלקטרים הינו "גורם הטיב" התרמואלקטרי, המסומן כ- Z והינו פונקציה משוקללת של שלושה מאפיינים בסיסיים של החומר: מקדם Seebeck, S , מוליכות החשמלית, σ , ומוליכות תרמית, κ . המכפלה של גורם הטיב התרמואלקטרי בטמפרטורה, המסומנת כ- ZT , משמשת כמדד ליעילות החומר התרמואלקטרי. כלומר, ככל ש- ZT גבוה יותר עבור חומר מסוים, כך הנצילות התרמודינמית המתקבלת משימוש בחומר זה גבוהה יותר. גודל חשוב נוסף הוא ה- Power Factor , המסומן כ- PF , ומוגדר כמכפלה של σ ו- S^2 . גודל זה מאגד את התכונות החשמליות של החומר ולכן מאפיין את החומרים התרמואלקטרים מבחינה חשמלית. על מנת לקבל חומר תרמואלקטרי בעל יעילות מקסימלית, ישנה דרישה ל- ZT גבוה, מה שמצביע על כך שאנו מעוניינים בחומר בעל מקדם Seebeck גבוה, מוליכות חשמלית גבוהה ומוליכות תרמית נמוכה. המכשול ביצירת חומר אידאלי זה הוא הקשר הקיים בין שלושת המאפיינים הפיסיקליים הללו כפונקציה של ריכוז נושאי המטען. עם עליית ריכוז נושאי המטען, ישנה עלייה במוליכות החשמלית של החומר, אך עם זאת ירידה בערכו של מקדם Seebeck. המוליכות התרמית מורכבת משתי תרומות: תרומה של השריג, המסומנת ב- κ_p , ותרומה של האלקטרונים המסומנת ב- κ_e . עם עליית ריכוז נושאי המטען, תרומת השריג נשארת קבועה בעוד שהתרומה האלקטרונית עולה, כך שבסך הכל מתקבלת עלייה במוליכות התרמית הכללית עם עליית ריכוז נה"מ. משיקולים אלו, על מנת להגיע ל- ZT גבוה יש לעבוד בתחום של מוליכים למחצה, בו מתקיים אופטימום מבחינת התכונות הפיסיקליות הרלוונטיות.

ההתקנים התרמואלקטרים הקיימים כיום בשוק ואלו היעילים ביותר מבוססים ברובם על חומרים רעילים ונדירים כגון: Pb , Bi ו- Te , ובנוסף הינם יקרים ואינם עמידים בטמפרטורות גבוהות. לפיכך, על

מנת שהחומרים התרמואלקטריים יהיו שימושיים, ישנו צורך בשימוש בחומרים זולים, ידידותיים לסביבה וששיטת הכנתם תהיה פשוטה. התחמוצות התרמואלקטריות עונות על הדרישות הללו, ובנוסף לכך יציבות בטמפרטורות גבוהות, ולכן ישנו עניין רב בחקירת חומרים תרמואלקטריים ממשפחת התחמוצות.

קיימות תחמוצות תרמואלקטריות, מסוג p , כגון $\text{Ca}_3\text{Co}_4\text{O}_9$ ו- NaCo_2O_4 , בעלות ZT המגיע ל-1, המהווה קריטריון לשימוש פרקטי בחומרים תרמואלקטריים, בעוד שערך ה- ZT הגבוה ביותר של מל"מ מסוג n נמוך משמעותית (~ 0.3 ב- 1000 K) על אף מחקרים רבים שנעשו בנושא, ולכן יש להמשיך לחקור ולשפר.

אחת ההבטחות בתחום התחמוצות התרמואלקטריות הינם משפחת ה- Perovskites , בעלי נוסחה כללית של ABO_3 כאשר A הינו יסוד מקבוצת היסודות הנדירים או מקבוצת המתכות האלקליות העפרוריות ו- B הינה מתכת מעבר. A ו- B יכולים להיבחר מתוך מגוון של אלמנטים. Perovskites מסוג תחמוצות מנגן, תחמוצות קובלט וכן תחמוצות טיטניום מאופיינים במקדם Seebeck גבוה. בפרט, תחמוצות מנגן בעלות סימונים שונים, היוצרים מל"מ מסוג n , מפגינות תכונות תרמואלקטריות מבטיחות בטמפרטורות גבוהות. התכונות התרמואלקטריות של תחמוצות המבוססות על CaMnO_3 עם סימום באתר A או B נחקרו רבות. מחקרים עדכניים של CaMnO_3 עם מגוון מסמנים מציינים ערך ZT אשר מגיע ל-0.32 ב- 1070 K באוויר עבור מל"מ מסוג n בעל סימום של Nb . עובדה זאת מצביעה על כך שתחמוצות מנגן בעלות סימום הינן בסיס טוב לשימושים תרמואלקטריים כמל"מים מסוג n . עם זאת, ערך ה- ZT אליו הן מגיעות עדיין נמוך בהשוואה לחומרים התרמואלקטריים היעילים הקיימים, בעלי ZT המגיע ל-1 ב- 300 K .

ניתן לגרום לעליה בהולכה החשמלית בעזרת סימום, בעוד שאחד האתגרים הניצבים בפני הקהילה התרמואלקטרית, הוא תכנון חומר שבו המוליכות התרמית תהיה נמוכה ללא פגיעה במוליכות החשמלית. בתחמוצות התרומה למוליכות התרמית כתוצאה מ- k_p משמעותית יותר מזו הנגרמת כתוצאה מ- k_e , מכיוון שהפונונים הינם נושאי החום העיקריים. לכן, אסטרטגיות שונות להקטנת מוליכות החום בעקבות פיזורם של הפונונים נחקרות רבות. פיזור פונונים יכול להיות מוגבר כתוצאה ממבנה גבישי מורכב, ממתבדלים ננומטרים, מעליה בכמות גבולות הגרעינים ובנוסף כתוצאה מהכנסה של אטומים זרים שמהווים מוקד פיזור נוסף. גישה נוספת להקטנת המוליכות התרמית הינה באמצעות שימוש ב- superlattice , הודות למספר הרב של משטחי הביניים הקיימים בו, הגורמים לפיזור הפונונים.

מחקר זה עוסק בעל שריגים (superlattices) טבעיים של פאזות מסוג Ruddlesden-(RP) Popper, שהינן בעלות מבנה מחזורי ברמה אטומיסטית, המתוארים פורמלית ע"י: $\text{AO}(\text{AMO}_3)_m$, כאשר: A - יסוד נדיר או מתכת אלקלית, M הינה מתכת מעבר, ו- O הינו חמצן. מבנה ה- RP הינו שכבתי,

המורכב מ- m שכבות של Perovskite, AMO_3 , המופרדות ע"י שכבת Rock-Salt, AO. בתחמוצות אלו קיים פוטנציאל למוליכות תרמית נמוכה עקב פיזור פונונים בפן-הביניים $\text{AO}/(\text{AMO}_3)_m$.

בעבודה הנוכחית אנו עוסקים בחקר התכונות התרמואלקטריות של פאזות RP מסוג $\text{CaO}(\text{CaMnO}_3)_m$, בעלות סימון של La או Nb באתרים של Ca או Mn, בהתאמה, וכן ללא סימון. החלפה של La^{+3} באתר ה-A או החלפה של Nb^{+5} באתר ה-B גורמת ליצירת Mn^{+3} בסביבת ה- Mn^{+4} , המתבטא ביצירת מל"מ מסוג n. ייצרנו מספר תרכובות של $\text{CaO}(\text{CaMnO}_3)_m$ עם ערכי m שונים וסימון של 4% אטומי של La או Nb וכן ללא סימון כלל. הסינטזה התבצעה ע"י כתישת האבקות, לחיצתן וסינטורן מספר פעמים בטווח טמפרטורות של 1173-1670 K. המיקרומבנה של הדגמים אופיין באמצעות דיפרקציית קרני-X ומיקרוסקופיית אלקטרוניים סורקת ברזולוציה גבוהה. מוליכות החום של הדגמים השונים נמדדה באמצעות טכניקת ה-LFA (Laser Flash Analysis) וכמו כן נמדדו המוליכות החשמלית ומקדם Seebeck של הדגמים, בטווח טמפרטורות של 300-1000 K.

בתוצאות שהתקבלו, הבחנו כי ישנה ירידה משמעותית במוליכות החום כתוצאה מעליית צפיפות מישורי ה- CaO , מערך של $2.9 \text{ W m}^{-1} \text{ K}^{-1}$ עבור $m=\infty$ לערך של $1.3 \text{ W m}^{-1} \text{ K}^{-1}$ עבור $m=1$ (בתרכובות המכילות סימון של Nb) ב- 1000K. בנוסף, ממודל המדמה את ההולכה התרמית, השימוש בתחום החומרים התרמואלקטרים, קיבלנו שזו אכן ההתנהגות המצופה מהחומרים הנחקרים. ממדידות ההולכה החשמלית ראינו שההשפעה של צפיפות מישורי ה- CaO על ההולכה התרמית ניכרת גם בההולכה החשמלית, כך שישנה ירידה בהולכה החשמלית עם עליית צפיפות מישורי ה- CaO מערך של $\Omega^{-1} \text{ cm}^{-1}$ ל- $76 \Omega^{-1} \text{ cm}^{-1}$ עבור $m=\infty$ ל- $2.9 \Omega^{-1} \text{ cm}^{-1}$ עבור $m=1$ (בתרכובות המכילות סימון של Nb) ב- 1000K. הירידה בהולכה החשמלית משמעותית יותר מהירידה בהולכה התרמית וכתוצאה מכך התקבל כי ערכי ה-ZT הכוללים בתרכובות ה-RP נמוכים מאלו שהתקבלו עבור פאזות ה- CaMnO_3 שאינה מכילה את מישורי ה- CaO .

על אף שערכי ה-ZT שהתקבלו הינם נמוכים יותר עבור תרכובות ה-RP, ישנם גורמים נוספים שכדאי לחקור אשר עשויים להשפיע כגון: ייצור בשיטות שונות, וכן סימון בריכוזים שונים או בעזרת מסממים שונים מאלו שנחקרו על-ידנו.